Controlled Escape from Trapped Contact Modes in Magnetic Bearing Systems

Saket, Fawaz

Award date:
2016

Awarding institution:
University of Bath

Controlled Escape from Trapped Contact Modes in Magnetic Bearing Systems

Fawaz Yahya Saket

A thesis submitted for the degree of Doctor of Philosophy

University of Bath
Department of Mechanical Engineering

February 2016

ABSTRACT

Rotors supported by active magnetic bearings under contact-free levitation have many advantages, such as allowing near frictionless rotation and high rotational speeds. They also provide the designer the capability to achieve increased machine power density. However, magnetic bearings possess limited load capacity and operate under active control. Under certain operational conditions, the load capacity may be exceeded or a transient fault may occur. Touchdown bearings or bushes are required in such systems, from the operational and design points of view, to prevent contact between the rotor and stator laminations causing damage to the system.

Rotor/touchdown bearing contact can occur in fault conditions and under external disturbances, even if the magnetic bearings are fully functional. If the rotor makes contact with the touchdown bearings, the ensuing rotor dynamics may result in transient or sustained contact dynamics. These dynamics involve transmitting a range of stresses under distortional strains. Such stresses occur under different contact modes, can be of very short or long duration, and can affect the life span of touchdown bearings. Touchdown bearings thus characterise significant safety and reliability aspects of active magnetic bearing systems. Maximisation of the performance and operational life of magnetic bearing systems dictates the need for minimisation of rotor/touchdown bearing contact. Magnetic bearing forces may have the capability to restore contact-free rotor levitation, though this will require appropriate control strategies to be devised. An understanding of the contact dynamics is required, together with the relationship between these and magnetic bearing control forces.

In this thesis, rotor/touchdown bearing contact conditions are identified and investigated dynamically. An active magnetic bearing system with a long flexible rotor is considered. A nonlinear system model is employed, and a speed range covering three of the rotor's critical frequencies is taken into account. Different types of transient and steady-state contact modes are identified, including non-persistent and persistent trapped contact modes of varying contact force levels and time durations. Design methodology is presented for a force measurement system capable of providing rotor/touchdown bearing contact force related data, based on experimental

strain measurement. The system is implemented and a calibration method of assessing magnetic bearing forces based on rotor/touchdown bearing contact is demonstrated. The frequency dependent behaviour of the active magnetic bearing system is considered using evaluated force and phase measurements. Force measurements covering one of the rotor's critical speeds are experimentally validated using an open-loop control strategy, aimed at attenuating rotor vibration in contact cases. Rotor recovery from a persistent rub contact mode through employing synchronous active magnetic bearing forces is demonstrated and discussed. The range of magnetic bearing control forces capable of contact elimination is also explored for different running speeds. The new control method presented provides insight into potential control methods capable of achieving rotor/touchdown bearing contact recovery utilizing experimental force data in contact conditions. This will contribute towards improving safety and reliability aspects of active magnetic bearing systems, which undergo operational conditions leading to rotor/touchdown bearing contact.

ACKNOWLEDGEMENTS

This thesis is the result of the research work I undertook at the Centre for Power Transmission and Motion Control, at the Department of Mechanical Engineering, at the University of Bath. I am sincerely grateful to everyone who supported me during the research work.

I would like to particularly thank my supervisor, Professor Patrick Keogh, for his patient guidance, continuous support and encouragement, and valuable advice throughout the research. I am also grateful to my co-supervisor, Professor Necip Sahinkaya, for his support, guidance, and valuable input during his time at the University of Bath.

I gratefully acknowledge the receipt of a studentship from the Engineering and Physical Sciences Research Council.

Last, but not least, I dedicate this thesis to my parents.

CONTENTS

1. Introduction **1**

1.1 Overview 1

1.2 Rotor/Active Magnetic Bearing Systems 1

1.2.1 Background 1

1.2.2 Advantages 3

1.2.3 Applications 4

1.3 Touchdown Bearings 4

1.4 Rotor/Active Magnetic Bearing System Dynamics 6

1.4.1 Fault Conditions 6

1.4.2 Rotor/Touchdown Bearing Contact Dynamics 7

1.5 Control of Rotor/Active Magnetic Bearing Systems 11

1.5.1 Active Magnetic Bearing Control 11

1.5.2 Control of Rotor/Touchdown Bearing Interaction 12

1.6 Gaps in the Knowledge 16

1.7 Research Hypothesis 17

1.8 Project Aim and Objectives 17

2. Experimental Rotor/Active Magnetic Bearing System Rig **19**

2.1 Overview 19

2.2 Experimental Facility Description 19

2.3 System Rig Components 23

2.3.1 Active Magnetic Bearings 23

2.3.2 Power Electronics 31

2.3.3 Displacement Sensors 32

2.3.4 AC Motor and Rotor Encoder 35

2.3.5 Force Measurement System 36

2.4 Rotor Sag 37

2.5 Data Acquisition and Control 39

2.6 Closed Loop Control System 40

2.7 Closure 41

3. Rotor/Active Magnetic Bearing System Model 42

3.1 Overview 42

3.2 Finite Element System Model 42

3.3 Active Magnetic Bearings Model 45

3.3.1 Nonlinear Modelling 45

3.3.2 Control Parameters 46

3.4 Touchdown Bearing Model 47

3.5 Sensors/Bearings Non-collocation 50

3.6 System Response Representation 51

3.7 Closure 52

4. Rotor/Touchdown Bearing Contact Modes 53

4.1 Overview 53

4.2 Contact at Various Rotating Frequencies 53

4.3 Contact with Variable Rotor Unbalance 62

4.4 Closure 70

5. Rotor/Touchdown Bearing Contact Force Measurement System 71

5.1 Overview 71

5.2 Design Considerations 71

5.3 System Description 74

5.4 Force Measurement Calibration 81

5.4.1 Calibration Methodology 81

5.4.2 Static Tests 83

5.5 Closure 89

6. Contact Dynamic Tests and Analysis 90

6.1 Overview 90

6.2 Dynamic Force Assessment 90

6.3 Phase Assessment 100

6.4 Contact Behaviour at Varying Forces and Frequencies 106

6.5 Experimental and Simulation Model Results Comparison 111

6.5.1 Contact Force and Phase Simulation Results 111

6.5.2 Measured and Calculated Force Relationships 114

6.5.3 Measured and Calculated Rotor Displacement 118

6.6 Closure 123

7. Control Strategy for Contact Recovery Based on Force Measurement **124**

7.1 Overview 124

7.2 Control System Description 124

7.3 Experimental Procedure 126

7.3.1 Rotating Rotor/TDB Contact 126

7.3.2 Static Calibration and Dynamic Tests 128

7.3.3 Control Force Assessment 133

7.4 Unbalance Control Tests 136

7.5 Closure 147

8. Conclusions and Future Work **148**

8.1 Conclusions 148

8.2 Future Work 152

References **153**

NOMENCLATURE

A	Force amplitude
A_B	Beam cross section area
A_p	Pole face area
B	Flux density in magnetic bearing coil
c_b	Touchdown bearing support damping
c_R	Rotor/bearing radial clearance
e	Mass eccentricity
E	Young's modulus
F	Attractive force generated by one coil
F_c	Rotor/bearing contact force
F_{cn}	Normal contact force between rotor and bearing
F_{ct}	Tangential contact force between rotor and bearing
F_i	Input force for rotor contact control
F_{MB}	Magnetic bearing force
F_u	Unbalance force
F_z	Force of a double pole magnet
H_{gap}	The magnetic field strength in the air gap
I	Current
I_b	Bias current
I_c	Control current
I_M	Second moment of area

I_s	Static current to balance rotor weight
k	Characteristic constant
k_b	Touchdown bearing support stiffness
k_{BA}	Beam axial stiffness
k_{BB}	Beam bending stiffness
K_D	Controller derivative gain
K_i	Current gain of the magnetic bearing
K_I	Controller integral gain
K_P	Controller proportional gain
K_s	Negative stiffness of the magnetic bearing
l	Length
L	Beam length
l_c	Circumferential contact patch length
l_{gap}	Air gap length
l_{iron}	Flux path length
m	Mass
m_b	Touchdown bearing mass
N	Number of turns per coil
r	Radius
R	Rotor displacement amplitude
t	Time
T	Periodic time
V	Relative velocity between the rotor and touchdown bearing
x, y	Rotating frame coordinates

X, Y	Rotor displacements
X_b, Y_b	Touchdown bearing displacements
z	Rotor displacement in a single axis
C	Calibration matrix
D	Damping matrix
f	Forces vector
F	Forces matrix
K	Stiffness matrix
M	Mass matrix
q	Displacements vector
r	Rotor displacement amplitudes vector
v	Strain gauge voltages vector
V	Strain gauge voltages matrix
α	Amplitude ratio between applied and estimated active magnetic bearing forces
α_c	Amplitude ratio between applied force and calculated contact force
β	Amplitude ratio between calculated contact force and estimated active magnetic bearing force
μ	Coulomb coefficient of friction
μ_0	Permeability of free space
μ_r	Relative permeability of iron
Ω	Rotor rotational frequency
ω	Rotor whirl frequency
θ	Phase angle

ϕ	Phase shift angle
ν	Poisson's ratio

Subscripts

c	Contact
i, **i**	Input control
MB, **MB**	Magnetic bearing
R	Resultant of *X* and *Y* components
R	Rotational
T	Translational
u	Unbalance
X	Horizontal component
Y	Vertical component

Superscripts

e, **e**	Estimated
T	Transpose
^	Input or measured

Chapter 1

INTRODUCTION

1.1 Overview

A literature review of rotor/magnetic bearing systems is presented in this chapter. The behaviour of rotor/touchdown bearing contact cases is discussed, in particular, with previous work on rotor/bearing dynamic interaction investigations. Different possible control techniques for vibration attenuation and contact-free recovery of rotor/bearing contact are discussed, specifically those that can be employed during full operation of active magnetic bearing systems. The importance of devising control strategies based on magnetic bearing control forces employing rotor/bearing interaction data is highlighted.

1.2 Rotor/Active Magnetic Bearing Systems

1.2.1 Background

Rotating machinery is used in a variety of mechanical systems, where bearings are an essential element that provide shaft support. Magnetic bearings, in contrast to conventional bearings, support shafts with magnetic forces, rather than mechanical or fluid contact. They have been used in industrial applications for many years, in systems such as compressors, turbomolecular pumps, flywheels and beam choppers.

Magnetic bearing systems can be active or passive. While passive magnetic bearings incorporate permanent magnets, Active Magnetic Bearings (AMBs) rely on electromagnets, with power amplifiers providing control currents. Passive magnetic bearings are limited by their fixed properties dictated by their design. The primary advantage of active magnetic bearings is the ability to vary system parameters, such as stiffness and damping, and the ability to actively control the system to achieve desired goals. Thus, active magnetic bearings are more commonly used than passive bearings.

Rotor/AMB systems rely on electromagnetic forces to levitate, suspend, and control a rotor. This is achieved by applying suitable electric currents through the bearings' ferromagnetic materials. Rotor/AMB systems also incorporate power amplifiers, rotor position sensors, and controllers. Control currents provide appropriate forces on the rotor through the magnetic bearings, causing the rotor to be levitated within a specified air gap or clearance. A feedback control loop including position sensor measurements is usually used to monitor and control rotor motion. AMB systems can include radial bearings, axial bearings, or a combination of both, depending on the application.

Rotor/AMB systems also include auxiliary or Touchdown Bearings (TDBs). They act as a safety element to prevent physical interaction between the elements of the magnetic bearings and the rotor, in cases where faults or failures occur. Touchdown bearings also support the rotor in its de-levitated position when the system is powered off. The rotor/TDB clearance is smaller than the rotor/AMB clearance to prevent potential damage in all cases.

The structure and features of active magnetic bearings make them suitable for novel research studies investigating rotor/bearing interaction and behaviour.

1.2.2 Advantages

AMBs distinctively provide non-contact suspension for high-speed rotors, the main reason why AMB systems are increasingly receiving attention. This is because the contactless operation of magnetic bearings introduces a number of advantages over conventional bearings, such as journal or ball bearings, and thus overcomes many of their deficiencies. The key advantages of AMB systems include:

- Operation with high rotational speeds is possible
- Elimination of the need for lubrication due to the contactless operation
- Long life and high reliability, which are a result of the absence of rotor/AMB physical interaction, minimising wear related issues
- Operating over a wide range of temperatures is possible (Yang *et al.*, 1991; Youcef-Toumi and Reddy, 1993)
- The ability to work in vacuum with no contamination (Schweitzer, 2002)
- Vibration control/attenuation of rotor motion, which is due to the capability to apply active control forces to the rotor
- Built-in measurement and control systems to facilitate fault diagnosis and performance monitoring, and therefore lower system maintenance
- Energy efficiency and low running costs due to low friction losses, which are higher in conventional bearings.

Although there are many advantages of AMB systems, the primary disadvantage they have, which may limit their application in some cases, is that they require power to operate. The power is required to drive the electromagnets, in addition to the control system which also incorporates measurement sensors. This could be a concern in applications where the system design and operational simplicity, and/or installation cost are of importance. Moreover, AMBs can have lower load capacities in comparison to conventional bearings, which remains one of the limiting factors of AMB application in some cases.

1.2.3 Applications

Rotating machinery is used in a variety of mechanical systems, such as machine tools, industrial turbomachinery, and aircraft gas turbine engines. The exploitation of active magnetic bearings for rotating machinery has spanned a wide range of applications and has become a unique area of research for potential applications.

Various applications of AMB systems in industry, in addition to scientific applications, have been presented and discussed by researchers including Dussaux (1990), Schweitzer *et al.* (1994), and Kasarda (2000). Industrial applications include machine tool applications such as electro-spindles, widely used for milling and grinding purposes. Light industrial applications include X-ray tubes and turbomolecular pumps, while heavy industrial applications include compressors and generators. Recently, Siemens has developed an AMB levitated steam turbine (Siemens, 2015). In aerospace the main applications are momentum/energy storage flywheels used in systems like satellites, and turbopumps used in jet and rocket engines.

Additionally, medical applications include neurosurgery catheter systems (Schoeb and Dasse, 2001) and artificial heart pumps (Lee *et al.*, 2003). Potential applications include micro-techniques in video heads, hard disk drives, and optical scanners (Schweitzer, 2002).

1.3 Touchdown Bearings

While active magnetic bearing systems allow high speed rotor operation under controllable levitation, from the operational and design points of view, touchdown bearings are required to limit rotor excursions, mainly to prevent rotor/magnetic bearing stator contact. Touchdown bearings are special conventional bearings such as rolling element bearings or bushes.

Touchdown bearings support the rotor while the system is not operating, but also catch the rotor during operation in certain cases of rotor/touchdown bearing contact. These include cases with power loss, failure in the equipment, exceeding the load capacity of AMBs, the occurrence of rotor mass loss, or cases where motion induced external disturbances occur. The task of touchdown bearings is essential in these cases to prevent system damage.

When rotor/TDB interaction occurs, it involves transmitting a range of stresses under distortional strains, and dissipating frictional heat. These stresses occur under different contact modes, can be of very short or long duration, and can involve large rotor/TDB contact forces. Thus, touchdown bearings have a limited life, and are only able to sustain a limited number of rotor drops or contact cases.

Safety and reliability aspects of AMBs can be highlighted by their fault tolerance characteristics, which include the ability of running the rotor down safely in some conditions, and the ability to recover normal operation in other cases, where transient rotor motion leading to rotor/TDB contact occurs. Such cases are possible even if the magnetic bearing system is fully functional, because of fault conditions, or any other abnormal operating conditions (Keogh and Cole, 2003).

Since touchdown bearings are safety components of AMB systems, it is crucial to understand their dynamic behaviour in order to minimise damage due to rotor/TDB interaction. This is particularly important as touchdown bearing life and performance is an issue that needs careful consideration in the application of magnetic bearing systems.

1.4 Rotor/Active Magnetic Bearing System Dynamics

1.4.1 Fault Conditions

Different fault conditions exist that can cause rotor/touchdown bearing interaction. A number of possible fault conditions in AMB systems were discussed by Cole *et al.* (2004). These include internal faults to the system such as power failure, transducer faults or failure, bearing magnet failure, and computer/controller hardware or software failures. Fault conditions also include external influences to the AMB system such as:

- Rotor mass loss
- Base motion
- Rotor impact
- Sudden loading changes
- Rotor deformation

These faults are external disturbances affecting the system, and they can be replicated by external disturbances applied to the system. External disturbances consist of transient motion and can also consist of steady-state motion. Such disturbances can occur in certain operating environments or potential AMB applications such as land, sea and air transport systems.

Internal system faults may lead to control loss or stability loss, and require component maintenance in most cases. However, external faults may lead to abnormal rotor vibration, which may result in rotor/TDB contact. To overcome this problem, appropriate controller design is required to apply sufficient control forces to restore the rotor to normal operation.

1.4.2 Rotor/Touchdown Bearing Contact Dynamics

Literature on rotor contact dynamics has spanned a wide range of investigations, including rotor contact with the touchdown bearings or the housing. The early work of Black (1968) investigated the rotor whirl motion. For different frequencies, a coupled motion between rotor and stator was illustrated. Experiments undertaken by Lingener (1990) demonstrate that in the vibrations of the rotor and stator system, the whirl frequency stays constant although the shaft speed is increasing. The backward whirl motion was specifically examined by Bartha (1998), including the influence of touchdown bearing parameters.

Different rotor/bearing contact modes are reported in the literature as a result of varying impact dynamics, including rotor unbalance and disturbances acting on the system. Full annular rub was studied and modelled by Muszynska (2002). Rub modes were also investigated by Black (1968) and Bartha (1998). Wu and Flowers (1993) studied and illustrated bouncing rotor motion. Kim and Noah (1990), and Wang and Noah (1998) studied chaotic rotor motion.

In addition to Black (1968), Ehrich (1965) identified bistable rotor motions in the vibrations of a rotor surrounded by an annular clearance. Muszynska (1989) reported a mathematical model demonstrating the synchronous and non-synchronous motions of the rotor, with experimental results. Muszynska (1984) also demonstrated subsynchronous rotor vibration.

Rotor drop tests were used in several studies to investigate rotor/touchdown bearing dynamics (Schmied and Pradetto, 1992; Kirk and Ishii, 1993; Swanson *et al.*, 1995; Hawkins *et al.*, 2007). Kirk *et al.* (1997) provide a complete study on modelling AMB rotor drop. Modelling techniques were studied to provide data on the dynamics of the rotor/touchdown bearing force levels.

Although rigid rotor dynamics is more widely investigated, investigations on flexible rotor systems are considered in some studies (Foiles and Allaire, 1997; Kirk, 1999; Cole and Keogh, 2003b).

Keogh and Cole (2003) demonstrated contact modes that can occur during rotor/bearing interaction due to unbalance, in addition to the synchronous response without contact. Analytical methods with idealized contacts were used, and the dependence of rotor motion through different contact modes on the initial conditions of the first contact was illustrated. Changes in the synchronous components of the rotor's response when entering a contact mode were observed, and the necessity to account for those changes in the control strategy was underlined and demonstrated experimentally.

Methods reported in the literature to study and analyse rotor contact include employing finite element based methods (Kirk *et al.*, 2005), the harmonic balance method (Von Groll and Ewins, 2001) and computer simulations involving shaft pitching at the contact (ZapomeÏ *et al.*, 2001). Rotor/touchdown bearing contact forces are usually modelled as a function of the rotor penetration depth into the inner bearing race at the contact location (Bedoor, 2000).

Dell *et al.* (1988) conducted different tests highlighting the performance of touchdown bearings. In particular, the work of Schmied and Pradetto (1992) involved theoretical and experimental investigations into the vibrations of a rotor with touchdown bearings, where the effects of damping, the friction coefficient and the moment of inertia of the inner race on the whirling motion of the rotor were demonstrated.

Fumagalli *et al.* (1994) studied rotor contact dynamics where measured rotor vibration and contact forces were demonstrated for friction-induced whirl motion. Similar studies were conducted by Feeny (1994). Large rotating speeds relative to whirling speeds were used causing the rotor to be in a sliding motion.

The work of Fumagalli and Schweitzer (1996) included the results of large-amplitude backward whirl as a result of high rotating speeds. The use of a soft mounted touchdown bush was reported to produce less whirl speeds, but with larger vibration amplitudes in some cases. A nonlinear stiffness and damping model of contact dynamics was used. Comparison between calculated and measured contact forces was presented. A similar model was used by Wang and Noah (1998) to study rigid rotor/bearing dynamics.

Contact force prediction was studied by researchers investigating the transient response (Kirk *et al.*, 1994; Kirk *et al.*, 1996; Ramesh and Kirk, 1994). Rotor drop tests have also been undertaken. Kirk *et al.* (1994) built an experimental facility with a heavy rotor, where large contact forces of friction-induced backward whirl on the touchdown bearing were demonstrated. Ishii and Kirk (1991, 1996) reported an optimum touchdown bearing support damping value that can reduce both rotor whirl motion and contact forces, by employing transient response techniques to their nonlinear model. The work of Kirk (1999) included the study of rotor/bearing interaction of turbomachinery touchdown bearings, where the experimental setup was designed to improve the understanding of rotor drop cases. Different touchdown bearing configurations were evaluated in the study.

Zeng (2003) investigated the transient motion of rotor drop on touchdown bearings in different cases. It was found that for a touchdown bearing with a constrained inner race and no lubrication, the coefficient of friction is not constant and may change with abrasion, while having a free inner race is advantageous as this allows the inner race to accelerate. It was further noted that using a soft support can reduce the abrasion and make the coefficient of friction increase less rapidly than when using a hard-mounted support, which can lead to full-clearance backward whirling motion after rotor drop. In addition, having a lubricated rotor/bearing contact surface was found to be useful, as a low coefficient of friction is obtained.

The performance of touchdown bearings and bushings, mounted in different configurations with and without lubrication, and the influence of rotor unbalance on the whirling motion of the rotor was demonstrated by Swanson *et al.* (1995). Full-clearance forward whirl was illustrated experimentally, as opposed to full-clearance backward whirl. Full-clearance whirling motion is particularly harmful to the system. It was found that if bushings are softly mounted, rotor whirl is generally more effectively concealed, although the vibration caused by the transient response following contact can be more significant than in other arrangements. This is in agreement with the results produced by Fumagalli and Schweitzer (1996) and Kirk and Ishii (1993).

Touchdown bearings can normally endure a number of rotor drops or rundowns in cases where the AMB system is not operating (Schmied and Pradetto, 1992; Hawkins *et al.*, 2007). This is because the rotor is de-levitated and contact with touchdown bearings occurs. While there is a range of literature on rotor/bearing contact and rotor drop tests, contact dynamics taking place while the magnetic bearings in AMB systems are functional, with their control capability not directly affected, is still an area of potential research.

Some studies have investigated system dynamics with fully operational AMBs including Abulrub *et al.* (2006a) and Sahinkaya *et al.* (2007). Abulrub *et al.* (2006a) developed a method, using constrained Lagrangian equations of motion, to model rotor/bearing contact dynamics without direct modelling of the contact forces. The method can be applied to multi contact cases. Experimental results were presented to validate their simulation results. Sahinkaya *et al.* (2007) undertook further investigations using the same modelling technique. Contact cases were initiated by applying unbalance forces through magnetic bearings. It was found that in the case of a low friction coefficient between the rotor and the inner surface of the touchdown bearing, the rotor can enter into forward whirl motion, and in such cases, the rotor position can be recovered from contact provided any additional unbalance forces are removed. However, in cases where the friction coefficient is very high, backward whirl can occur, and it was shown that once in this mode, rotor recovery is not possible even if the forces that cause the contact are removed.

If the operating environment of the AMB system introduces input disturbances or rotor unbalance that can initiate or sustain rotor/touchdown bearing contact, and shutting down the system is not an option, if continuous operation is required. The ability to recover the rotor position in such cases would be advantageous and can extend the application of AMB systems to applications where such disturbances occur.

Different rotor/bearing contact modes reported in the literature are possible, which include whirl rub, bounce and chaotic modes, and can involve large rotor/bearing contact forces. Control of the system to restore normal operation successfully is an area that is open to investigation. This could be achieved using AMB forces, or by using additional actuators in the system when feasible. The occurrence of such modes

depends on the impact dynamics and unbalance caused by any disturbances to the system. Control of the system becomes a significant issue when the rotor remains in continual contact in these modes.

1.5 Control of Rotor/Active Magnetic Bearing Systems

1.5.1 Active Magnetic Bearing Control

AMBs allow controllable damping and stiffness according to system requirements. AMBs were used as actuators in early investigations for the control of rotor dynamics (Schweitzer, 1976). Several studies subsequently presented rotor control techniques using AMBs. An early study presented open-loop adaptive control strategies for multi-mode rotor/bearing systems (Burrows and Sahinkaya, 1983), where minimisation of the vibration of a rotor/bearing system was demonstrated. The method used provided sensitivity of the optimum response to changes in system control forces.

Closed loop control of AMBs has been investigated and shown to enable active vibration suppression and on-line bearing stiffness control (Dussaux, 1990; Sinha *et al.*, 1991). In particular, synchronous vibration control has been studied using closed loop feedback methods, where changes in unbalance and transient vibration can be minimised (Knospe *et al.*,1995; Sivrioglu and Nonami, 1995).

Robust control methods for AMBs were studied by researchers to allow for uncertainties in system parameters and for a variety of disturbances that can act as additional inputs to the system (Schweitzer, 2005). Such methods were presented by Zhou and Doyle (1997) for the design of robust H∞ control. This method was investigated in a number of studies (Nakashima *et al.*, 1996; Cole *et al.*, 2004), where H_∞ optimisation minimises the effect of modelling errors and offers improved tolerance to external faults, providing robustness.

On the other hand, robust μ–synthesis control for AMB applications was identified (Schoenhoff *et al.*, 2000), where a flexible AMB system model with rigorous gyroscopic effects and substructure modes was used. Gyroscopic effects were considered as uncertainty, in addition to modelling errors considered in uncertainties in the natural frequencies. Experimental evaluation of the performance was undertaken. Measured performance and the predicted robust performance showed good agreement.

1.5.2 Control of Rotor/Touchdown Bearing Interaction

There are publications aimed at developing and testing control strategies that can effectively control rotor/touchdown bearing contact conditions while AMB systems are fully functional. However, this is an area that needs to be investigated further. In such cases, the re-levitation of the rotor from a contact mode is studied, and the aim is to restore normal contact-free operation of the system. On the other hand, while complete recovery or prevention of contact may not be possible, specially when the dynamics involve large amplitudes and contact forces exceeding the capability of the control forces of AMB systems, suitable control action can act to reduce the orbits of the rotor to reduce the effects of contact.

A controller acting during rotor/bearing interaction has to account for the dynamic changes during this event, and it also has to work towards minimising both the magnitude and duration of contact forces, in order to keep system stability and prevent significant damage (Cole and Keogh, 2003a).

Various types of control strategies have been developed to reduce rotor vibrations. On the other hand, few studies have tested controllers designed specifically to take into consideration rotor/bearing contact. The reduction or removal of rotor/touchdown bearing contact has been studied using magnetic control forces in some investigations including those by Keogh and Cole (2003), Cole and Keogh (2003a), and Abulrub *et al.* (2006b). Other investigations employed the induced motion of touchdown bearings in contact control, such as Ulbrich *et al.* (2004) and Cade *et al.* (2008).

Cole and Keogh (2003a) investigated robust controller synthesis for rotor vibration attenuation with models involving a range of rotor contact conditions. A linear time-varying system model was used for the synthesis of controller gain matrices. Maintaining dynamic stability and steady state vibration levels were the objectives for designing novel control methods that included H_∞ optimisation. Experimental tests verified the action of the robust controllers where near-optimal rotor vibration levels were recovered from contact conditions.

In a study by Keogh *et al.* (2004), it was established that in synchronously forced vibration, synchronous vibration components can provide a useful measure of rotor vibration as well as providing a way of deriving synchronous control forces in harmonic controllers. It was also shown that the rotor can be driven to make persistent contacts, and the changes in measured vibration components were demonstrated. It was underlined that controllers based on linear non-contact dynamics can be ineffective and can worsen the rotor dynamics in contact cases. The controller derived and demonstrated in the study was based on parameters obtained from measured amplitude and phase changes of vibration components, to enable returning the rotor from a contacting to a non-contacting condition.

Abulrub *et al.* (2006b) investigated a control strategy to prevent rotor bearing contact cases. A recursive open-loop adaptive control algorithm was presented, that is based on the classic open-loop adaptive control method (Burrows and Sahinkaya, 1983). The algorithm updates both control force amplitude and phase, for rapid response to changes in external forces, such as those causing rotor unbalance. Simulation and experimental results were presented. It was demonstrated that the control strategy is fast enough to prevent the occurrence of contact in many cases, that being dependent on excitation levels. Also, it was shown that if contact occurs, the impact can be minimised, and rotor recovery is possible.

The above-mentioned investigations demonstrate the ability to restore rotor control from some contact cases involving persistent contact modes, provided appropriately-phased synchronous control forces are applied. This is particularly important, as the need to shut down the AMB system can be eliminated.

Touchdown bearing design and actuation has been investigated by researchers to deal with the problem of touchdown bearing life and reliability. This is because contact conditions can lead to touchdown bearing damage over time, due to the stresses and strains involved. Also, touchdown bearing actuation is considered if the load capacity of the magnetic bearings is temporarily exceeded.

Keogh (2012) discussed contact cases in rotating machinery, where rotor/TDB contact was studied, and the benefits for making the touchdown bearing an active element of the system were highlighted. The options for using active TDBs to help in rotor/TDB contact cases were mentioned. Cade *et al.* (2009) considered an active touchdown bearing to limit trapped contact modes, where rotor recovery was demonstrated with the variation of the touchdown bearing controller parameters. Control strategies were explored using the harmonic decomposition of rotor/bearing contact. Li *et al.* (2012) demonstrated that the recovery of rotor/TDB contact cases is possible with active TDB systems, where small motions under large transient actuation are required. TDB actuation was applied through piezoelectric stack actuators. The use of piezoelectric actuators for active vibration control of rotor/bearing systems was also examined by Palazzolo *et al.* (1991).

Ulbrich *et al.* (2004) developed a touchdown bearing system with electromagnetic actuators, to minimise rotor/bearing contact forces. The control system designed was aimed at reducing impact forces and stabilizing the rotor in the case of persistent contact. This was done by having the touchdown bearing track the rotor trajectory before the occurrence of impact and by making it avoid multi impacts. Further investigations on the application of electromagnetically actuated touchdown bearings were carried out by Ginzinger and Ulbrich (2006). A PID controller was used in controlling the actuators. Althaus and Ulbrich (1992) employed a hydraulic actuator to transmit control forces through a conventional bearing. In another design, Santos (1993) also investigated hydraulic actuation. Ulbrich (1994) presented a complete study comparing the above-mentioned different actuator concepts, and the effectiveness of using each actuator for different objectives was examined.

However, the main drawbacks of active touchdown bearing systems are the increased cost, in addition to the added complexity of the design and control of the AMB system,

although they offer some control advantages provided adequately capable actuation is available.

Since AMB systems can be appropriately employed for controlling rotor vibration during rotor/bearing contact, and restoring contact-free operation in some cases using AMB control forces, new control approaches using AMBs may be possible.

Knowledge of the interaction dynamics between the rotor and the touchdown bearing is necessary for optimising control action, and reducing or eliminating the damaging effect of contact modes. While displacement measurements have been typically used in experimental investigations presented in the literature to study rotor/bearing interaction and devise possible control strategies, only a few studies have considered the measurement and analysis of forces relating to contact conditions (Fumagalli *et al.*, 1994; Bartha, 1998; Cuesta *et al.*, 2002).

Fumagalli (1997) performed measurements to improve the understanding of the nonlinear contact dynamics, including force data, on a rigid system. Bartha (2000) examined specifically the potentially damaging condition of dry friction backward whirl. Cuesta *et al.* (2002) examined the response of a rigid rotor, supported by a magnetic bearing on one side, and considered emergency stop cases at several running speeds. The rotor motion was considered with the magnetic bearing deactivated.

While displacement sensors are commonly used in rotor/bearing systems, other types of sensors have also been used in some studies, aiming to assess contact forces in rotor systems. This includes using acceleration signals (Fumagalli, 1997), and strain measurements from gauges mounted on the outer bearing ring (Kwapisz *et al*., 2008). Sensor data were related to force levels experienced by the bearing in contact conditions. Experimental force measurements could provide additional important data leading to better understanding of contact dynamics, and thus providing new possibilities for control strategies in AMB system applications.

1.6 Gaps in the Knowledge

The literature reviewed demonstrates the ability to successfully control rotor/TDB contact in some contact conditions involving persistent contact modes, provided appropriately-phased synchronous AMB control forces are applied. It is evident that better understanding of rotor/TDB contact dynamics in AMB systems is important for optimising methods capable of minimising or eliminating contact conditions. This is particularly significant if the need to shut down the AMB system can be eliminated, and control of contact conditions can be optimised while AMBs are fully functional, as it will contribute to expanding the applications of AMB systems.

Some of the studies discussed in this chapter considered experimental measurement of rotor/bearing contact force related data, to enable better assessment and understanding of rotor/bearing contact conditions, in comparison to using rotor displacement data. Other studies considered developing rotor/TDB contact control in AMB systems based on rotor displacement data, by employing AMB control forces. However, devising rotor/TDB contact control strategies in operational AMB systems based on measured data directly related to rotor/TDB contact forces is still an area of potential research.

In order to devise force based contact control in rotor/AMB/TDB systems, a method of experimentally assessing data related to rotor/TDB contact forces is required, together with establishing a relationship between this data and AMB control forces. This could form the basis for new control methods enabling finite duration contact control in fully operational AMB systems that experience intermittent faults or external inputs or disturbances.

The research undertaken for this thesis extends experimental measurement of rotor/TDB contact force related data to an AMB system with a long flexible rotor, as opposed to a rigid rotor, for the purpose of rotor/TDB contact control. Assessment and control of forces related to rotor/TDB contact conditions in operational AMB systems is identified to provide a number of advantages over rotor displacement based assessment and control of contact, including:

- Force related data would provide a clear indication of rotor/TDB contact occurrence. On the other hand, rotor orbits obtained from displacement data do not necessarily confirm whether contact has occurred. They also may not give a clear indication of the type of contact if contact has occurred

- Experimental assessment of contact force related data can be directly employed in synchronous control strategies using AMB control forces, while further analysis is needed if displacement data is employed

- Changes in rotor/TDB contact forces, stresses or strains affecting the system cannot be determined using displacement data, except by possible less or more audible contact becoming evident. Experimental assessment of contact force data can provide such information

- Evaluation of force levels due to contact can provide improved system monitoring and diagnosis, particularly in relation to touchdown bearings.

1.7 Research Hypothesis

The purpose of this research is to establish that forces related to rotor/TDB contact conditions in AMB systems can be experimentally assessed and then minimised or eliminated through new force based control methods, which employ AMB control forces, while AMBs are fully operational.

1.8 Project Aim and Objectives

The aim is to enable contact-free recovery from contact modes in rotor/AMB/TDB systems. The objectives of the research in this thesis were to:

- Investigate the dynamic behaviour of rotor/bearing contact cases in magnetic bearing systems, which undergo fault conditions or external motion induced disturbances, where the disturbances can be replicated by the application of inputs such as unbalance forces on the system. Theoretical investigations would include a nonlinear dynamic system model

- Design and build a force measurement system capable of providing rotor/bearing contact force related data, to experimentally identify the dynamic behaviour of rotor/bearing interaction cases

- Calibrate the force measurement system statically and dynamically in relation to applied forces of an active magnetic bearing, which are capable of providing rotor motion control. A rotor/magnetic bearing system with a long flexible rotor would be used. Dynamic calibration would include testing a range of whirl frequencies covering different rotor modes, and deriving force and phase data

- Compare theoretical and experimental tests at different rotor frequencies to help in the understanding and validation of contact force models

- Devise and experimentally test a control strategy to evaluate the force measurement methodology. Force measurement data would be used and the control would employ synchronous active magnetic bearing forces to minimise or eliminate rotor/touchdown bearing contact cases. The control would be tested on a frequency range covering one of the rotor's critical frequencies.

Chapter 2

EXPERIMENTAL ROTOR/ACTIVE MAGNETIC BEARING SYSTEM RIG

2.1 Overview

In order to demonstrate the contact behaviour of rotor/touchdown bearing interaction, a rotor/AMB experimental facility is used. This chapter describes the test rig and its components. The rig design and validation are also discussed, particularly the magnetic bearing characteristics. The signal measurements and control system used in the rig are also described.

2.2 Experimental Facility Description

A rotor/active magnetic bearing test rig with a flexible rotor is employed in this project. The system has two electromagnetic bearings connected to power amplifiers to generate coil currents, hence control forces, a rotor with four discs, position transducers providing displacement signals, and an AC motor at one end. A photograph of the experimental facility is shown in Figure 2.1.

Figure 2.1: The rotor/active magnetic bearing experimental facility

The rotor is a uniform flexible steel shaft of 2 m length having a radius of 25 mm. The motor can run at up to 100 Hz. That speed range covers four rotor resonant frequencies, including conical and cylindrical modes, in addition to flexural bending modes. The discs have 120 mm radii, and have a mass of 10 kg each. They are used to increase the inertia of the rotating system. The disks are designed and positioned so that the second flexural frequency of the rotor is significantly lower than the maximum running speed.

Two sets of radial electromagnets are used to the produce control forces. Each electromagnet has eight poles. There is a radial clearance of 1.2 mm between the stator and rotor in each of the magnetic bearings, which are contained in housings. A number of conventional touchdown bearings are used in the system. At each magnetic bearing location, there is a touchdown bearing with a radial clearance of 0.75 mm. The touchdown bearings used at the magnetic bearing locations are rolling element bearings. In addition, a bronze bush is placed at the driven end of the rotor, with a radial clearance of 0.90 mm, providing protection at that end.

While the AC motor acts as an axial constraint on the rotor, the rotor can move freely radially due to a universal coupling connecting the rotor to the motor. The whole rig is mounted on a bedplate, which is mounted on two pairs of isolators to the ground.

The rotor/bearing test rig, with layout shown in Figure 2.2, was designed and commissioned by Rutland and Keogh (1994a; 1994b; 1995). As part of the research undertaken for this thesis, a force measurement system was designed and installed at the non-driven end of the rig to provide contact force data. The force measurement system incorporates a TDB, in the form of a bronze bush, with an inner diameter of 85.5 mm. This provides a large rotor/TDB radial clearance of 17.75 mm. When rotor/TDB contact tests are performed at that location, a steel sleeve and collar are mounted onto the shaft, so the total rotor diameter becomes 84.8 mm. This gives a rotor/TDB radial clearance value of 0.35 mm. While the small rotor/TDB clearance is useful in performing contact tests, the collar is removed at other times to provide the larger clearance. This applies when the rotor is de-levitated and the system is powered off, or in case other tests are performed where no rotor/TDB contact at that location is desired.

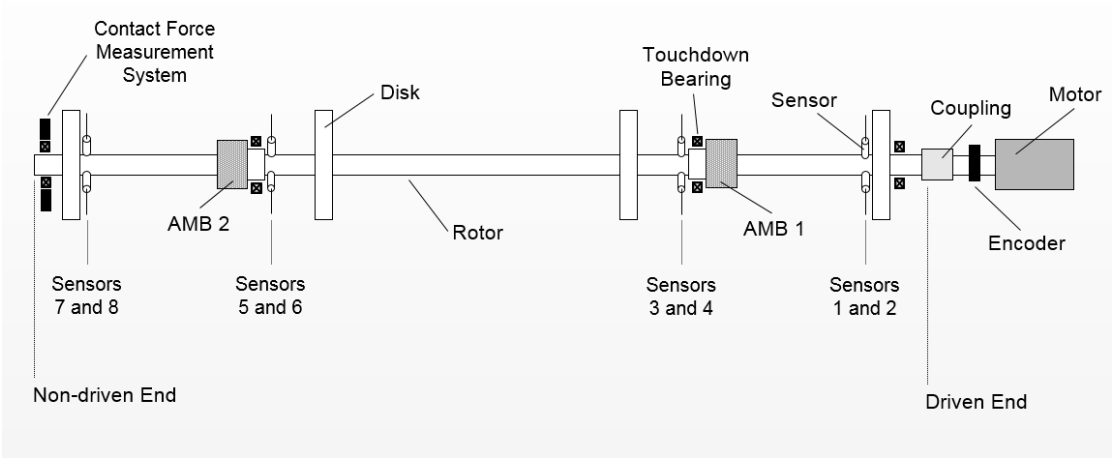

Figure 2.2: Schematic layout of the test rig (top view)

In cases where the rotor/TDB small clearance is not required at the force measurement system location, the AMB TDBs, in addition to the driven end touchdown bush, provide rotor support when the system is powered off. They also offer protection if the load capacity of the magnetic bearings is exceeded.

Since the bearing electromagnets produce a force that increases as the magnetic gap decreases, hence negative stiffness, they are inherently unstable without control. Therefore, closed loop feedback control is used to operate the AMBs. The controllers for both AMBs use position transducer signals. The eight position transducers used are eddy current types, which have a very good frequency response with very small phase shift. This results in good rotor stability. The AC motor is controlled separately by a different controller.

Table 2.1 contains the rotor design specifications, while Table 2.2 contains the disk design data. Other components of the test rig are discussed in more detail in other sections of this chapter.

Table 2.1: Flexible rotor data

Parameter	**Value**
Length	2 m
Radius	25 mm
Total Mass	100 kg
Density	7850 kg/m^3
Young's Modulus	206400 N/mm^2
Maximum Running Frequency	100 Hz

Table 2.2: Disk data

Parameter	Value
Length	35 mm
Outer Radius	120 mm
Inner Radius	25 mm
Mass	10 kg
Density	7850 kg/m^3

2.3 System Rig Components

2.3.1 Active Magnetic Bearings

Each of the two AMBs used in the test rig consists of four opposing pole pairs positioned at ±45 degrees. This is illustrated in Figure 2.3. The specifications of each magnetic bearing are listed in Table 2.3.

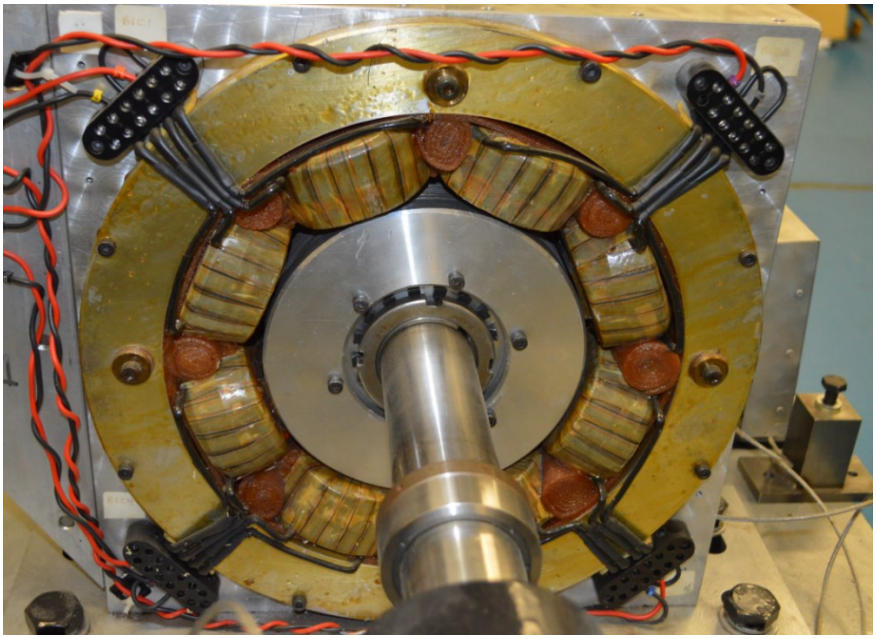

Figure 2.3: A photograph of an AMB used in the experimental facility

For a single coil, an attractive magnetic force can be expressed as

$$F = \frac{1}{2} B H_{gap} A_p \tag{2.1}$$

where B is the flux-current relationship in the coil:

$$B = \frac{\mu_0 N I}{l_{gap} + l_{iron} / \mu_r} \tag{2.2}$$

and H_{gap} is the magnetic field strength within the air gap:

$$H_{gap} = B / \mu_0 \tag{2.3}$$

Table 2.3: Active magnetic bearing data

Parameter	Value
Number of Poles	8
Number of Turns per Pole	158
Pole Face Area/Cross-section	1399 mm^2
Coil Resistance	0.365 Ω
Coil Inductance	0.0732 H
Maximum Coil Current	10 A
Bias Current	4.43 A
Static Current	1.14 A
Maximum Voltage	95.2 V
Maximum Power	952 W
Saturation Force Limit	2000 N
Rotor/Stator Radial Clearance (Magnetic or Air Gap)	1.2 mm

This gives the force equation

$$F = \frac{\mu_0 N^2 I^2 A_p}{2(l_{gap} + l_{iron}/\mu_r)^2} \tag{2.4}$$

If the force of two opposing magnetic poles is considered, the double pole force equation becomes

$$F = \frac{\mu_0 N^2 I^2 A_p}{(l_{gap} + l_{iron} / \mu_r)^2} \cos \lambda \tag{2.5}$$

where λ has a value of 22.5 degrees, which is appropriate for a magnetic bearing with 4 double poles.

Figure 2.4 shows a layout of a double pole magnet. Each two opposing magnets are operated in the bearing, enabling the generation of positive and negative rotor forces. One magnet is driven with the sum of both the bias and control currents, while the other is driven with the difference between the currents. This is referred to as the differential driving mode. Four opposing double pole magnets are operated in each magnetic bearing used in the experimental facility to generate the control forces.

The current I of Equation (2.5) can be separated into two currents for the differential mode. The first one is the one operating the upper coil and is expressed as

$$I_{z+} = I_s + I_b + I_c \tag{2.6}$$

where I_s is a constant current that enables rotor levitation, and I_b is a constant bias current supplied to the coils. These represent the static performance of the AMB. I_c is the current enabling dynamic rotor control.

To generate the control force, I_c is added to the bias current on one side and subtracted on the other side, giving the following current for the lower coil

$$I_{z-} = I_b - I_c \tag{2.7}$$

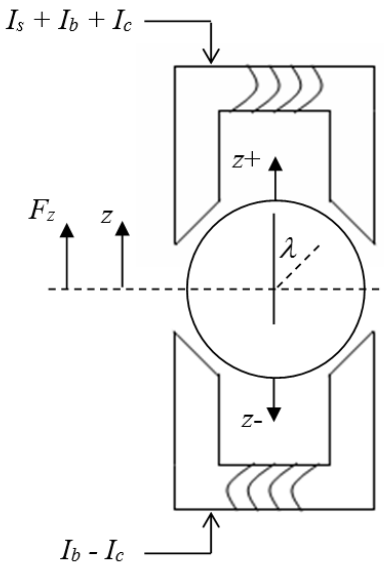

Figure 2.4: Layout of a double pole magnet

The corresponding force relationship is

$$F_z = F_{z+} - F_{z-} \tag{2.8}$$

Thus, Equation (2.5) yields

$$F_z = K_F \left(\frac{(I_s + I_b + I_c)^2}{(l_{gap} - z)^2} - \frac{(I_b - I_c)^2}{(l_{gap} + z)^2} \right) \tag{2.9}$$

where

$$K_F = \mu_0 N^2 A_p \cos\lambda \tag{2.10}$$

In Equation (2.9), the value of l_{iron}/μ_r representing iron magnetisation is neglected, since this value is usually much smaller than the value of l_{gap} due to the relatively high relative permeability value of μ_r.

The force relationship is nonlinear in terms of current and displacement. However, for zero rotor displacement, the relationship can be linearized, where the control current I_c and the displacement z are equal to zero. The force relationship can also be considered linear for small rotor displacements, around the rotor operating point. The linearized equation can be expressed as

$$F_z = K_s z + K_i I_c \tag{2.11}$$

where

$$K_s = \left.\frac{\partial F_z}{\partial z}\right|_{\substack{z=0 \\ I_c=0}} \quad \text{and} \quad K_i = \left.\frac{\partial F_z}{\partial I_c}\right|_{\substack{z=0 \\ I_c=0}}$$

If the force of Equation (2.9) is differentiated to obtain the force-displacement relationship, known as the negative stiffness of the magnetic bearing, expressed as K_s, and the force-current relationship expressed as the current gain K_i, the following equations are obtained

$$K_s = \frac{2K_F}{l_{gap}^3}\left((I_s + I_b)^2 + I_b^2\right) \tag{2.12}$$

$$K_i = \frac{2K_F}{l_{gap}^2}(I_s + 2I_b) \tag{2.13}$$

These equations give values of 2377 N/mm and 563 N/A for K_s and K_i, respectively, using the values of the magnetic bearing design parameters. Rutland and Keogh (1995) performed experimental validation of the magnetic bearings to arrive at the values of K_s and K_i for each magnetic bearing. The change in force acting on the rotor was measured using strain gauges with the variation of rotor displacement and applied current. Figures 2.5 and 2.6 show the variation in force with displacement for each magnetic bearing, where the constant force F_0 is the static force required to levitate

the rotor, which requires I_b and I_s to be applied, and the force f is the control force depending on the control current. A displacement range of ± 0.5 mm was considered. A first-order polynomial fit of the data was done to arrive at the value of the slopes representing the negative stiffness of each bearing. For AMB 1 the value was found to be 1944 N/mm, and for AMB 2 it was found to be 2156 N/mm.

Figures 2.7 and 2.8 show the variation in force with current for each magnetic bearing. A first-order polynomial fit of the data was used to arrive at the value of the slopes representing the current gains for each bearing. For AMB 1 the value was found to be 544 N/A, and for AMB 2 it was found to be 539 N/A.

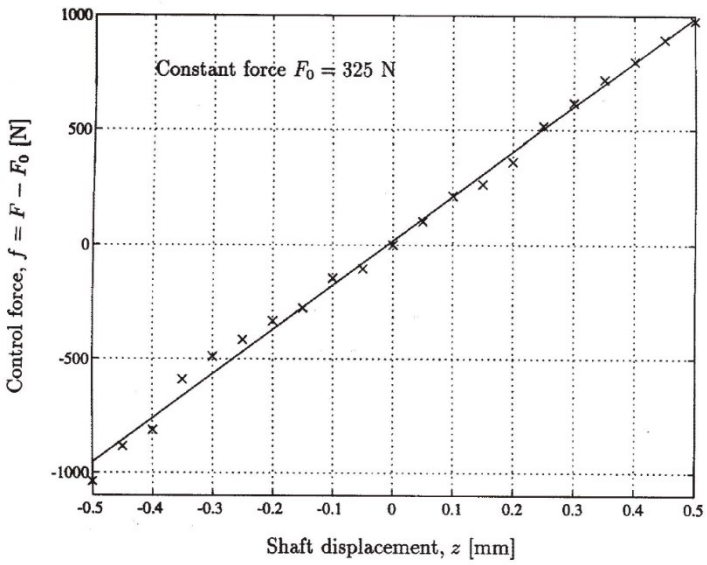

Figure 2.5: Experimental measurements of forces with shaft displacement variation for AMB 1 (Rutland and Keogh, 1995)

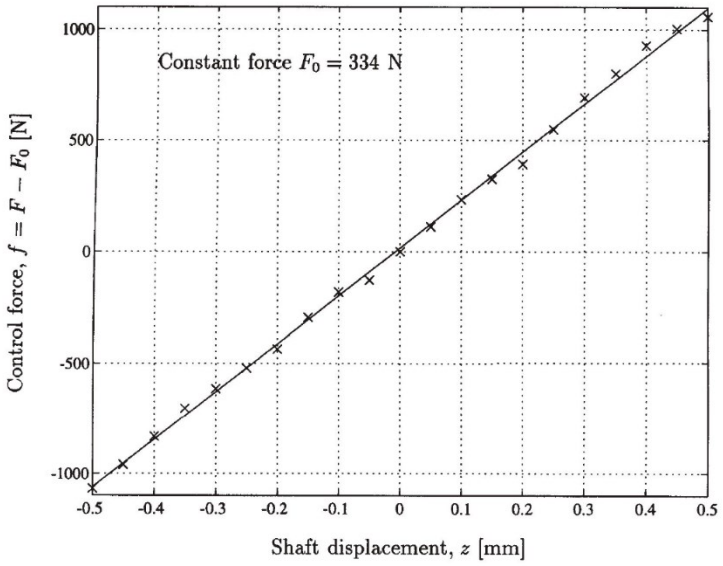

Figure 2.6: Experimental measurements of forces with shaft displacement variation for AMB 2 (Rutland and Keogh, 1995)

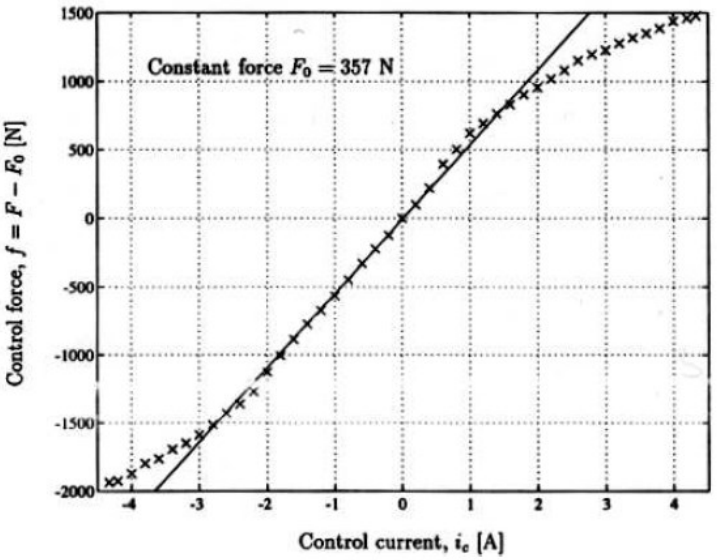

Figure 2.7: Experimental measurements of forces with control current variation for AMB 1 (Rutland and Keogh, 1995)

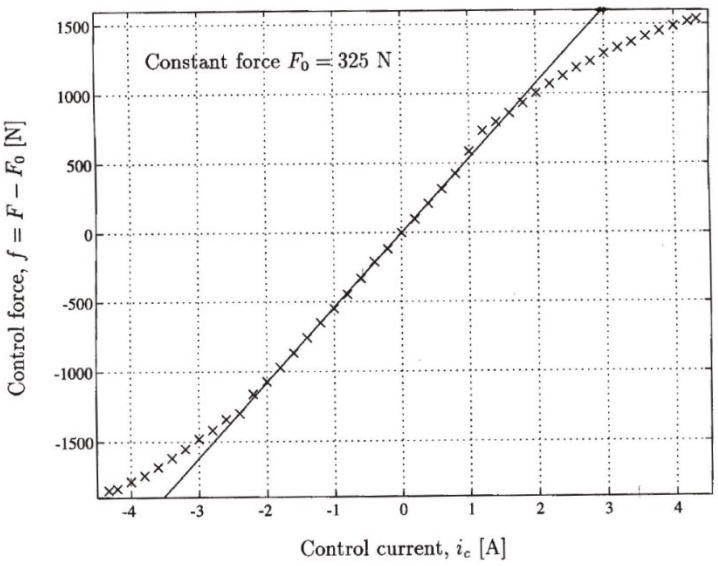

Figure 2.8: Experimental measurements of forces with control current variation for AMB 2 (Rutland and Keogh, 1995)

2.3.2 Power Electronics

Power amplifiers are an essential component of the system, driving the magnetic bearings. The opposing pairs of poles in the magnetic bearings are driven by eight power amplifiers in total. The amplifiers are driven by the controller output signal (voltage) and provide the coils with the appropriate currents with the required gains.

The power amplifiers employed in the test rig are switching amplifiers, commonly used in AMB systems. The way they operate is by switching between positive and negative voltages providing the amplified current. The time ratio between the positive voltage and negative voltage produces the required current. Switching is done at a high frequency. High voltages and high currents are present in the power transistors for short periods in switching amplifiers. This leads to a significant reduction of power loss.

The switching frequency in the amplifiers used is 22 kHz. Other technical specifications are shown in Table 2.4.

Table 2.4: Power amplifier data

Parameter	Value
Input Gain	0.5 A/V
Maximum Output Current	10 A
Signal Bandwidth	1.4 kHz

2.3.3 Displacement Sensors

To control the rotor/bearing system, real-time displacement data are used by the controller. Eddy-current displacement sensors are used. They are capable of high resolution measurements and can be used with any conductive material without contact. These are commonly used in AMB systems. Table 2.5 provides the sensor technical data.

The sensors' bodies are made from stainless steel. The sensors are arranged into four pairs over the rotor. Each pair is 90 degrees apart and each sensor is 45 degrees to the horizontal. This makes the sensors aligned with the pole pairs in the magnetic bearings. Four sensors are located close to both magnetic bearings, just outside the bearing housing. Another four are located near the rotor ends, as shown in Figure 2.2. Figure 2.9 shows the pair of sensors mounted next to the disk at the driven end, and the sensors mounted next to AMB 1.

The sensors measure the rotor displacement and give a voltage output to the controller. The 8 sensors were calibrated against the shaft to provide the voltage-displacement relationship for each sensor. Voltage variation was observed while the sensors were moved away from the shaft covering a displacement range of 0-2 mm. The data obtained are shown in Figures 2.10 and 2.11. A second-order polynomial fit of the data was done for each sensor to arrive at the displacement-voltage relationships. The resulting equations were programmed into the controller.

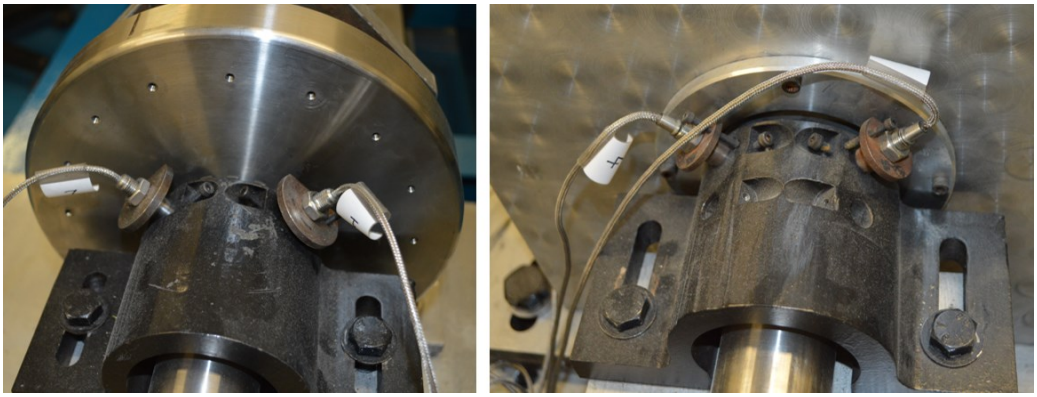

Figure 2.9: Photograph of displacement sensors mounted on the experimental facility at the driven end (left side) and at AMB 1 (right side)

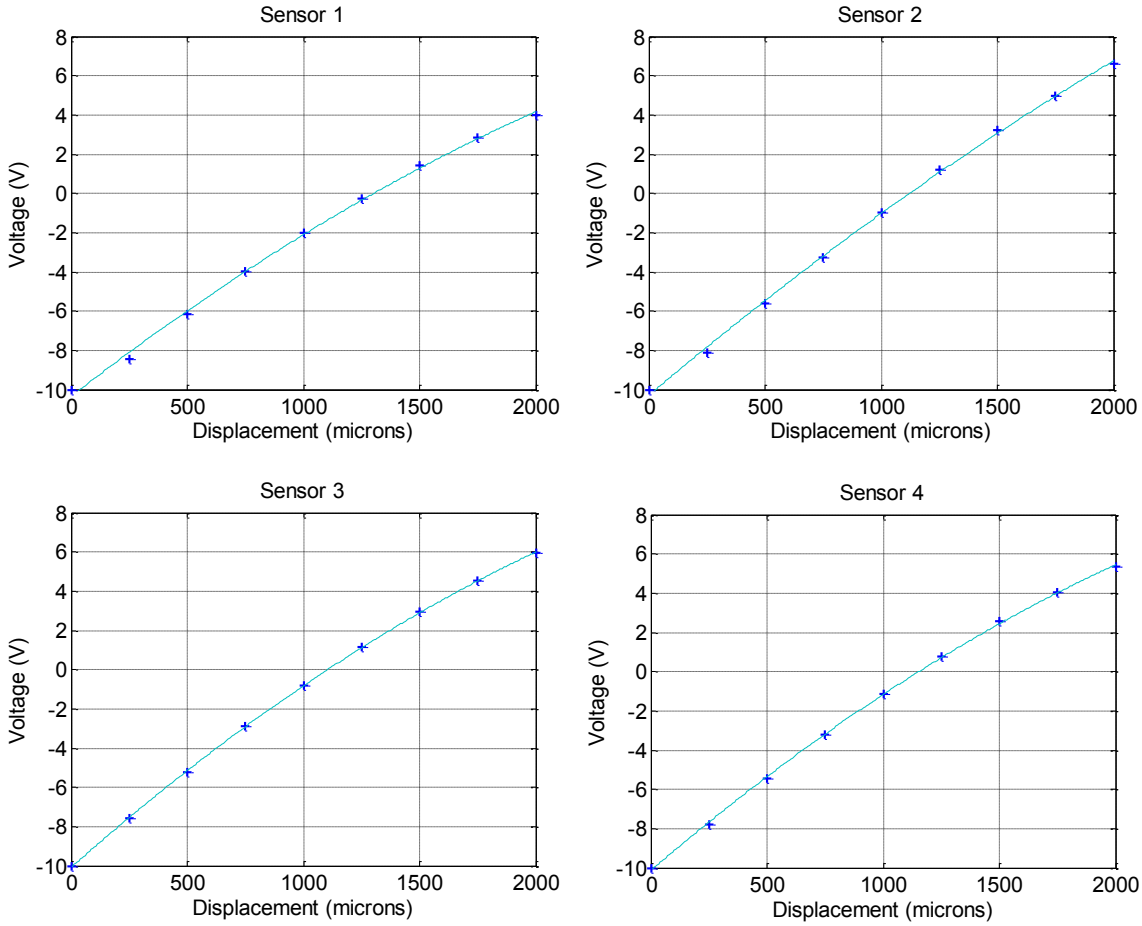

Figure 2.10: Calibration plots for displacement sensors 1 to 4 of the experimental facility

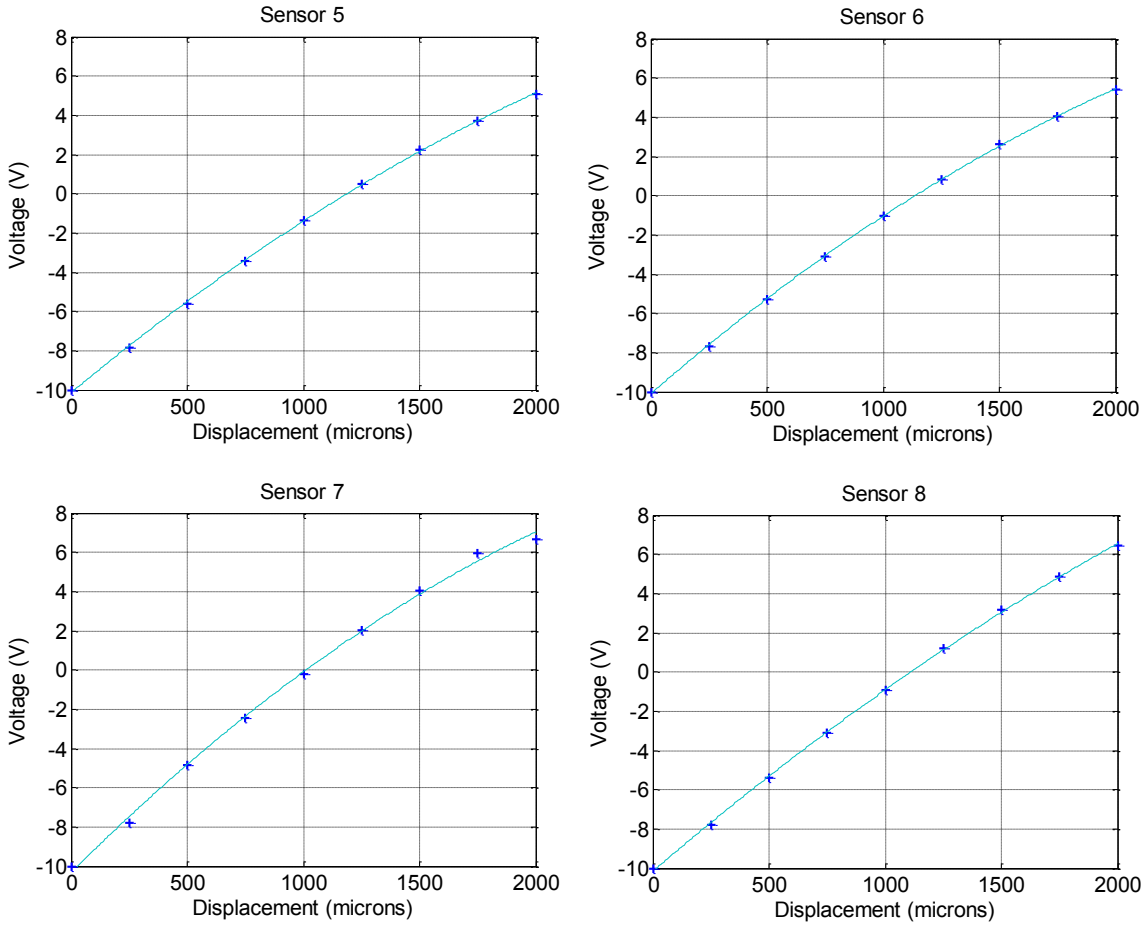

Figure 2.11: Calibration plots for displacement sensors 5 to 8 of the experimental facility

Table 2.5: Eddy-current displacement sensor data

Parameter	**Value**
Power Supply	-24 V DC at 30 mA
Sensitivity	8 mV/μ m
Frequency Range	Up to 10 kHz
Operating Temperature	– 30 to +180 ◦C

2.3.4 AC Motor and Rotor Encoder

An electric AC motor is used to spin the rotor. The shaft connects to the motor with a universal coupling allowing free radial movement. The motor can run with a speed of up to 100 Hz, under its internal control.

An incremental encoder is used to track the shaft rotation and is mounted next to the motor. The encoder features a clamp type mount over the shaft. It is used to provide shaft position information, where its output signal is given as one pulse per revolution. This signal is used in applying synchronous AMB forces, to be able to synchronise the rotor motion with the magnetic bearings. Figure 2.12 shows the encoder, which is mounted on the rotor between the motor and the coupling. Table 2.6 provides the technical data of the encoder.

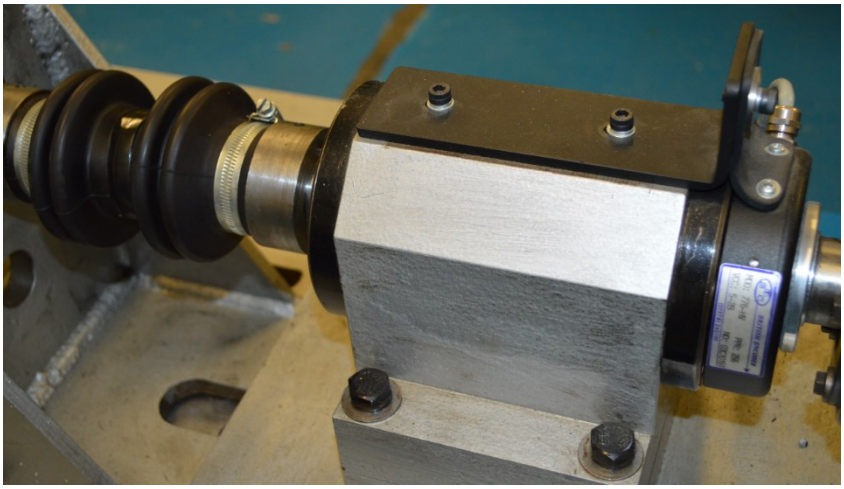

Figure 2.12: A photograph showing the rotor encoder (right side) and the universal coupling (left side)

Table 2.6: Shaft encoder data

Parameter	Value
Output Format	Incremental
Frequency Response	200 Hz
Maximum Input Current	100 mA
Maximum Rotor Frequency	100 Hz
Operating Temperature	0 to 70 ◦C

2.3.5 Force Measurement System

In order to demonstrate the behaviour of the rotor/bearing system in contact conditions experimentally, a method of measuring forces related to rotor/TDB contact was developed. Although the rotor's displacement can be measured using eddy current sensors, the ability to measure forces directly from a TDB was previously non-existent in the test rig. Design methodology is required to incorporate force measurement devices into the TDB or its housing. A design based on strain gauge measurements was commissioned and mounted onto the rotor/magnetic bearing test facility at the non-driven end. This will provide experimental data about a range of contact conditions, which are caused by different input disturbances. The force measurement system is described in detail in Chapter 5.

2.4 Rotor Sag

The eight eddy-current displacement sensors were all installed in a similar way with respect to the rotor. Since the rotor rests on the two AMB touchdown bearings when de-levitated, and the rotor/TDB radial clearance at those locations is 0.75 mm, the rotor displacement in the vertical *Y* direction should be equal to the clearance value when de-levitated. Sensors were installed at an equal distance from the rotor at the sensor locations, giving a rotor vertical displacement value of around -0.75 mm before levitation. When the rotor is levitated, the AMBs control centralises the rotor because of the integral action in the PID control. This is for the rotor in its static state. It is assumed that the rotor is straight in its static condition.

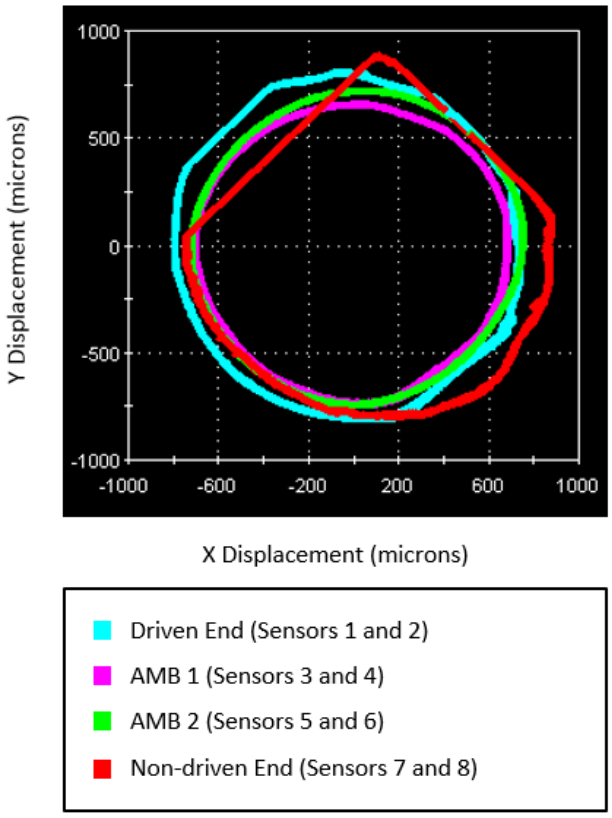

Figure 2.13: Rotor orbits at the four sensor locations showing sensor measurements. An applied AMB force amplitude of 800 N at a 1 Hz whirl frequency was used to generate the orbits

Testing the sensor readings with AMB forces provided orbits such as the orbit shown in Figure 2.13. It is noticed that the sensors at both ends of the rotor do not provide the full range of measurements, giving incomplete orbits. This is particularly noticed with relatively large AMB force amplitudes giving large rotor orbits. No measurement problems were noticed at the AMB locations, where the TDBs are.

To investigate this, a finite element model of a static flexible beam was employed. The rotor was divided into 192 elements. The rotor mass, in addition to the masses of the four disks (10 kg each) and the two AMB cores mounted on the rotor (8 kg each), were taken into consideration at the correct locations. This gives the rotor total mass of a 100 kg. Distribution of rotor weight under gravity was incorporated.

The two AMB TDBs, on which the rotor rests, were modelled as linear springs providing a support stiffness of 1×10^{9} N/m. The rotor displacements in its static state at all locations were considered, resembling the de-levitated rotor. The results are shown in Figure 2.14.

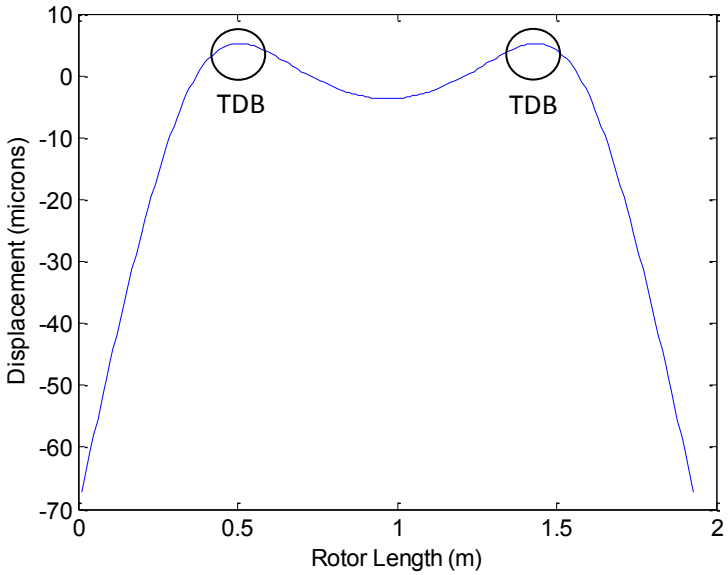

Figure 2.14: Flexible rotor displacement showing rotor bending in its static position while resting on the AMB touchdown bearings

Rotor sag is evident. This particularly affects the displacement sensor measurements at both ends of the rotor. Sag would also affect the rotor in its levitated state. Therefore, the sensors at both the driven and the non-driven ends had to be repositioned to account for the sag effect. This would prevent sensor measurement saturation, giving incomplete measurements. The sensors at both ends were repositioned with respect to the rotor in order to measure the full range of displacements.

2.5 Data Acquisition and Control

A dSPACE hardware and software system is used for data acquisition and for implementing the control system of the test rig. The dSPACE system supports Matlab and Simulink models. This enables controller design to be performed using Matlab/Simulink and applied to the dSPACE system.

The ControlDesk software package of dSPACE provides a full graphical user interface with virtual instrument panels. This enables real-time data monitoring, such as rotor displacement data, and AMB currents data. Additionally, the interface enables modifying system parameters and inputs in real-time, primarily control inputs and parameters.

Data acquisition is done using the capturing capabilities of the software, and that includes recording and saving the data in Matlab compatible formats. The dSPACE hardware acts as the main link between the magnetic bearing rig components and the desktop PC, which runs the control software. Figure 2.15 shows the signal and measurement flow for the test rig components.

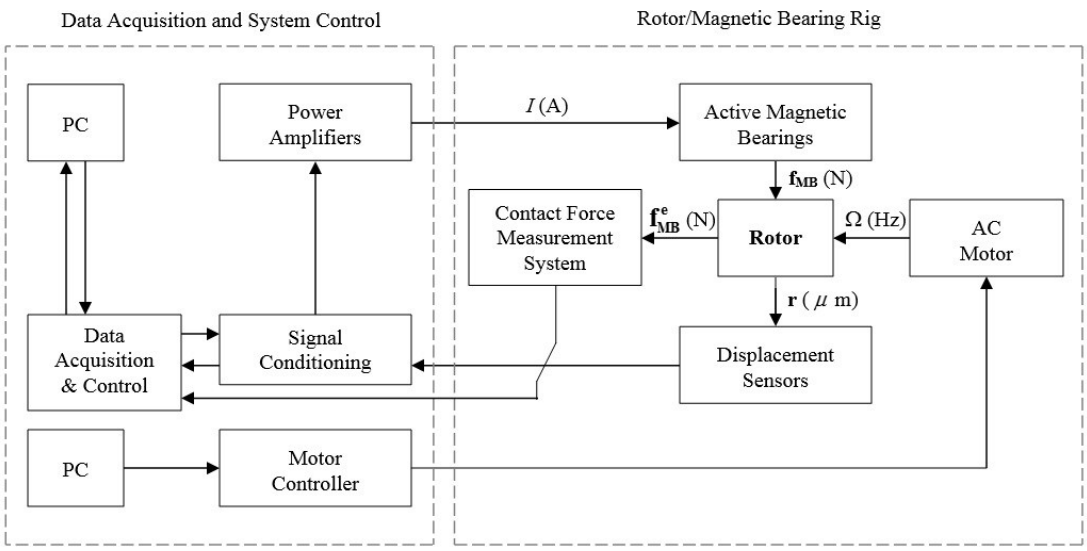

Figure 2.15: Diagram of the magnetic bearing system showing signal and measurement flow

2.6 Closed Loop Control System

The feedback control system shown in Figure 2.16 is used to operate and control the magnetic bearings. This system is used to levitate the rotor and control its motion at all times, relying on displacement sensor measurements. The controller uses the measurements of the two pairs of sensors next to the magnetic bearings.

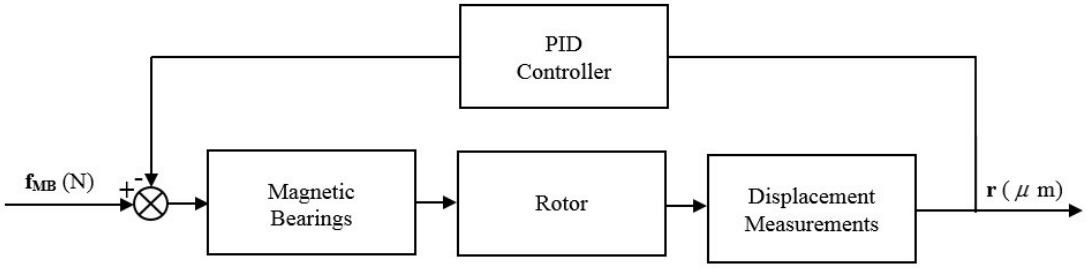

Figure 2.16: Block diagram showing the structure of the closed loop feedback control of the flexible rotor/bearing system

Proportional-Integral-Derivative (PID) control is employed. A separate PID controller is dedicated to each AMB, to enable varying the control parameters for each bearing. An appropriate value of the proportional gain that overcomes the negative stiffness of the magnetic bearings is used. The integral gain is chosen to ensure no steady-state errors and keep the rotor in its centralised position, while the derivative gain is chosen according to system parameters to ensure stability.

The PID controller can have additional control action applied after levitating the rotor, where control inputs can be in the form of appropriately phased AMB forces to perform any required tests. These forces are converted to currents and applied to the coils according to the force-current relationship. The PID controller is implemented using the dSPACE hardware and software through Simulink.

2.7 Closure

The experimental test rig used in this project was described. The design considerations and specifications of the rig components were explained. Measurement data of the displacement sensors and the active magnetic bearings was included. The modelling and behaviour of the active magnetic bearings was discussed and illustrated. Additionally, the data acquisition technique and the control system were described. Issues relating to rotor sag were also assessed so that adjustments could be made to touchdown bearings to achieve rotor concentricity.

Chapter 3

ROTOR/ACTIVE MAGNETIC BEARING SYSTEM MODEL

3.1 Overview

A model of a rotor/AMB/TDB system is described in this section, corresponding to the experimental facility described in the previous chapter. The matrix-vector equation of motion of the system is presented, which is based on finite element analysis. The system components modelling is addressed, including the rotor, the AMBs, and the TDBs. Additionally, the PID control parameters are discussed. The system model is employed in this research to dynamically simulate rotor/TDB contact conditions using Simulink software.

3.2 Finite Element System Model

The rotor/bearing system is modelled using finite element theory. Discretization of the continuous rotor structure into finite elements is performed, where a number of element nodes are formulated to describe the system's motion. The elements of the flexible rotor can be modelled as Euler-Bernoulli beam elements or Timoshenko beam elements. The Euler-Bernoulli beam theory assumes that shaft sections remain plane, and only pure bending is considered to occur. This neglects any shear deformation and assumes negligible distributed rotary inertia. In contrast, the Timoshenko beam theory takes into account the effects of transverse shear, rotary inertia, and gyroscopic moments. In this research, the system was modelled using Timoshenko beam

elements. Nelson and McVaugh (1976) and Nelson (1980) provided a detailed mathematical description of the model. The model employed in this research takes into account radial rotor motion, while axial and torsional displacements are not considered. The disks mounted on the shaft are considered rigid and thin.

The rotor is modelled as a flexible shaft with a constant cross-section consisting of an appropriate number of elements, where each element has two nodes. Each element node has four degrees of freedom expressed by two orthogonal displacements and two angular displacements. These represent translation and rotation in the horizontal and vertical *X* and *Y* axes. Thus, in total, there are 8 degrees of freedom for each element of the rotor. The 4 discs are symmetrically modelled as rigid bodies with four degrees of freedom each, and are applied on the rotor at the correct node positions.

The rotor is discretized into a total of 12 finite elements. This number of elements provides good accuracy to predict the first and second free-free rotor flexure modes, in addition to providing good computing efficiency. This results in 13 element nodes with 52 degrees of freedom. A description of the rotor/AMB system is shown in Figure 3.1, where the locations of the 13 nodes of the finite element model are shown, the first node being on the left. The rotor system model described consists of the rigid discs, the AMB cores, and the distributed parameter finite rotor elements. The AMB nodes are 3 and 11, for AMB 1 and AMB 2, respectively.

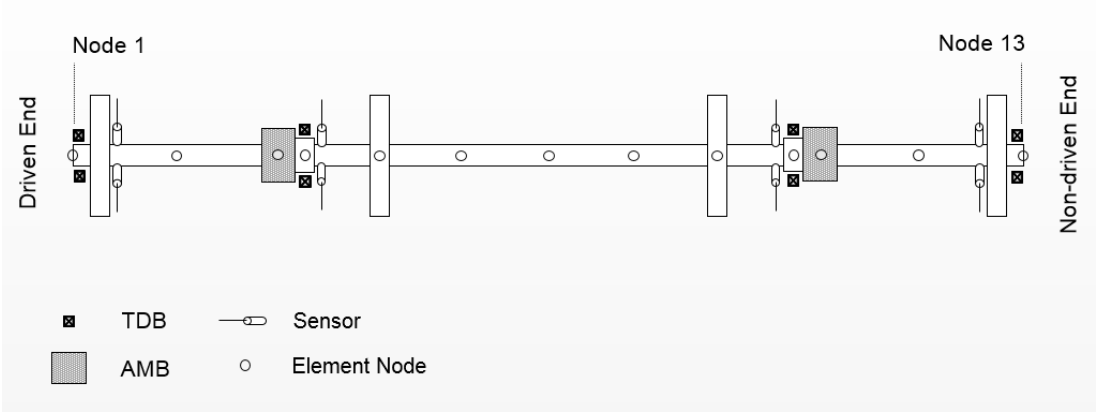

Figure 3.1: Rotor/AMB system description showing the rotor with finite element discretization into 12 elements using 13 element nodes

The equation of motion of the rotor/bearing system consists of the mass, damping and stiffness matrices, and can be expressed as

$$\mathbf{M}\ddot{\mathbf{q}} + \mathbf{D}\dot{\mathbf{q}} + \mathbf{K}\mathbf{q} = \mathbf{f} \tag{3.1}$$

where **M** is the mass matrix consisting of the translational and rotational mass matrices of the disks, AMB cores and rotor elements, written as

$$\mathbf{M} = \mathbf{M}_{\mathbf{T}} + \mathbf{M}_{\mathbf{R}} \tag{3.2}$$

D is the damping matrix incorporating rotor gyroscopic effects, and **K** is the stiffness matrix.

The input vector of forces at the appropriate nodes incorporates the magnetic bearing forces in addition to applied unbalance forces and is expressed as

$$\mathbf{f} = \mathbf{f}_{\mathbf{u}} + \mathbf{f}_{\mathbf{MB}} \tag{3.3}$$

State-space representation is used for the rotor's dynamic model for the purpose of computer simulations. The state-space form of the equations of motion is

$$\begin{aligned} \dot{\mathbf{x}}_{\mathbf{s}} &= \mathbf{A}_{\mathbf{s}}\mathbf{x}_{\mathbf{s}} + \mathbf{B}_{\mathbf{s}}\mathbf{u}_{\mathbf{s}} \\ \mathbf{y}_{\mathbf{s}} &= \mathbf{C}_{\mathbf{s}}\mathbf{x}_{\mathbf{s}} + \mathbf{D}_{\mathbf{s}}\mathbf{u}_{\mathbf{s}} \end{aligned} \tag{3.4}$$

where $\mathbf{x}_{\mathbf{s}} = \left[\mathbf{q}^T, \dot{\mathbf{q}}^T\right]^T$ is the model state vector, while $\mathbf{u}_{\mathbf{s}}$ and $\mathbf{y}_{\mathbf{s}}$ are the input and output vectors, respectively. For the rotor/AMB system, the system matrix $\mathbf{A}_{\mathbf{s}}$ is expressed as

$$\mathbf{A}_{\mathbf{s}} = \begin{bmatrix} \mathbf{0} & \mathbf{I} \\ -\mathbf{M}^{-1}\mathbf{K} & -\mathbf{M}^{-1}\mathbf{D} \end{bmatrix}$$

and

$$\mathbf{B}_s = \begin{bmatrix} \mathbf{0} \\ \mathbf{M}^{-1} \end{bmatrix} \qquad \mathbf{u}_s = \mathbf{f}$$

3.3 Active Magnetic Bearings Model

3.3.1 Nonlinear Modelling

Nonlinear AMB system modelling is described by Schweitzer *et al.* (1994). In Chapter 2 of this thesis, a linearized model of the AMB characteristics was considered. However, the linearized AMB force equation used for the test rig analysis was modified to account for the nonlinearities and force saturation present in real data. The nonlinear behaviour of AMB forces can be specifically seen in Figures 2.7 and 2.8, which provide experimental measurements. Considering the double pole arrangement of the magnetic bearings, the nonlinear AMB force in a single axis can be expressed as

$$F_z = \frac{K_F}{k}\left(\frac{\tanh\left(k\left(I_s + I_b + I_c\right)^2\right)}{\left(l_e - z\right)^2} - \frac{\tanh\left(k\left(I_b - I_c\right)^2\right)}{\left(l_e + z\right)^2} \right) \tag{3.5}$$

where

$$K_F = \mu_0 N^2 A_p \cos\lambda$$

$$l_e = l_{gap} + \left(l_{iron} / \mu_r\right)$$

and k is a characteristic constant. This equation gives similar AMB behaviour in the model to real measurements.

3.3.2 Control Parameters

The negative stiffness induced instability of the AMBs is stabilised by a PID controller. The AMB force of Equation (3.5) may be linearized in terms of the current and displacement gains as

$$F_z = K_s z + K_i I_c \tag{3.6}$$

Expressions for K_s and K_i were provided in Equations (2.12) and (2.13). If the proportional and derivative gains of feedback control are considered, the control current I_c can be represented as

$$I_c = -K_P z - K_D \dot{z} \tag{3.7}$$

Substituting Equation (3.7) into Equation (3.6) yields

$$F_z = -((K_i K_P - K_s) z + K_i K_D \dot{z}) \tag{3.8}$$

$K_i K_P - K_s$ represents the magnetic bearing stiffness, and $K_i K_D$ represents the magnetic bearing damping. Integral gain is added to the controller to minimise steady-state errors of the levitated rotor during operation. Thus, a proportional-integral-derivative (PID) controller is implemented in the system model corresponding to the AMB PID control of the experimental rig.

The closed loop rotor critical frequencies can be obtained, which are dependent on the AMB gains. This can be done using the system matrix $\mathbf{A_s}$ and deriving the eigenvalues. If the AMB proportional and derivative gains are chosen to be $K_i K_P$ = 3×10^6 N/m, and $K_i K_D$ =3500 Ns/m, respectively, the rotor's natural frequencies are found to be at 13 Hz, 19 Hz, 29 Hz, and 70 Hz, approximately. The first two frequencies correspond to dominantly rigid body rotor motion, specifically the conical and cylindrical modes. The last two frequencies correspond to the symmetric and antisymmetric flexural modes of the rotor.

3.4 Touchdown Bearing Model

This section describes rotor/TDB contact force formulation using a TDB model. The model is applied using the finite element analysis of the rotor at the correct nodes, representing all the TDBs in the system. The nonlinear model presented is based on models developed and described by a number of researchers including Xie *et al.* (1999) and May (2001). Keogh and Cole (2003) presented a nonlinear contact model with a TDB undergoing localised contact with the rotor, where different rotor contact modes were assessed involving a flexible rotor. The TDB model is based on a linear mass-spring-damper system representation, where the TDB itself is resiliently mounted but considered rigid. Nonlinearity arises between the rotor and the inner race of the bearing as a result of nonlinear contact stiffness. The nonlinear contact stiffness was derived by Roark and Young (1975) based on the case of cylinder on cylinder contact. The nonlinear stiffness is induced by a Hertzian stress formulation at the specific contact location, where the compressive force on the TDB introduces normal surface deformations. It is assumed that the strains are considered small and are within the TDB's material elastic limit. Damping effects of the localised contact are neglected, because they are considered small compared the damping arising from the TDB mounting.

Rotor/TDB contact introduces contact forces normal to the TDB surface at the contact point. Tangential friction forces at the contact point are related to the normal contact forces via a coefficient of friction, characterising Coulomb friction. Dynamic Coulomb friction has been used by researchers developing contact models for rotor systems, and is considered adequate for that purpose. The total rotor/TDB contact forces are determined as the resultant of the normal contact forces and the friction forces.

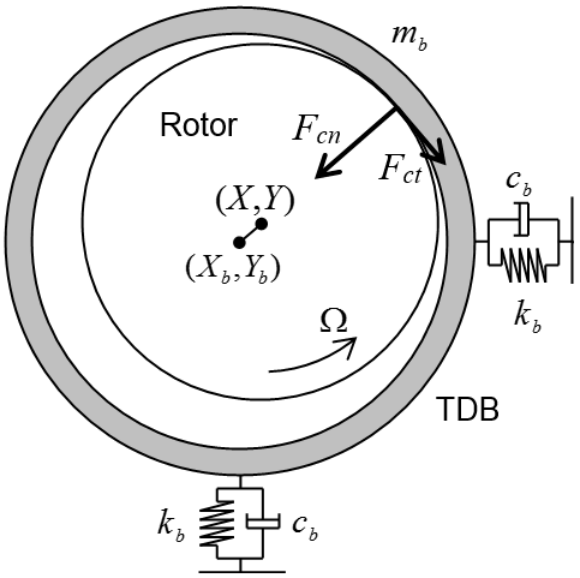

Figure 3.2: Schematic of rotor/TDB showing possible rotor/TDB contact

Since the rotor displacement can be defined in terms of the coordinates X and Y, if the X and Y axes displacements of the TDB are X_b and Y_b, respectively, as shown in Figure 3.2, the equations of motion of the TDB in the X and Y directions can be expressed as

$$\begin{aligned} m_b\ddot{X}_b + c_b\dot{X}_b + k_bX_b &= F_{cn}\cos\theta_c - F_{ct}\sin\theta_c \\ m_b\ddot{Y}_b + c_b\dot{Y}_b + k_bY_b &= F_{cn}\sin\theta_c + F_{ct}\cos\theta_c \end{aligned} \tag{3.9}$$

where

$$\theta_c = \tan^{-1}\left(\frac{Y - Y_b}{X - X_b}\right) \tag{3.10}$$

The force F_{cn} is the normal contact force, while F_{ct} is the tangential force, which is a function of rotor/TDB friction, expressed as

$$F_{ct} = \mu F_{cn} \operatorname{sgn}(V) \tag{3.11}$$

where V is the relative velocity between the rotor and the TDB expressed as

$$V = \Omega r - (\dot{Y} - \dot{Y}_b)\sin\theta_c + (\dot{X} - \dot{X}_b)\cos\theta_c \tag{3.12}$$

Dynamic friction occurs as a result of the slipping motion between the rotor and TDB surfaces, where friction is opposite in direction to the direction of slipping. Equation (3.11) takes into account the direction of slipping at the contact point, using the calculation of the relative velocity. If the tangential friction force is high, rotor backward whirl motion can occur, which is damaging to the system. The difference in displacement between the rotor and bearing centres is represented by

$$\delta R = \sqrt{(X - X_b)^2 + (Y - Y_b)^2} \tag{3.13}$$

Rotor/TDB contact only occurs if

$$\delta R \geq c_R$$

where c_R is the radial rotor/TDB clearance, which is the difference between the rotor and the TDB radii. The normal contact force induced on the rotor during rotor/TDB interaction is a function of the nonlinear contact stiffness and the depth of penetration. The contact force amplitude is related to δR by the following expression

$$\delta R - c_R = \frac{2F_{cn}(1-\nu^2)}{\pi E l_c}\left(\frac{2}{3} + \ln\frac{8El_c c_R}{2.15^2 F_{cn}}\right) \tag{3.14}$$

where $\delta R - c_R$ is the penetration depth, and l_c is the circumferential contact patch length.

3.5 Sensors/Bearings Non-collocation

The choice of displacement sensor positions in the rotor/AMB system can have an influence on controller stability, and will affect identifying the dynamics of the system. Although sensors are positioned as close as possible to the bearing locations on the experimental rig, sensor/bearing non-collocation exists. The sensor pairs employed by the PID controllers are the AMB location sensors, which are positioned very close to the AMB locations. This makes them nearly collocated with the AMB TDBs. However, there is a more significant difference in position along the rotor between the sensors and the other TDBs. Sensors/TDBs at both ends of the rotor are considered non-collocated. Therefore, they do not provide the exact displacements of the rotor at the TDB locations.

The 13 node system model presented in the first section of this chapter considers the displacements at the TDB nodes, which is where the TDBs are positioned along the rotor. However, since the sensors on the experimental rig are non-collocated, offsets in the displacements will occur between experimental and simulation results at TDB locations due to the non-collocation of sensors coupled with rotor flexibility. The 13 node model was employed to undertake initial simulations identifying the effect of rotor unbalance on rotor/TDB contact. The model was modified into a 17 node model to enable comparison between experimental and simulation results. The 4 extra nodes represent the displacement sensors positions. The 17 node model is described in Figure 3.3.

Although other issues influence differences between simulation and experimental results, such as measurement errors/noise, and rotor/TDB misalignment problems, predicting displacements at the actual sensor positions will increase model accuracy.

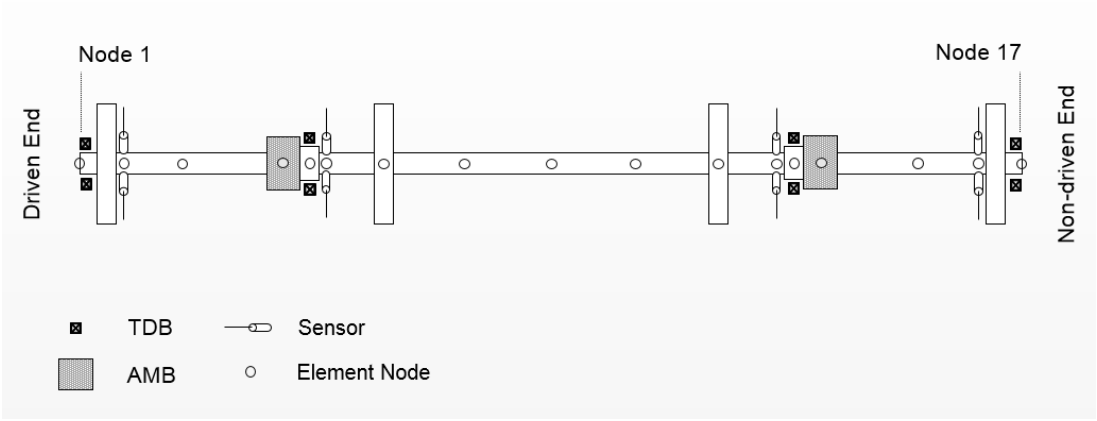

Figure 3.3: Rotor/AMB system description showing the rotor with finite element discretization into 16 elements using 17 element nodes

3.6 System Response Representation

Displacement data can be represented in different ways. This includes orbital plots obtained directly from the X and Y stationary coordinates, and plots using rotating frame coordinates. A rotating frame is employed to plot displacement data rotating with the rotor's speed Ω. This is described in Figure 3.4.

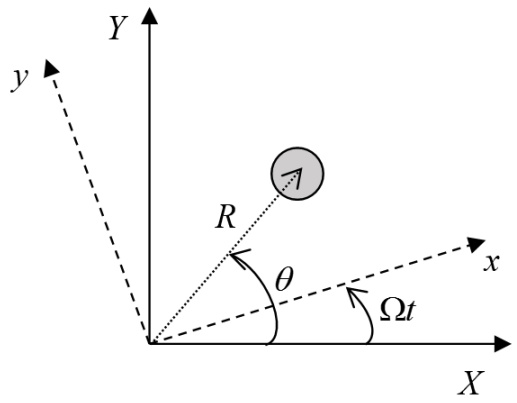

Figure 3.4: Description of the rotating frame coordinates

The displacement amplitude of the rotor is expressed as

$$R = \sqrt{X^2 + Y^2} \tag{3.15}$$

The phase angle is expressed as

$$\theta = \sin^{-1}\left(\frac{Y}{R}\right) \tag{3.16}$$

The relationship between the stationary and rotating frame coordinates is defined as

$$\begin{aligned} x &= X\cos(-\Omega t) - Y\sin(-\Omega t) \\ y &= Y\cos(-\Omega t) + X\sin(-\Omega t) \end{aligned} \tag{3.17}$$

3.7 Closure

A description of the rotor/AMB/TDB system model was presented in this chapter. The equation of motion of the finite element rotor was presented. Nonlinear modelling of the AMBs and of rotor/TDB interaction was described and discussed. The PID control parameters of the AMBs were also discussed. Sensor/bearing non-collocation was addressed, where a modified system model was presented. In addition, the response representation of rotor motion was presented. The system model presented is employed in the prediction of rotor/TDB interaction.

Chapter 4

ROTOR/TOUCHDOWN BEARING CONTACT MODES

4.1 Overview

Simulation tests for the evaluation of the dynamic performance of the rotor/bearing system during contact conditions are presented in this chapter. The aim is to identify possible rotor/TDB contact modes and behaviours due to rotor unbalance over a range of frequencies. Different rotor unbalance forces are applied to generate rotor/TDB contact, resembling potential external faults or disturbances. Rotor/TDB contact behaviour is observed and analysed. Two types of tests are performed. The first involves varying the rotating speed of an unbalanced rotor, and the second involves introducing and removing unbalance at a constant rotating speed. Further simulation results are presented in Chapter 6, where the dynamics of the force measurement system are explored.

4.2 Contact at Various Rotating Frequencies

The rotor/AMB/TDB 13 node system model was employed to perform a series of simulation tests to explore and identify the dynamic contact behaviour of the system. The TDB parameters employed to investigate contact behaviour are shown in Table 4.1. The parameters correspond to a non-driven end TDB with a radial rotor/TDB clearance of 0.7 mm. The non-driven end is where rotor/TDB contact occurs as

determined by the unbalance imposed in the tests. The PID control parameters used are shown in Table 4.2.

Table 4.1: TDB parameters at the non-driven end

Parameter	Value
Bearing support damping coefficient (Ns/m)	1×10^{4}
Bearing support stiffness (N/m)	2×10^{8}
Coefficient of friction	0.15
Radial rotor/TDB clearance (m)	0.7×10^{-3}

Table 4.2: PID control parameters

PID Control Parameter	AMB 1	AMB 2
$K_i K_P$ (N/μm)	3	3
$K_i K_I$ (N/s/μm)	0.3	0.3
$K_i K_D$ (Ns/μm)	0.005	0.005

The rotor/bearing system response to mass unbalance was simulated. The unbalance force, which was applied in X and Y directions, is expressed as

$$\begin{aligned} F_{uX} &= me\Omega^2 \cos\Omega t \\ F_{uY} &= me\Omega^2 \sin\Omega t \end{aligned} \tag{4.1}$$

An unbalance represented by a value of *me* = 3 gm was introduced to the system at node 13 to observe rotor/TDB interaction at the non-driven end. Multiple simulation tests were undertaken to explore the behaviour of rotor/TDB interaction at different rotating frequencies. The rotor was run at a rotating speed range of 0 to 32 Hz. Figure 4.1 shows the relationship between the rotating frequencies and unbalance forces as the rotor frequency is increased. The force in the figure represents the resultant unbalance force amplitude obtained from the *X* and *Y* forces.

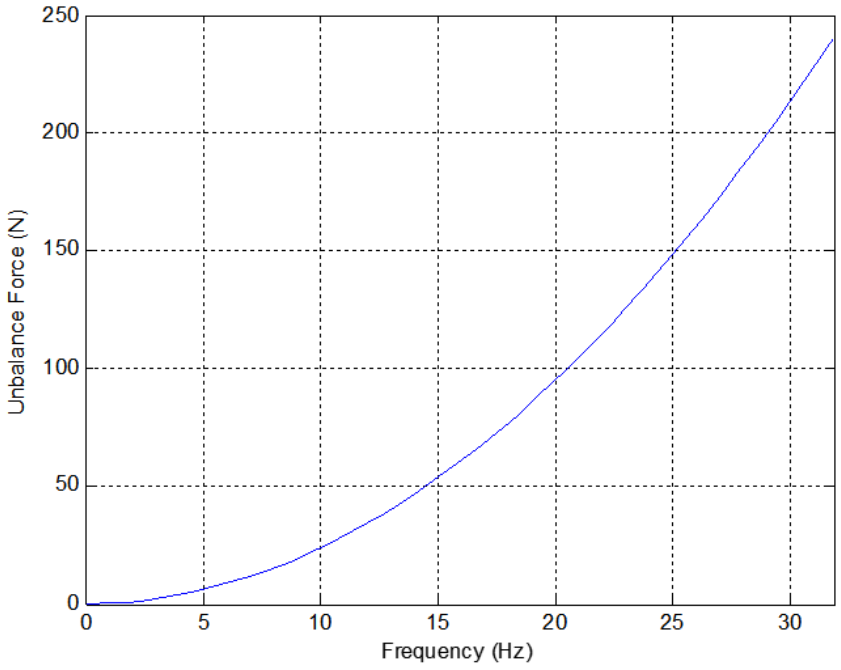

Figure 4.1: Variation of unbalance force with the rotating speed at the non-driven end for an unbalance of 3 gm

The maximum value of the unbalance force reached in this case is 240 N for the 3 gm unbalance. The steady-state displacement amplitude of the rotor, *R*, is plotted against the same range of running frequencies in Figure 4.2, which illustrates the values of the steady-state displacements of the rotor at each rotating speed. Initially, an increase in the displacement amplitude is observed up to 0.5 mm. That displacement amplitude continues until a rotating speed of 18.3 Hz. A small change in the displacement amplitude is observed between the frequencies of 18.3 and 19.9 Hz. However, that is

followed by an increase of the amplitude with a larger rate in the speed range from 19.9 to 24.7 Hz. After that, rotor/TDB contact occurs as the amplitude reaches its maximum value, which is the rotor/TDB radial clearance value, at speeds of 24.7 Hz to 32 Hz.

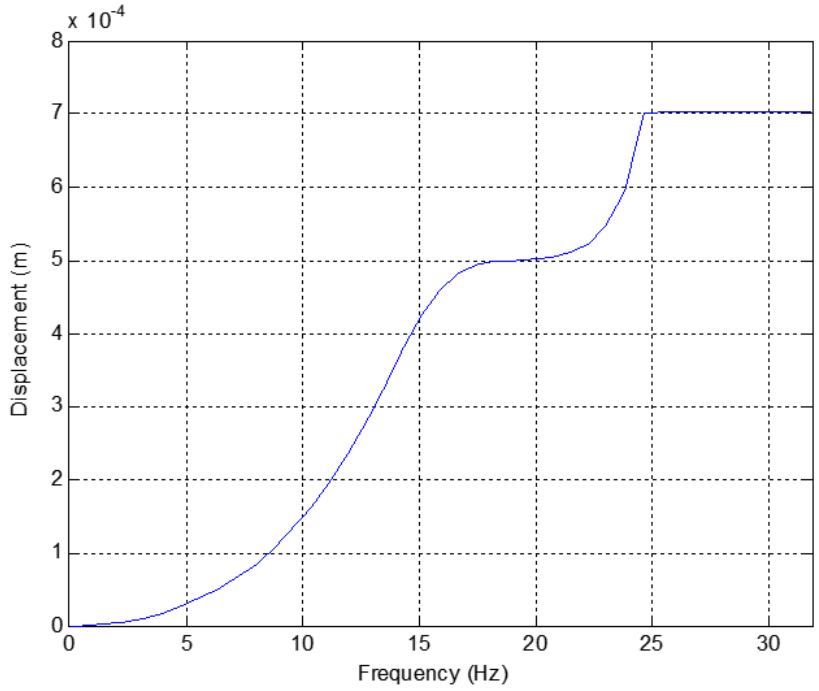

Figure 4.2: Rotor steady-state displacement amplitudes at the non-driven end over a rotating speed range of 0-32 Hz with an unbalance of 3 gm

The different contact modes that occur within the speed range considered at the given value of unbalance are mapped and described in Figure 4.3. It is noted that the first contact case occurs at a speed of 21.5 Hz. Different contact modes are present up to the speed of 32 Hz. At 21.5 Hz, transient rotor/TDB contact occurs, rather than continuous steady-state contact. Steady-state persistent contact only starts occurring at a speed of 24.7 Hz as can be seen from Figure 4.2.

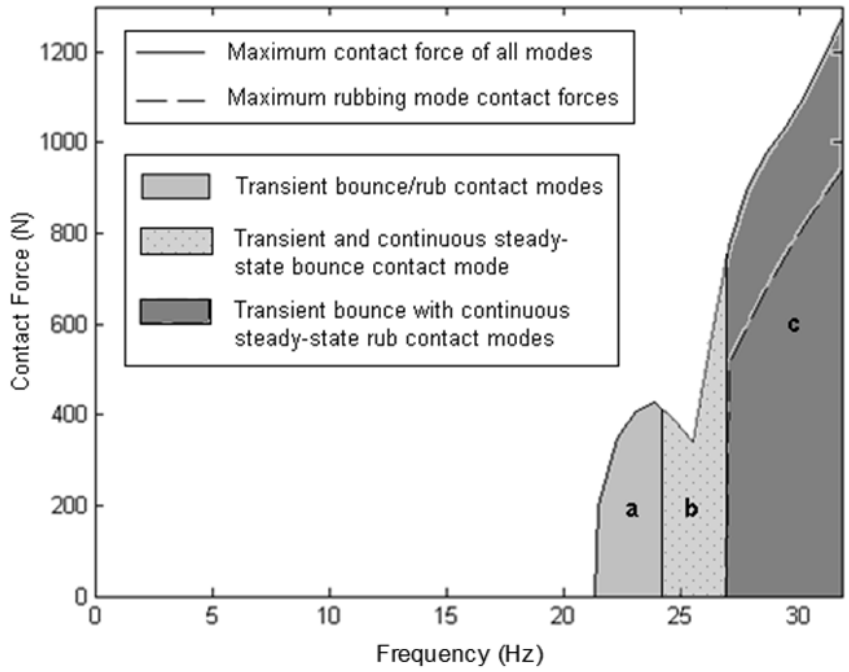

Figure 4.3: Various modes of rotor/TDB contact for an unbalance of 3 gm at the non-driven end over rotating speeds (a) 21.5-24.7 Hz (b) 24.7-27 Hz (c) 27-32 Hz

The maximum contact forces in regions (a), (b) and (c) of Figure 4.3 are 428 N, 760 N and 1279 N respectively. The maximum rub mode contact force in region (c) is 940 N. The behaviour of contact cases corresponding to regions (a), (b) and (c) are presented in Figures 4.4 to 4.9. Contact force variation with time is explored. Additionally, rotor orbits are plotted to illustrate the contact behaviour, using rotating frame displacement coordinates x and y.

Figure 4.4 illustrates the contact force behaviour for a running speed of 23 Hz, which exists in region (a) of Figure 4.3. Transient bounce and rub contact modes are observed, which continue up to 0.09 s. The maximum value of the transient contact forces observed in this case is 410 N. Figure 4.5 shows the corresponding rotor displacements, illustrating the contact modes.

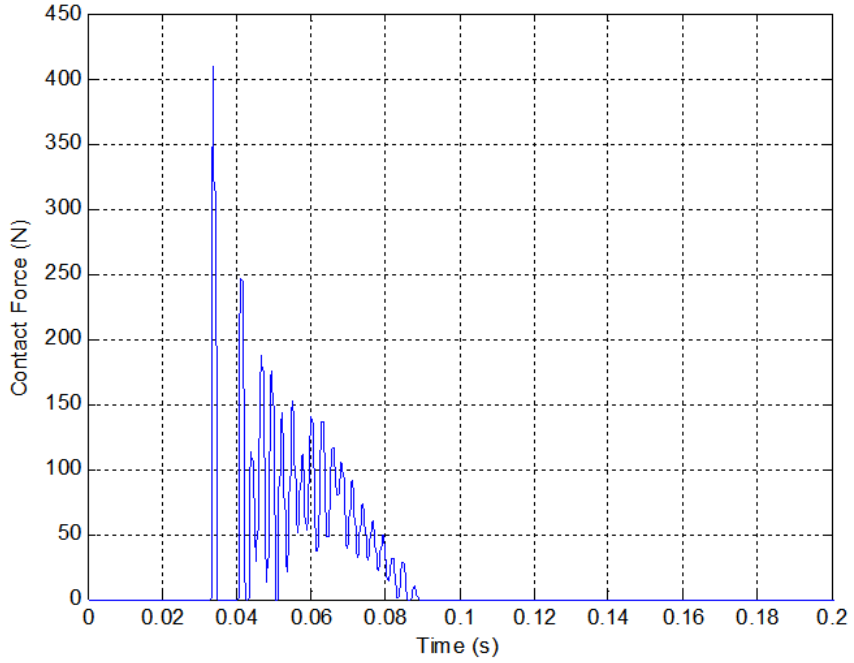

Figure 4.4: Rotor/TDB contact forces at the non-driven end for a rotating speed of 23 Hz

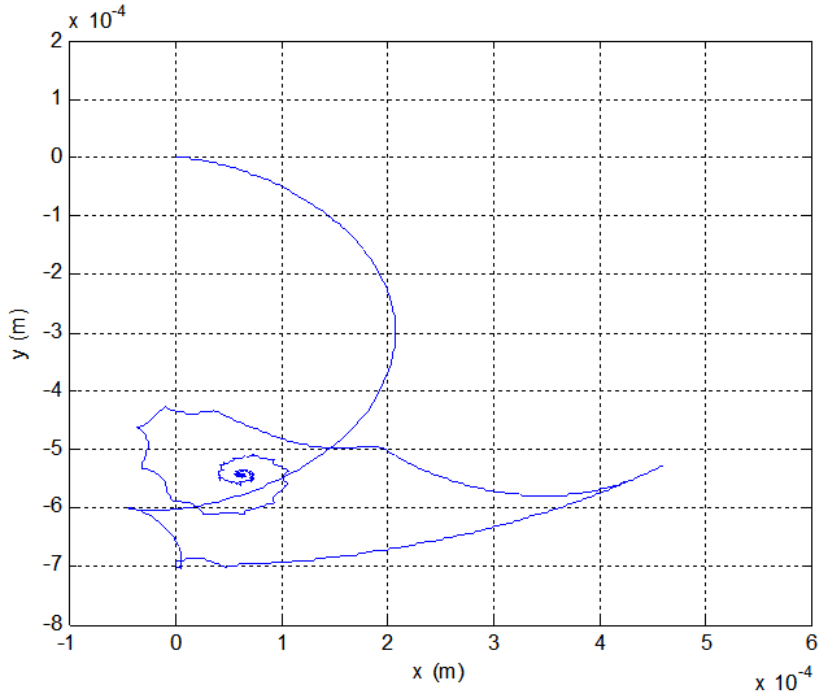

Figure 4.5: Rotor displacements in rotating frame coordinates showing a transient bounce/rub contact mode at the non-driven end at a speed of 23 Hz

Continuous rotor bouncing behaviour is observed in region (b) of Figure 4.3. Figures 4.6 and 4.7 show the contact forces and the corresponding rotor displacements for a rotating speed of 25.5 Hz, which exists in region (b). A maximum contact force of 339 N is evident, representing the transient response. The maximum steady-state bounce mode forces are around 285 N.

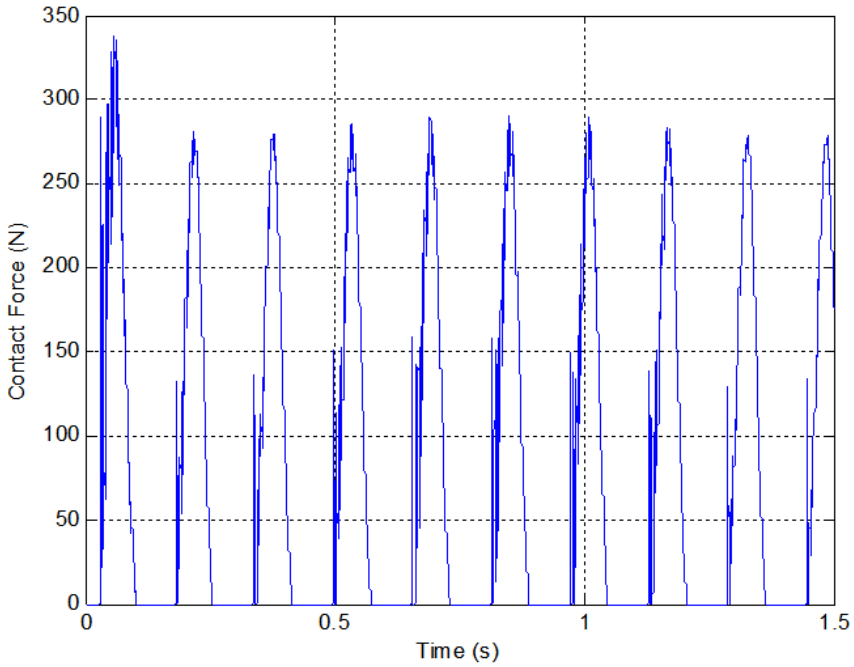

Figure 4.6: Rotor/TDB contact forces at the non-driven end at a rotating speed of 25.5 Hz

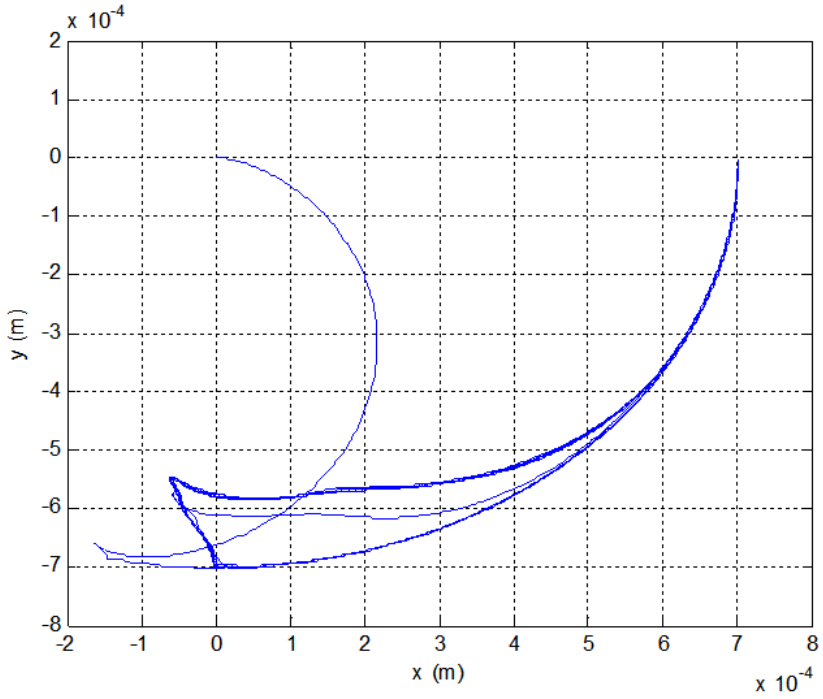

Figure 4.7: Rotor displacements in rotating frame coordinates showing a persistent bounce contact mode at the non-driven end at a speed of 25.5 Hz

For higher rotating speeds from 27 Hz up to 32 Hz, persistent rotor rub is observed. Rotor rub takes place within this range after transient bounce motion occurs. This corresponds to region (c) of Figure 4.3. An example of this behaviour is shown in Figures 4.8 and 4.9 for a rotating speed of 29.4 Hz. It is noticed from Figure 4.8 that the contact force reaches a high value of 1035 N in the transient phase of the response. The response stabilises after 0.25 s to a steady-state value of 280 N. It was observed for the cases corresponding to region (c) of Figure 4.3 that as the running speed increases, the time taken for the response to stabilise into the steady-state behaviour decreases.

The different effects of changing the running speed of an unbalanced rotor were demonstrated in the tests performed in relation to rotor/TDB contact. Different types of contact modes are possible, including transient and persistent steady-state modes. The tests identify rotor/TDB contact dynamics that should be considered when assessing control methods aimed at contact-free recovery of the rotor.

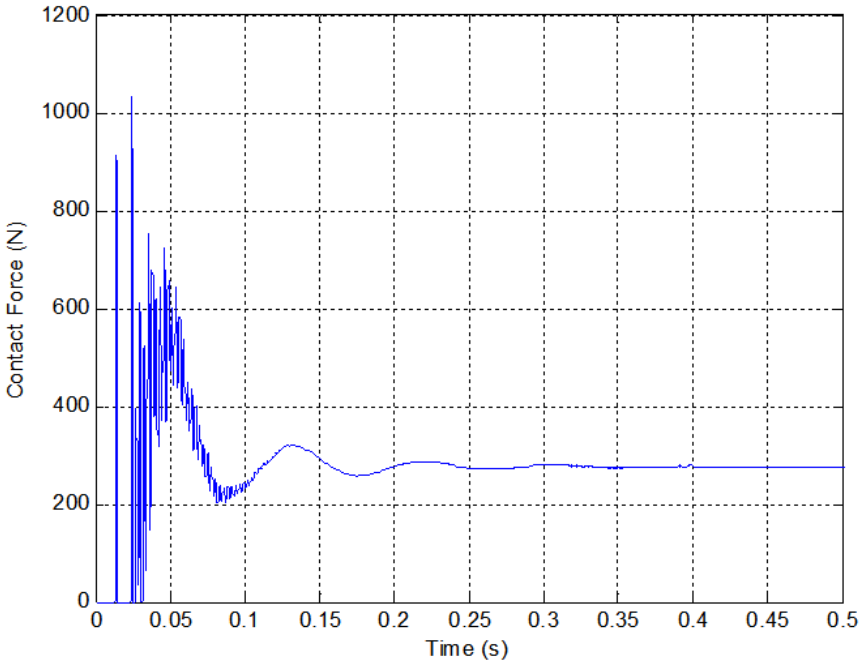

Figure 4.8: Rotor/TDB contact forces at the non-driven end at a rotating speed of 29.4 Hz

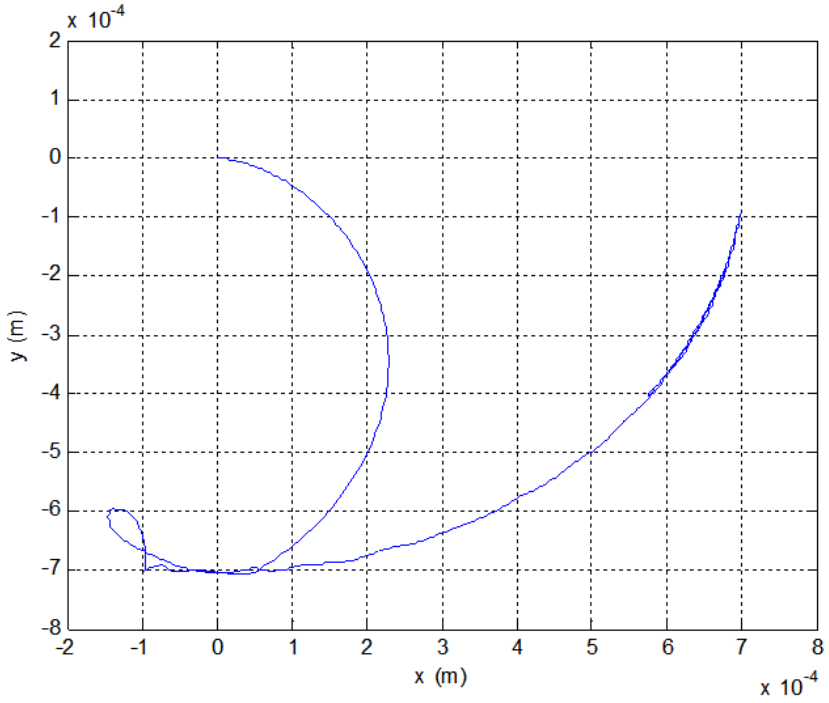

Figure 4.9: Rotor displacements in rotating frame coordinates showing a transient bounce contact mode and a persistent rub contact mode at the non-driven end at a speed of 29.4 Hz

4.3 Contact with Variable Rotor Unbalance

In this section, the behaviour of rotor/TDB interaction is observed after introducing variable rotor unbalance levels over a constant running frequency. Unbalance levels were increased to initiate contact, then the unbalance was removed to recover the rotor to a non-contact case. Figure 4.10 shows how the value of *me* of Equation (4.1) was varied linearly with time during the simulations, illustrating run-up to rotor/TDB contact, and run-down removing the unbalance forces causing the contact. The varying unbalance profile described in Figure 4.10 was employed in the different tests undertaken. However, different values of *me*, and different run-up and run-down time durations were explored. Tests were performed at a number of different running speeds.

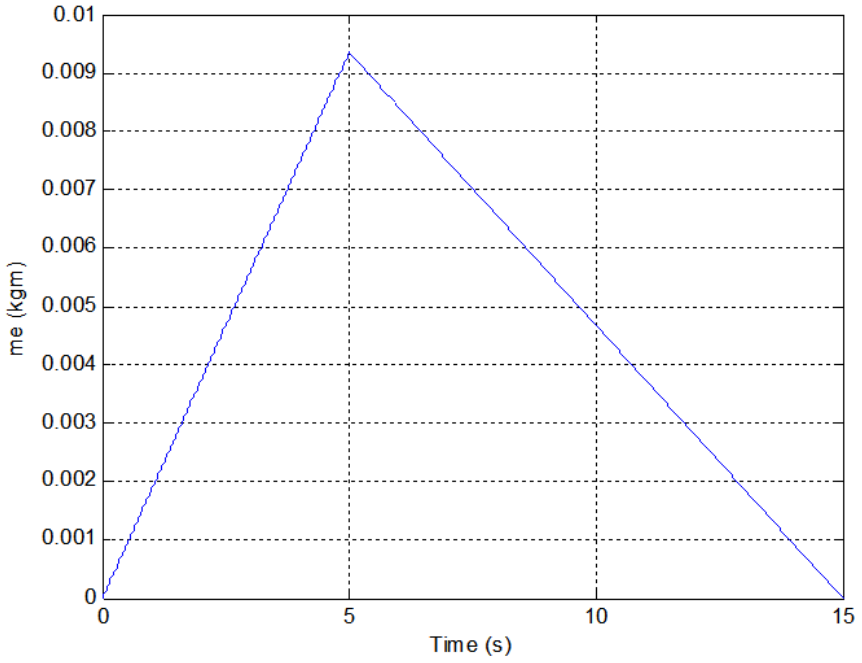

Figure 4.10: Profile of varying rotor unbalance to initiate and remove unbalance force at the non-driven end

The maximum value that the applied unbalance reaches is 9.4 gm. This unbalance variation was applied to the rotor at a rotating speed of 15.9 Hz to observe the contact behaviour. Figure 4.11 shows the displacement response to the varying unbalance. The applied unbalance is shown to initiate rotor/TDB contact. It can be noticed that the rotor makes contact with the TDB in a rub mode. Figure 4.12 shows the corresponding contact forces. The contact force reaches its maximum levels at the start of contact, and as the unbalance decrease is initiated, representing transient behaviour. In this case, a maximum unbalance force of 94 N was reached, causing a maximum contact force of 21.8 N, and a contact duration of 0.4 s.

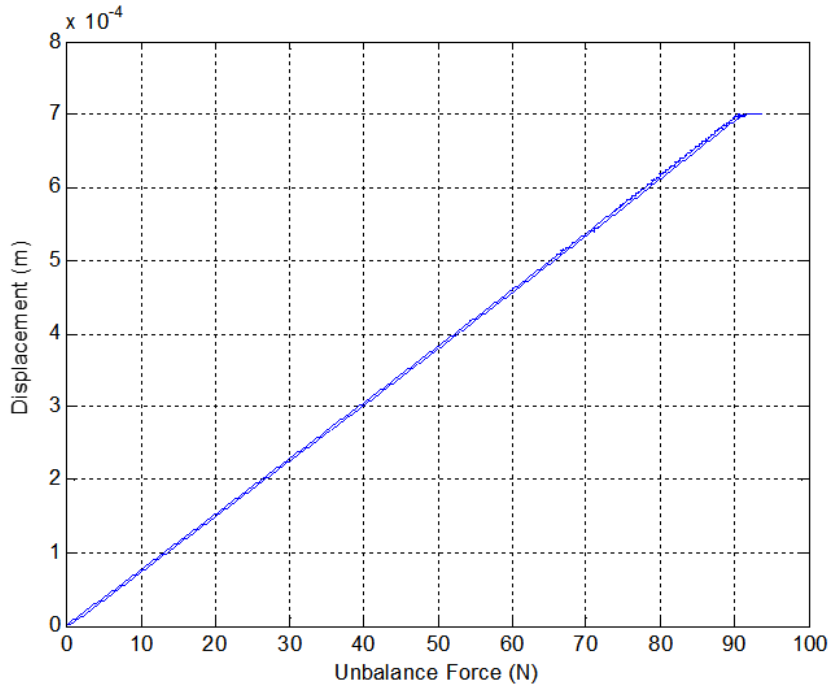

Figure 4.11: Displacement amplitude variation with unbalance force at the non-driven end at a speed of 15.9 Hz

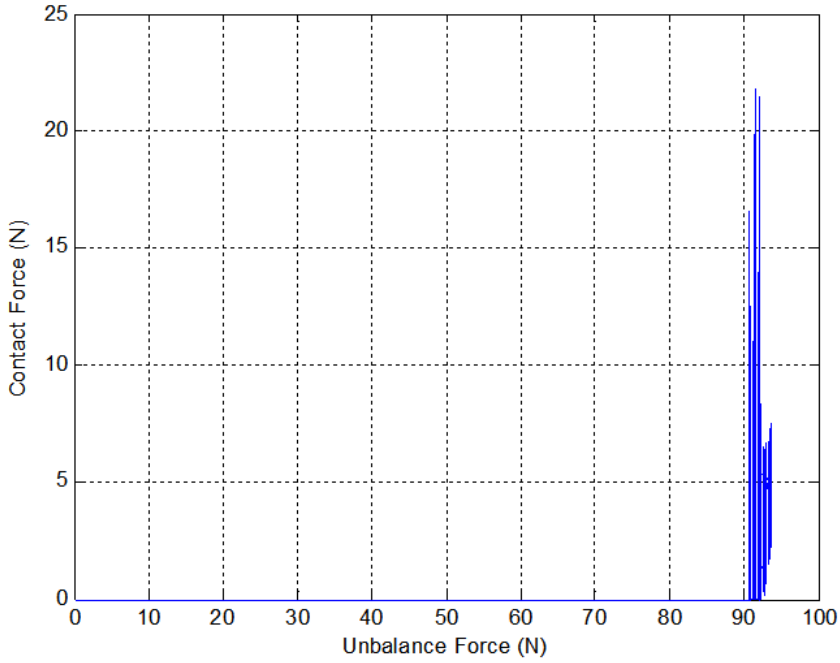

Figure 4.12: Variation of contact forces with unbalance force at the non-driven end at a speed of 15.9 Hz

Similar tests were undertaken at a rotating speed of 23.9 Hz. A maximum value of *me* of 7.4 gm was used. The run-up time to maximum unbalance was 10 s, while the run-down time was varied to observe the change in contact behaviour. Figure 4.13 shows the variation of rotor displacement with the unbalance force, where the run-up time to maximum unbalance was 10 s, and the run-down time was 5 s. Figure 4.14 shows the corresponding contact forces. A maximum contact force of 105.3 N is observed for a maximum applied unbalance force of 166 N. The duration of contact was evaluated to be 0.79 s.

Figure 4.15 shows the rotor displacements in rotating frame coordinates. It is noticed that the rotor enters into a bounce mode during contact, in addition to undergoing rubbing motion. The time duration of the removal of unbalance was decreased in the next test to observe the change in rotor vibration behaviour.

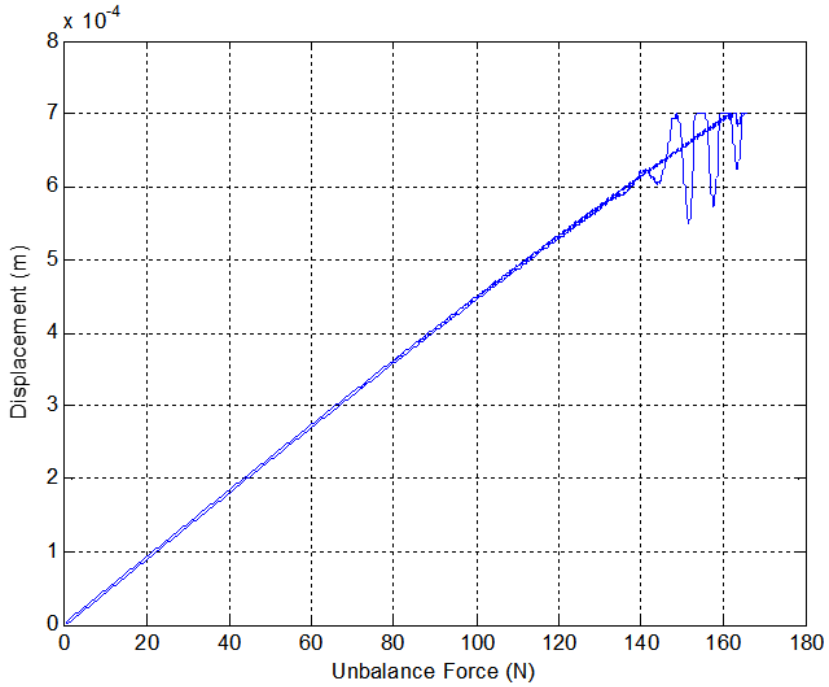

Figure 4.13: Displacement amplitude variation with unbalance force at the non-driven end at a speed of 23.9 Hz with a 5 s unbalance run-down time

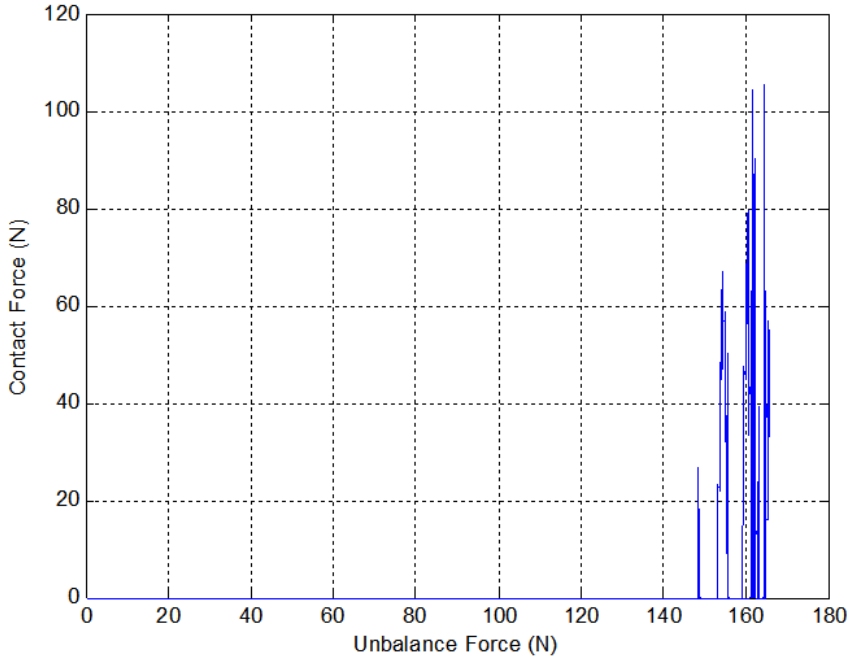

Figure 4.14: Variation of contact force with unbalance force at the non-driven end at a speed of 23.9 Hz with a 5 s unbalance run-down time

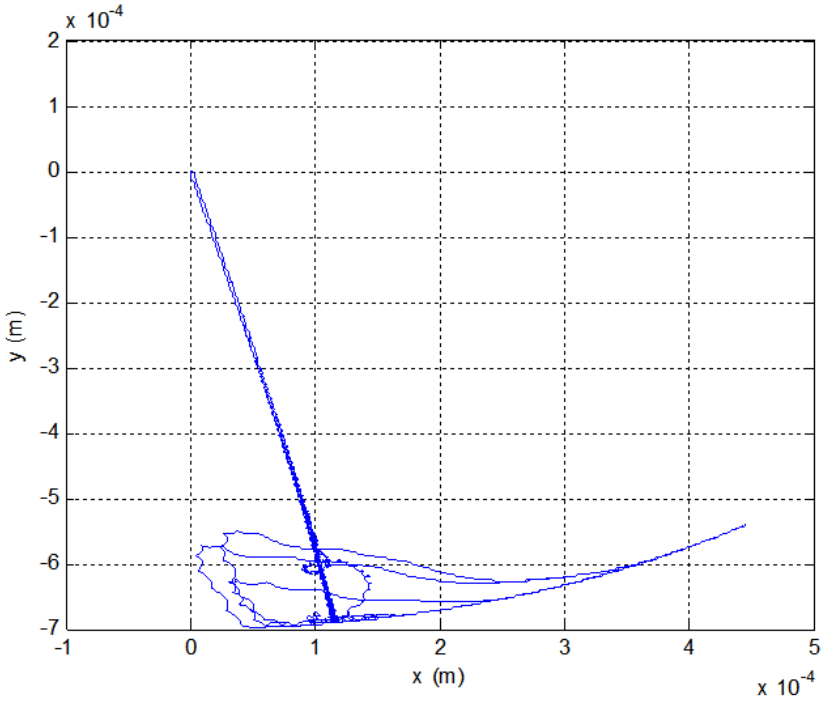

Figure 4.15: Rotor displacements in rotating frame coordinates at the non-driven end at a frequency of 23.9 Hz with a 5 s unbalance run-down time

The second test at the speed of 23.9 Hz was performed with a shorter unbalance run-down time of 0.1 s. Figure 4.16 shows the variation of contact forces with unbalance forces in this case. A maximum contact force of 104.2 N is observed, with a maximum unbalance force of 166 N. The contact duration in this case is shorter than the previous case due to the shorter unbalance run-down time. It is observed that the contact forces increase rapidly with unbalance causing rotor/TDB contact, however, the forces decrease more gradually as unbalance is removed. The corresponding displacements are shown in Figure 4.17, where the rotor's motion leading to contact and recovery from contact is shown.

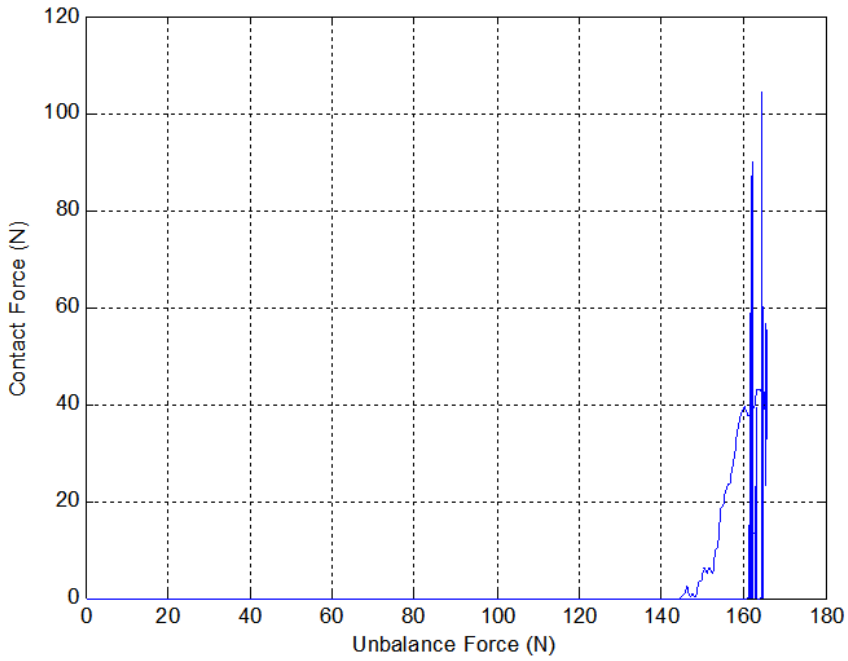

Figure 4.16: Variation of contact force with unbalance force at the non-driven end at a speed of 23.9 Hz with a 0.1 s unbalance run-down time

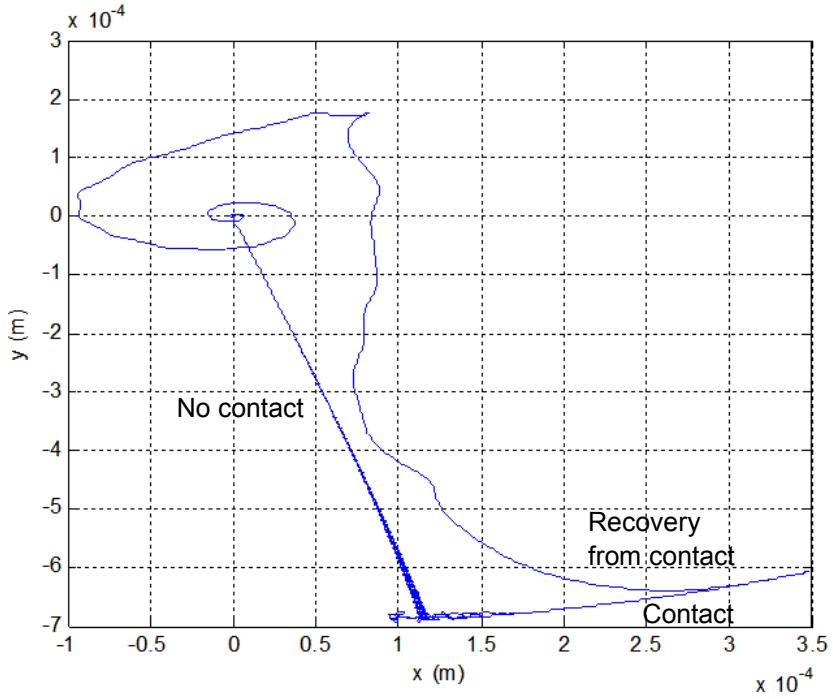

Figure 4.17: Rotor displacements in rotating frame coordinates at the non-driven end at a speed of 23.9 Hz with a 0.1 s unbalance run-down time

A higher rotating speed of 31.8 Hz was employed in another test. A maximum unbalance of 4.6 gm was used, with a run-up time of 5 s, and a run-down time of 10 s. Figure 4.18 shows the displacement amplitude variation with the unbalance forces. A hysteresis phenomenon is observed, where the rotor remains in rotor/TDB contact even after the unbalance forces start decreasing. The contact duration was evaluated to be 7.5 s.

Figure 4.19 shows the corresponding contact forces. The contact forces decrease very gradually in this test as the unbalance is removed. The contact force eventually reduces to zero when the unbalance force reaches a value of 50 N from a maximum unbalance force of 185 N. A maximum contact force of 630 N is observed at an unbalance force of 185 N. Figure 4.20 illustrates the rotor motion as it goes through the unbalance variation, where a rubbing motion is evident.

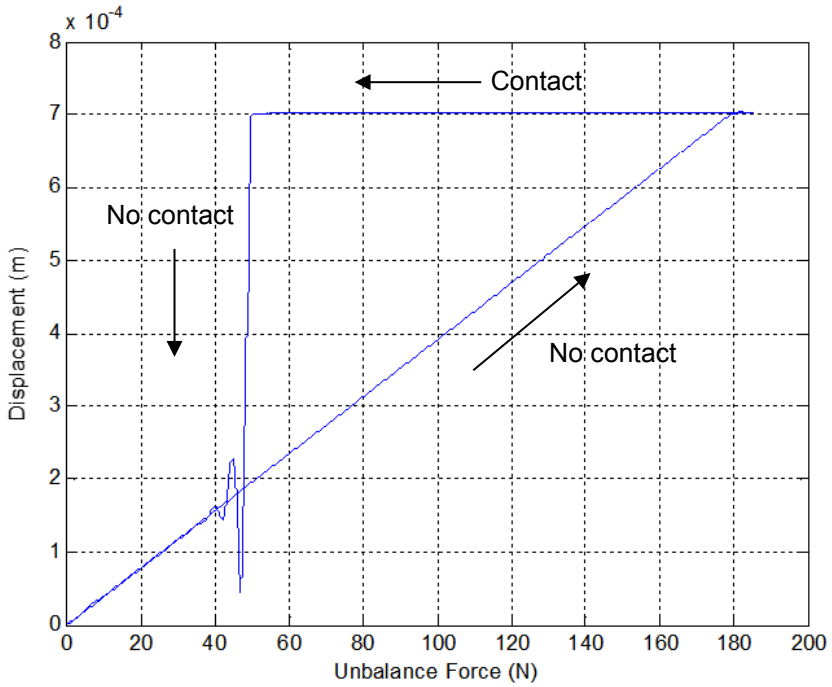

Figure 4.18: Displacement amplitude variation with unbalance force at the non-driven end at a speed of 31.8 Hz

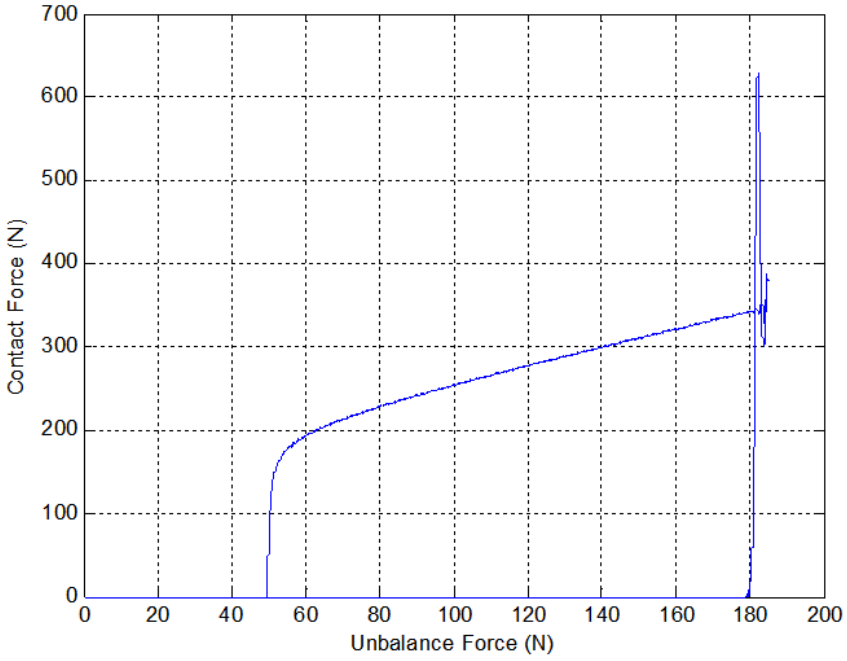

Figure 4.19: Variation of contact force with unbalance force at the non-driven end at a speed of 31.8 Hz

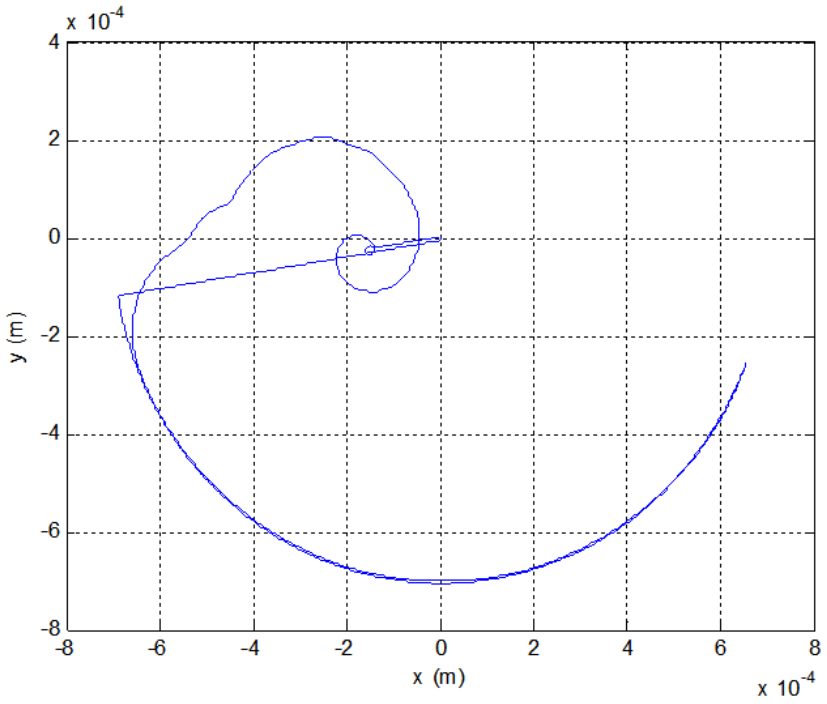

Figure 4.20: Rotor displacements in rotating frame coordinates at the non-driven end at a speed of 31.8 Hz

It can be concluded from the unbalance run-up and run-down tests that the rotor can be induced into rotor/TDB contact with different contact modes and durations. The contact behaviour and duration is dependent on the rotor unbalance level and duration, in addition to the rotor speed. The rotor returned to a non-contact operating position when the unbalance forces were removed. Control strategies taking into account rotor/TDB contact dynamics in such cases are needed to minimise or eliminate contact force levels and durations, whenever changes in unbalance occur in the system.

4.4 Closure

A number of simulation tests were performed on an unbalanced rotor leading to rotor/TDB contact. A speed range covering three of the rotor's critical frequencies was employed. Possible types of transient and steady-state contact modes were identified for the AMB system. Non-persistent and persistent trapped contact modes were demonstrated, which were dependent on the unbalance forces and durations, in addition to the rotor speeds. Similar unbalance cases can be used to test control strategies aimed at minimising or eliminating rotor/TDB contact, particularly persistent contact motion.

Chapter 5

ROTOR/TOUCHDOWN BEARING CONTACT FORCE MEASUREMENT SYSTEM

5.1 Overview

The description of a force measurement system designed and constructed for the research undertaken is presented in this chapter. The system aims to enable experimental assessment of forces related to rotor/TDB contact, based on appropriate transducers. The design considerations of using the system on the rotor/AMB experimental facility are addressed, and the features of the system are presented. Additionally, the calibration method employed in assessing forces arising due to rotor/TDB contact is discussed, and calibration results are demonstrated.

5.2 Design Considerations

Experimental assessment of rotor/TDB contact induced forces forms part of the research undertaken for this thesis. This includes the design and implementation of a force measurement system. Design methodology was required to incorporate force measurement transducers into a TDB or its housing, in order to be mounted on the rotor/AMB system experimental facility. The system would be required to provide experimental data over a range of contact conditions.

Many types of transducers exist that can provide force related data. Different transducers can be used in different configurations and setups, and would require different types of instrumentation. To achieve rotor/TDB contact induced force assessment, the choice of a transducer type and measurement system design was based on a number of considerations, primarily:

- Covering the operating force range. The measurement system should have the capability of covering the contact force range related to the various contact cases considered. Since AMB control forces would be used for rotor vibration attenuation in this research, the force range was dictated by the maximum force capacity of the AMBs. The saturation force limit of the AMBs is 2000 N.

- Measurement of different contact force components. This involves the ability to identify forces acting on the system, to infer their directions, enabling calculation of the corresponding contact forces. Measurement of different force components should also allow derivation of corresponding phase data.

- Ability to incorporate multiple transducers. Since rotor/TDB contact can occur at any point or angle, multiple loading points on the TDB exist. Placing multiple transducers at different positions within the system would reduce uncertainty and minimise any measurement problems related to any off-axis forces.

- Capability of dynamic measurements. The system is required to be capable of measuring dynamic force related data, given the dynamic loading conditions of contact events. Thus, detection of change with an adequate frequency response is essential. The frequency range achieved in measurements would be dependent on the type of transducer and also its instrumentation. The rotational frequency range of the rotor/AMB test rig is up to a 100 Hz, which should also be considered with rotor/TDB contact.

- Appropriate size and installation. The system incorporating the TDB and the measurement transducers should have an appropriate size, and the design must

allow installation within the space available to mount the device at the non-driven end of the experimental rig.

- Design simplicity and cost effectiveness. Employing multiple transducers and their instrumentation for force measurement, the system design and cost requirements would be taken into account. The level of design complexity would affect the manufacturing procedure, in addition to the calibration requirements and procedure. The choice of the transducer type and its instrumentation would also affect the data acquisition hardware and software requirements.

After some studies on various possible configurations and sensing devices, a design incorporating strain gauges mounted on elastic elements was chosen for the purpose of this research. The motivation for using a strain gauge based measurement system included a number of factors satisfying the design considerations discussed. As a common type of transducers for force measurement applications, strain gauge systems have the advantage of providing a continuously stable response and enable force estimation with relatively high linearity from elastic strains. They are capable of measuring in static and dynamic loading conditions, and can provide an adequate frequency range for the application considered. Strain gauges are available in a wide range of sizes and configurations, have no moving parts, and offer a relatively simple construction. This provides the flexibility of integration into a variety of systems and designs, even when demanding multi-component force measurements. Strain gauges need to be associated with electronics such as Wheatstone bridges and amplifiers to provide appropriate outputs. This type of instrumentation is feasible and offers easy integration with the data acquisition system in place. Thus, employing a strain gauge based system provides a cost effective solution with a simple construction, which would give the required measurement data. In order to measure strain, elastic elements are required in the system. A TDB support structure with elastic elements was designed, which can withstand the loading conditions and cover the required force measurement range. The force measurement system design is described in the next section.

5.3 System Description

This section describes the measurement system made to provide experimental data pertaining to contact forces between the TDB and the rotor. The system, which is shown in Figures 5.1 and 5.2, was designed using 3D design software, commissioned, instrumented, and installed at the non-driven end of the rotor/AMB experimental rig.

The system consists of a steel housing, containing a bronze bush acting as a TDB, and is supported by 3 circular flexible beams acting as the elastic elements of the system. The beams are made from aluminium. Each beam is 40 mm long, with a radius of 5 mm. The beams are equipped with strain gauges, and are mounted on a rigid steel structure. The system is 30 mm deep and thus covers 30 mm of the 2 m rotor length at the free end of the rotor. The inner diameter of the bronze bush is 85.5 mm, providing a large rotor/TDB radial clearance of 17.75 mm. When rotor/TDB contact tests are performed, a steel sleeve and collar are mounted onto the shaft, reducing the radial rotor/TDB clearance to 0.35 mm under controlled rotor levitation by the AMBs. The rotor/TDB clearance can be adjusted if needed by using different rotor sleeves with different diameters.

The method for measuring the contact induced force is to measure the strain levels generated in the system due to the rotor/TDB interaction using the strain gauges. Once a rotor/TDB contact condition occurs and produces the impact force, the force transmitted results in the motion of the steel housing as a rigid body. That motion leads to the elastic deformation of the 3 aluminium beams for the duration of the rotor/TDB contact. The force levels can therefore be derived directly from the stress/strain levels of the aluminium beams.

Since rotor/TDB contact can occur at any point or angle on the TDB, this dictated the use of pairs of strain gauges on the aluminium beams in more than one arrangement, to account for all force components and enable the evaluation of the resultant force. That includes strain gauges arranged to measure tension, compression, and bending strains in the beams.

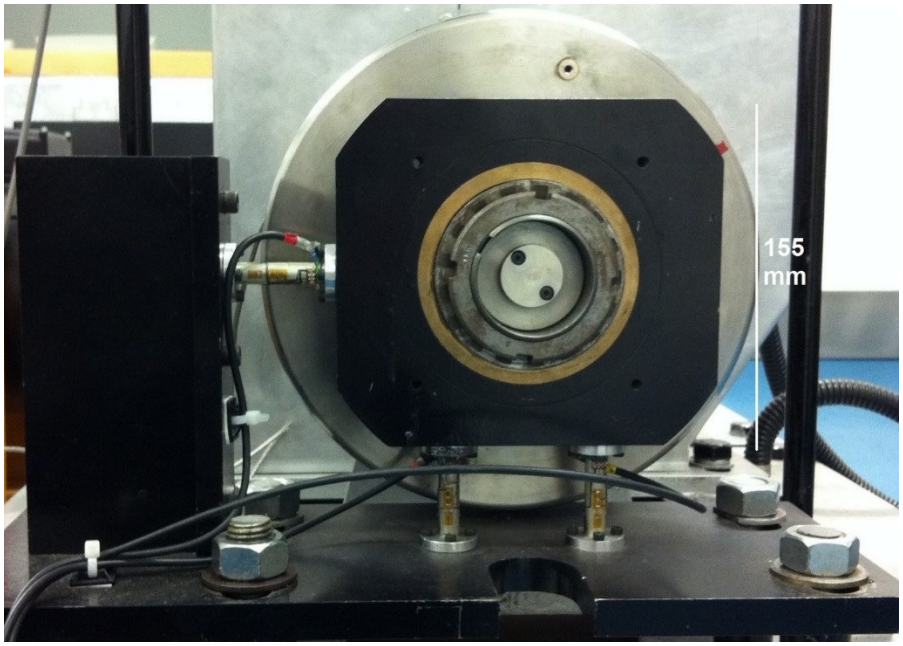

Figure 5.1: A photograph of the contact force measurement system showing the rotor with the sleeve and collar attached

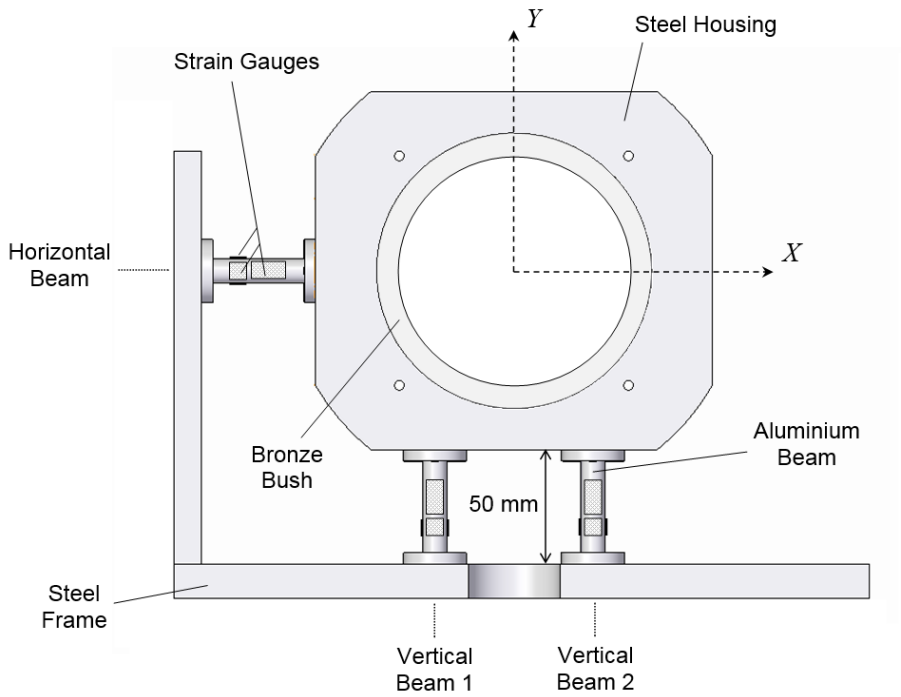

Figure 5.2: Schematic layout of the contact force measurement system

In total, 9 pairs of strain gauges are used on all the flexible beams in the system, with 3 pairs on each of the 3 beams, forming identical layouts. Each pair is attached to a beam on opposing sides at the same location along the length of the beam to detect the required strain. The system design and strain gauge layout enables the system to be sensitive to three orthogonal force components, which are the X and Y radial force components, in addition to any axial force component from the rotor. For the purpose of this research, only radial force components are of interest. This is discussed in more detail in the next section, where system calibration is considered.

Strain gauges convert mechanical strain to a change in electrical resistance. Since changes in strain-initiated resistance can be very small, Wheatstone bridge circuits are employed to convert detected changes in resistance to proportional voltage outputs. Each pair of strain gauges in the system is connected to a Wheatstone bridge circuit, the output of which is the voltage measurement. A combination of full and half Wheatstone bridge circuits are used in the system instrumentation. The Wheatstone bridge circuits employed give a total of 9 strain gauge voltage output signals with a high degree of accuracy. The circuit outputs are directly connected to the dSPACE hardware and software system for data monitoring and acquisition.

Figure 5.3 shows the strain gauges attached to the vertical beams. Figures 5.4 and 5.5 show the strain gauge layouts on the vertical and horizontal beams, respectively, with the types of forces acting on the beams, which the strain gauges would detect during rotor/TDB contact. Strain gauge (A), shown in Figures 5.4 and 5.5, which is the same on all beams, is one of 2 identical gauges attached to each beam on opposite sides. This strain gauge has 2 gauges built-in. The first is a gauge that measures tension and compression beam strains, and the second acts as a Poisson gauge. Both gauges contribute to providing strain measurements related to tension and compression forces acting on a beam. Each pair of opposing strain gauges (A) thus has four active gauges, which are connected to a full Wheatstone bridge. This configuration provides beam tension/compression related measurements, rejecting any bending strains and compensating for the combined effect due to the Poisson's ratio of the beam material.

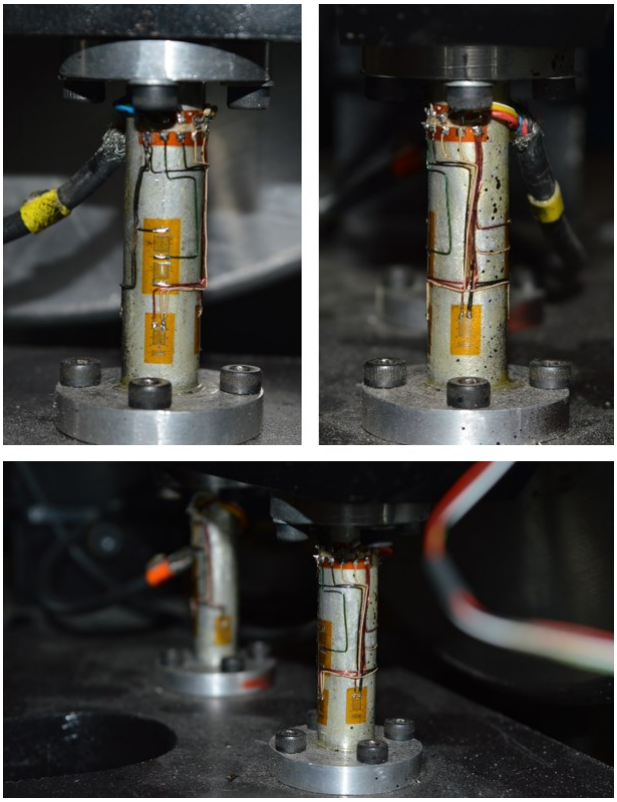

Figure 5.3: Photographs showing the vertical beams of the measurement system. One of the vertical beams is shown with the three strain gauges attached on the front and side of the beam (top), and the two vertical beams are shown (bottom)

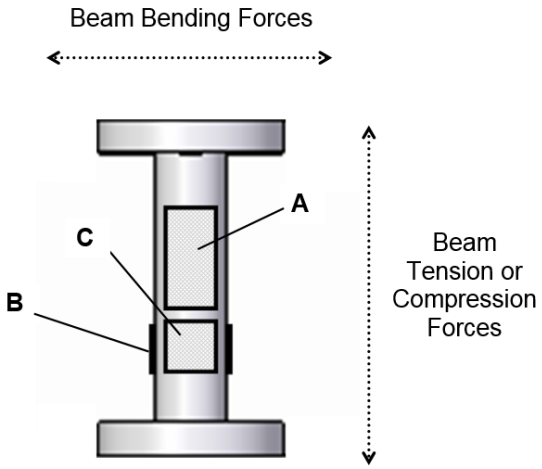

Figure 5.4: Schematic layout showing the positions of the different strain gauges on a vertical beam and the force types acting on the beam (front view)

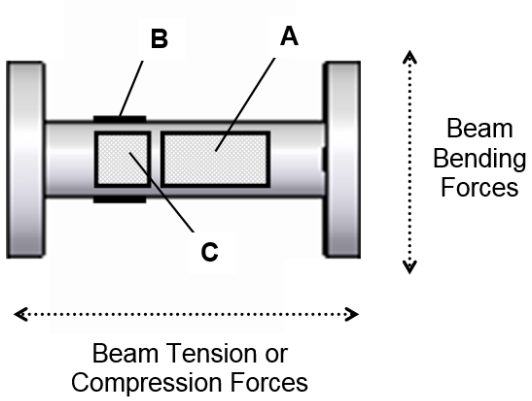

Figure 5.5: Schematic layout showing the positions of the different strain gauges on the horizontal beam and the force types acting on the beam (front view)

Similarly, strain gauge (B) is one of 2 identical gauges attached to each beam on opposite sides, as shown in Figures 5.4 and 5.5. The pair of opposing strain gauges (B) on each beam measure strains related to beam bending forces. Each pair is connected to a half Wheatstone bridge circuit. This configuration provides beam bending related measurements, while rejecting any beam tension/compression strains. The same applies for strain gauge pairs (C) on each beam, which also measure bending strains. However, strain gauge pairs (C) measure beam bending corresponding to components of axial rotor movement (not shown in the figures). If no axial rotor force components exist, these gauges provide no significant outputs. Therefore, a combination of tension/compression and bending strain measurements in different directions contribute in giving data on rotor/TDB interactions.

The frequency range of the strain gauges and the electronics used is up to 108 Hz, which provides an adequate dynamic response. An appropriate size of strain gauges was chosen for the beam dimensions used. Table 5.1 shows the technical data of the strain gauges and their circuits.

Table 5.1: Strain gauge data

Parameter	Value
Type	Foil Electrical Resistance Strain Gauge
Resistance of Each Gauge	350 Ω
Temperature Range for Stable Output	Up to +45 ◦C
Operating Strain Range	Up to 1000 με
Circuit Input Excitation	5 V
Operating Output Voltage	-2 to 1.5 V
Output Frequency Range	Up to 108 Hz

The operating force range of the system is dependent on the strain gauges in addition to the design of the elastic beams. The beam length and radius dimensions were chosen so that they produce enough measureable strain for relatively small applied forces, while also withstanding forces higher than the operating range, and providing enough space to mount the strain gauges. A circular cross-section was chosen for ease of manufacture and to optimise as a uniform shape. However, strain gauge mounting on the beams in this case results in slight bending of the gauges due to the circular cross-section. This provides a small static offset in the measurements that is taken into account in the calibration process. It does not affect the dynamic performance of the system. Table 5.2 shows the data of each of the beams employed.

Table 5.2: Flexible beam data

Parameter	Value
Material	Aluminum Alloy
Length	40×10^{-3} m
Radius	5×10^{-3} m
Cross-section Area	7.85×10^{-5} m^2
Second Moment of Area	4.9×10^{-10} m^4
Young's Modulus	70×10^{9} N/m^2

Assuming small deflections, the bending stiffness of each beam is linear and can be expressed as

$$k_{BB} = \frac{3EI_M}{L^3} \tag{5.1}$$

and the tension/compression stiffness for each beam can be expressed as

$$k_{BA} = \frac{EA_B}{L} \tag{5.2}$$

Using the values provided in Table 5.2, Equations (5.1) and (5.2) give stiffness values of 1.6×10^{6} N/m and 1.37×10^{8} N/m, for bending stiffness and tension/compression stiffness, respectively. Therefore, the dominant stiffness in the system is in relation to tension/compression forces on the beams, rather than bending forces, although both types of forces will affect the force measurements of the system.

5.4 Force Measurement Calibration

5.4.1 Calibration Methodology

The force measurement system can be calibrated in a number of different ways. To enable establishment of a relationship between active control forces, which can be applied by the AMBs, and measured forces related to rotor/TDB contact, force components related to rotor/TDB contact were calibrated against input forces applied by AMB 2. This relationship would provide important force related data that can be used in rotor/TDB interaction control, which is the ultimate aim of this research.

The calibration of the system was undertaken after assembly and installation on the test rig and took into account all the 9 strain gauge outputs provided by the system in all cases. Forces were applied through AMB 2, after the rotor was levitated, to introduce rotor/TDB contact at the measurement system. The rotor contact within the inner surface of the bronze bush TDB caused the force measurement system to respond. The measurements of the resulting voltages of the strain gauges were then related to the AMB 2 forces in the 2 radial components, and then to the phase angles, to achieve the calibration of radial forces measurement in the system. Figure 5.6 shows the applied AMB 2 force, $\mathbf{f}_{MB}$, and the resulting contact force, $\mathbf{f}_c$, at the force measurement system location.

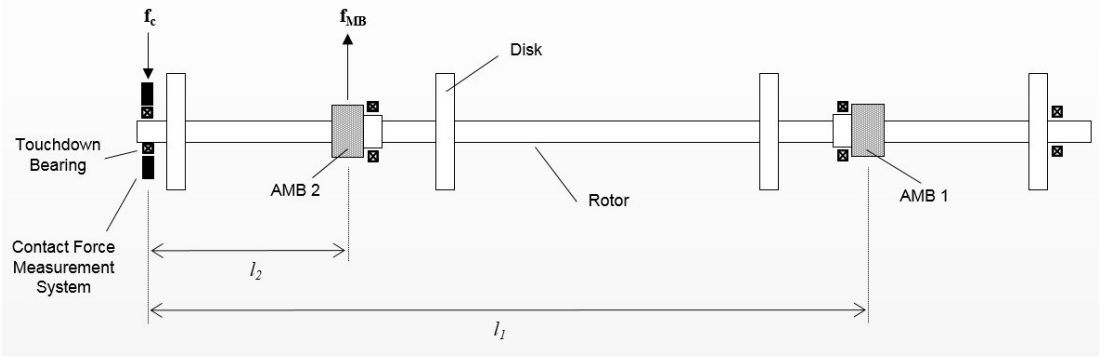

Figure 5.6: Schematic layout of the test rig showing AMB and contact forces

The applied AMB 2 force $\mathbf{f_{MB}}$ is expressed as a 2×1 force vector consisting of X and Y components as

$$\mathbf{f_{MB}}(\omega t)=\begin{bmatrix} F_{MBX}(\omega t) \\ F_{MBY}(\omega t) \end{bmatrix} \tag{5.3}$$

The X and Y force components are expressed as

$$\begin{aligned} F_{MBX}(\omega t) &= F_{MB}\cos(\omega t+\phi_{MB}) \\ F_{MBY}(\omega t) &= F_{MB}\sin(\omega t+\phi_{MB}) \end{aligned} \tag{5.4}$$

where F_{MB} is the force amplitude and ϕ_{MB} is the phase shift angle, for a given AMB 2 force, $\mathbf{f_{MB}}$. The corresponding contact force vector $\mathbf{f_c}$ in X and Y components is

$$\mathbf{f_c}(\omega t)=\begin{bmatrix} F_{cX}(\omega t) \\ F_{cY}(\omega t) \end{bmatrix} \tag{5.5}$$

The contact force at the force measurement system location can be defined in terms of the strain gauge voltages as

$$\mathbf{f_c}(\omega t)=\mathbf{C_c}(\omega)\mathbf{v}(\omega t) \tag{5.6}$$

where $\mathbf{C_c}$ is a calibration matrix, and $\mathbf{v}(\omega t)$ is a 9×1 voltage vector consisting of the 9 strain gauge voltage signals. Under static conditions, the contact force can be related to the applied AMB 2 force by considering moments about the AMB 1 location, where the rotor is centralised by PID control action, as

$$\mathbf{f_c}(0)=\left(\frac{l_1-l_2}{l_1}\right)\mathbf{f_{MB}}(0) \tag{5.7}$$

Substituting Equation (5.7) into Equation (5.6), with $\omega = 0$ representing static conditions, yields the AMB 2 force as

$$\mathbf{f_{MB}}(0) = \mathbf{C_{MB}}(0)\mathbf{v}(0) \tag{5.8}$$

where $\mathbf{C_{MB}}$ is a calibration matrix relating applied AMB 2 forces to strain gauge voltages upon rotor/TDB contact, defined as

$$\mathbf{C_{MB}}(0) = \left(\frac{l_1}{l_1 - l_2} \right) \mathbf{C_c}(0) \tag{5.9}$$

Equation (5.8) represents the calibration relationship between an applied AMB 2 force and the force measurement system voltages. A series of tests were performed to demonstrate this relationship.

5.4.2 Static Tests

Employing static AMB 2 forces, experimental tests were performed to calibrate the force measurement system. Both the applied whirl frequency of the AMB and the rotational (motor) frequency were set to zero. Different force amplitudes and phase angles were applied through AMB 2, which is the closest AMB to the force measurement system. The integral control action was switched off at AMB 2 for the purpose of applying the input forces, while the integral control action at AMB 1 kept the rotor centralised at its normal operating point. Rotor/TDB contact due to static AMB 2 applied forces only occurred at the force measurement system location. Table 5.3 shows the parameters used for the PID controllers.

Table 5.3: PID control parameters for static calibration

PID Control Parameter	AMB 1	AMB 2
$K_i K_P$ (N/μm)	3	3
$K_i K_I$ (N/s/μm)	0.3	0
$K_i K_D$ (Ns/μm)	0.005	0.005

Static tests were done with a series of input AMB 2 radial forces ranging from 100 N to 2000 N, over 8 input phase angles covering 360 Deg, as follows

$$\hat{\mathbf{F}}_{\mathbf{MB}n}(0) = \left[\hat{\mathbf{f}}_{\mathbf{MB}n,\hat{\phi}_{MB1}}(0), \ldots, \hat{\mathbf{f}}_{\mathbf{MB}n,\hat{\phi}_{MB8}}(0) \right] \tag{5.10}$$

where $n = 1,\ldots,12$, representing 12 different input force amplitudes ($\hat{F}_{MB}$) and $\hat{\mathbf{F}}_{\mathbf{MB}n}$ is a 2×8 input force matrix of the X and Y components of a given force amplitude, $\hat{F}_{MBn}$, with 8 different input phase angles, $\hat{\phi}_{MB1},\ldots,\hat{\phi}_{MB8}$. The corresponding voltage signals obtained for each applied $\hat{\mathbf{F}}_{\mathbf{MB}n}$ are

$$\hat{\mathbf{V}}_n(0) = \left[\hat{\mathbf{v}}_{n,\hat{\phi}_{MB1}}(0), \ldots, \hat{\mathbf{v}}_{n,\hat{\phi}_{MB8}}(0) \right] \tag{5.11}$$

where $\hat{\mathbf{V}}_n$ is a 9×8 measured voltages matrix. Combining the 12 matrices resulting from Equation (5.10), which correspond to the 12 force amplitudes, yields the overall applied forces matrix, which consists of all input force amplitudes and angles, as follows

$$\hat{\mathbf{F}}_{\mathbf{MB}}(0) = \left[\hat{\mathbf{F}}_{\mathbf{MB1}}(0), \ldots, \hat{\mathbf{F}}_{\mathbf{MB12}}(0) \right] \tag{5.12}$$

where $\hat{\mathbf{F}}_{\mathbf{MB}}$ is a 2×96 matrix consisting of the *X* and *Y* components of the 96 applied AMB 2 forces. The corresponding measured voltage signals obtained at the force measurement system as a result of applying these force inputs are

$$\hat{\mathbf{V}}(0)=\left[\hat{\mathbf{V}}_{\mathbf{1}}(0),\ldots,\hat{\mathbf{V}}_{\mathbf{12}}(0)\right] \tag{5.13}$$

where $\hat{\mathbf{V}}$ is a 9×96 matrix consisting of all measured voltages. In principle, the relationship between the AMB 2 input forces and the measured voltages can be expressed as

$$\hat{\mathbf{F}}_{\mathbf{MB}}(0)=\mathbf{C}_{\mathbf{MB}}(0)\hat{\mathbf{V}}(0) \tag{5.14}$$

Thus, a calibration matrix, representing the force-voltage relationship, was estimated as follows

$$\mathbf{C}^{\mathbf{e}}_{\mathbf{MB}}(0)=\hat{\mathbf{F}}_{\mathbf{MB}}(0)\hat{\mathbf{V}}^{T}(0)\left(\hat{\mathbf{V}}(0)\hat{\mathbf{V}}^{T}(0)\right)^{-1} \tag{5.15}$$

where $\mathbf{C}^{\mathbf{e}}_{\mathbf{MB}}$ is the estimated calibration matrix of dimensions 2×9. This calibration matrix is estimated in the presence of measurement error and nonlinearity. The estimated AMB 2 force for a given AMB 2 force input can hence be evaluated as

$$\mathbf{f}^{\mathbf{e}}_{\mathbf{MB}}(0)=\mathbf{C}^{\mathbf{e}}_{\mathbf{MB}}(0)\hat{\mathbf{v}}(0) \tag{5.16}$$

This equation uses the estimated calibration matrix, in addition to the vector of measured voltages that are obtained as a result of rotor/TDB contact at the force measurement system, and is of the same form as Equation (5.8).

The estimated AMB 2 forces corresponding to the 12 different input force amplitudes, which were applied in the static tests performed, were evaluated using $\mathbf{C}^{\mathbf{e}}_{\mathbf{MB}}$ as

$$\mathbf{F}^{e}_{\mathbf{MB}n}(0) = \mathbf{C}^{e}_{\mathbf{MB}}(0)\hat{\mathbf{V}}_{n}(0) \tag{5.17}$$

where $\mathbf{F}^{e}_{\mathbf{MB}n}$ is a 2×8 matrix of the X and Y components of estimated AMB 2 forces as a result of applying an input $\hat{\mathbf{F}}_{\mathbf{MB}n}$. Estimated AMB 2 forces were evaluated for the whole range of input forces.

Figure 5.7 shows the relationship between the input AMB 2 forces and the corresponding estimated AMB 2 forces, in their X and Y components, for an input angle of 45 Deg.

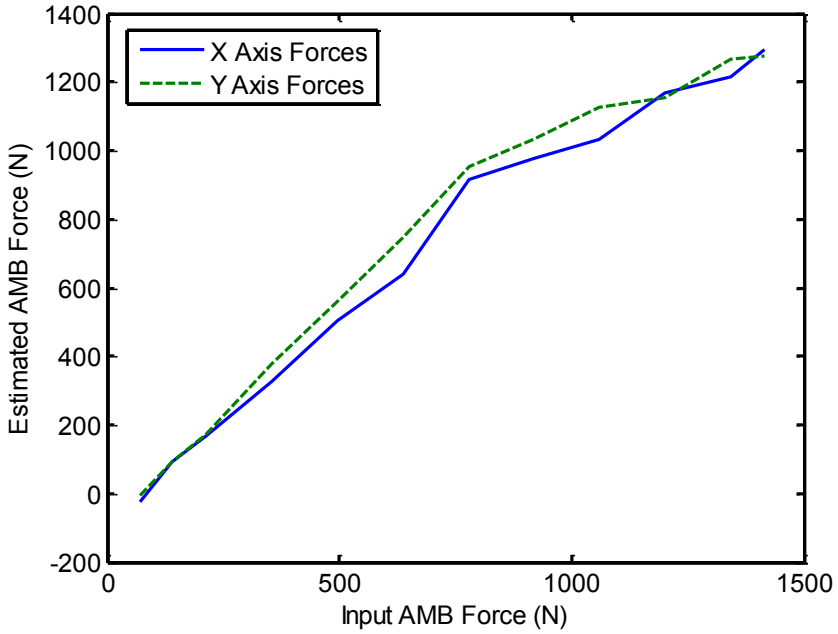

Figure 5.7: Static forces of AMB 2 with an input phase angle of 45 Deg

This figure demonstrates system calibration, at a specific phase angle, through the relationship between input forces and estimated forces. Estimated AMB 2 forces are evaluated using the voltage measurements obtained as a result of applying the AMB 2

input forces, which are of sufficient magnitude to excite the strain gauge system due to rotor/TDB contact.

Figures 5.8 and 5.9 show the relationships between the input forces and the estimated forces, in the X and Y components, respectively, for the whole range of forces and angles used in the static tests. Figure 5.10 shows the relationship between the input and estimated phase angles. Estimated phase angles were obtained using the corresponding X and Y components of the estimated forces as follows

$$\phi_{MB}^{e} = \tan^{-1}\left(F_{MBY}^{e} / F_{MBX}^{e}\right) \tag{5.18}$$

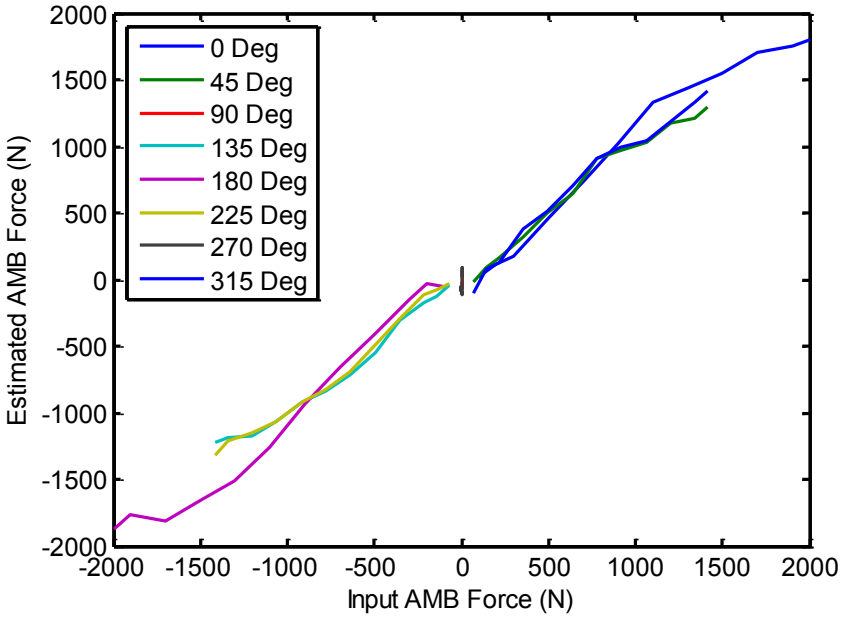

Figure 5.8: X-axis static AMB 2 forces at phase angles: 0, 45, 90, 135, 180, 225, 270, and 315 Deg

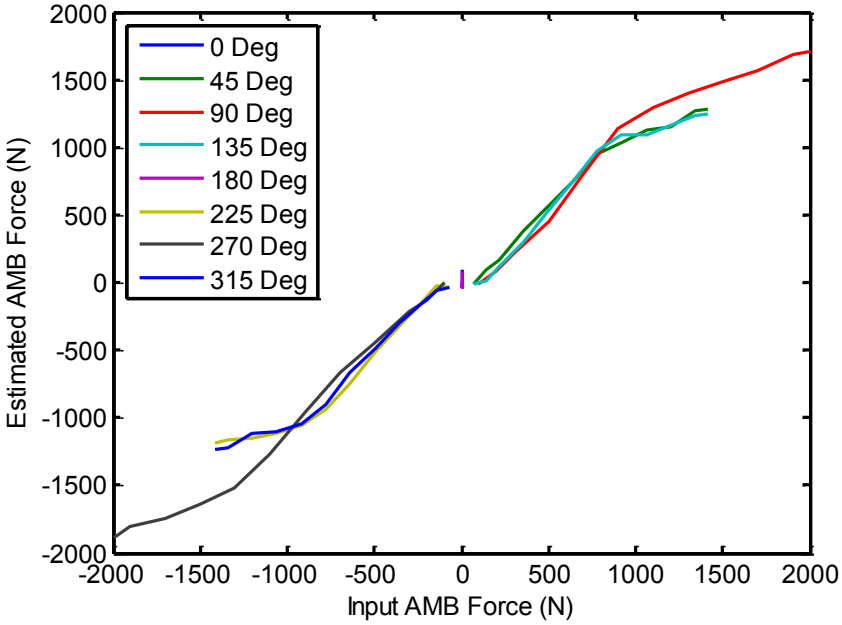

Figure 5.9: Y-axis static AMB 2 forces at phase angles: 0, 45, 90, 135, 180, 225, 270, and 315 Deg

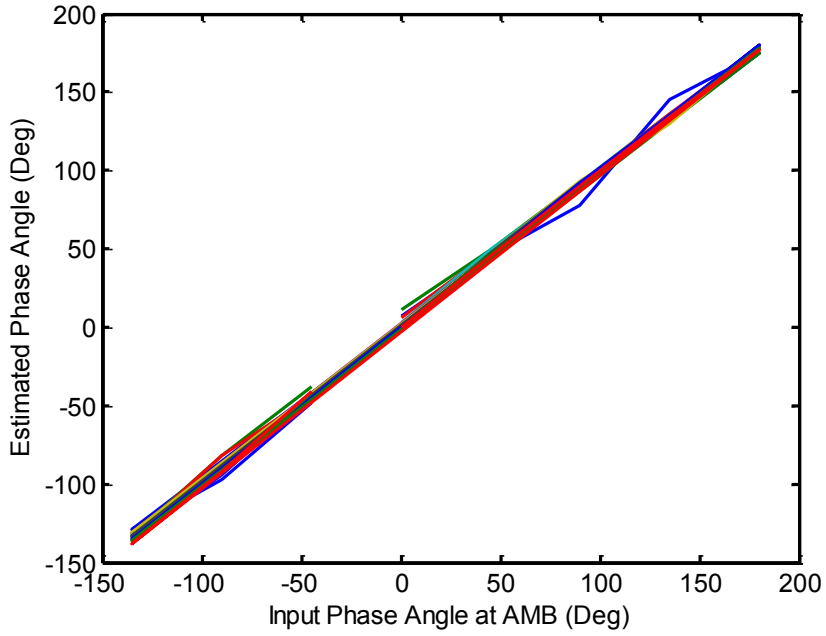

Figure 5.10: Phase angle variation with static AMB 2 forces over an input force amplitude range of 300-2000 N

The rotor/TDB contact force at the force measurement system was not used directly in performing the static calibration. However, it may be inferred according to

$$\mathbf{f}_{\mathbf{c}}^{\mathbf{e}}(0) = \left(\frac{l_1 - l_2}{l_1} \right) \mathbf{f}_{\mathbf{MB}}^{\mathbf{e}}(0) \tag{5.19}$$

The results obtained from the tests performed demonstrate the relationship between static input AMB 2 forces and estimated AMB 2 forces due to rotor/TDB contact measurements, based on the evaluated static calibration matrix, $\mathbf{C}_{\mathbf{MB}}^{\mathbf{e}}$. Statically derived force measurements can be applicable for dynamic force measurements. Thus, dynamic force cases can be investigated over different frequencies, employing the calibration matrix, to demonstrate the dynamic performance of the system. This is explored in the next chapter.

5.5 Closure

A rotor/TDB contact force measurement system was described in this chapter. The design considerations were addressed, and the different components of the system were discussed. Strain gauge measurements of the TDB support structure of the system were related to force components through a calibration procedure. The calibration involved relating rotor/TDB contact conditions to applied AMB control forces. Through system calibration, results were demonstrated providing static AMB control force estimation. The calibration data obtained can be used in assessing dynamic forces.

Chapter 6

CONTACT DYNAMIC TESTS AND ANALYSIS

6.1 Overview

In order to demonstrate the dynamics of contact in the AMB/rotor system, a series of experimental tests are presented in this chapter. Based on the static calibration of the force measurement system, dynamic force estimation tests are undertaken. Force and phase data are derived from the measurement system outputs and analysed. A range of rotor frequencies and AMB applied force levels are employed to demonstrate the contact cases. Additionally, comparison between simulation and experimental results is considered, including force and displacement data.

6.2 Dynamic Force Assessment

Rotor/touchdown bearing dynamic interactions need to be investigated to identify the contact behaviour in the system. Therefore, estimated AMB forces due to rotor/TDB contact are investigated over different rotor frequencies.

Rotor interaction with a TDB occurs when the rotor's amplitude in the radial direction reaches the specified rotor/TDB clearance value. The TDB then restrains the radial displacement of the rotor during contact, and is subject to the forces exerted by the rotor.

Rotor/TDB contact introduces forces normal to the touchdown bearing surface at the contact point. Kinetic (dynamic) friction is formulated, based on dry contact between the metal surfaces of the rotor and the TDB. Friction forces at the contact point are related to the normal forces via a Coulomb coefficient of friction.

Figure 6.1 shows the estimated AMB force and phase evaluated at the force measurement system upon rotor/TDB dynamic interaction. The force F_{MBR}^{e} represents the estimated AMB force amplitude, which is a resultant of the X and Y force components. The forces shown represent forces acting on the touchdown bearing.

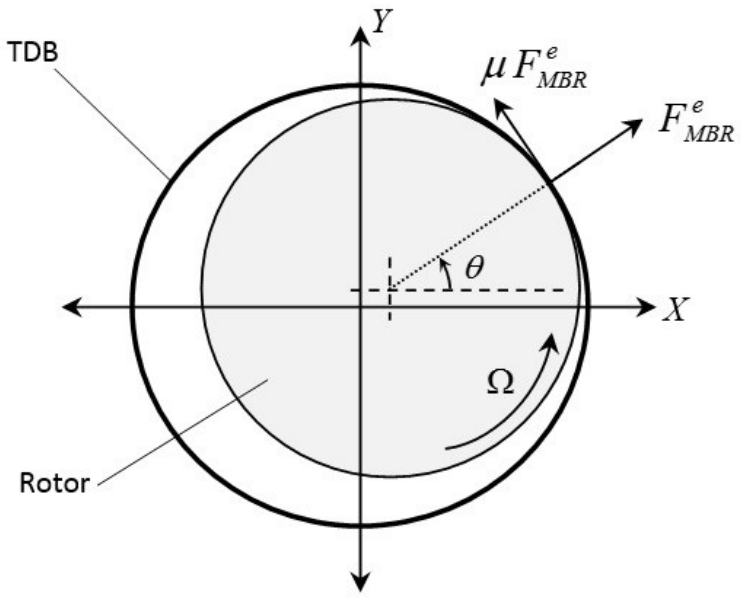

Figure 6.1: Diagram showing estimated AMB forces and phase due to rotor/TDB contact

The angle of contact θ can be expressed as

$$\theta = \Omega t + \phi_R \tag{6.1}$$

where ϕ_R represents a phase shift. The estimated AMB force due to contact, $\mathbf{f}^{\mathbf{e}}_{\mathbf{MB}}$, consists of X and Y components that can be expressed as

$$\begin{aligned} F^{e}_{MBX}(\Omega t) &= A_X \cos(\Omega t + \phi_X) \\ F^{e}_{MBY}(\Omega t) &= A_Y \sin(\Omega t + \phi_Y) \end{aligned} \tag{6.2}$$

where $\Omega = \omega$ if no rotation by the motor is applied. Since the voltage signals generated by the strain gauge system were related to the X and Y components of the estimated AMB force through a calibration matrix, $\mathbf{C}^{\mathbf{e}}_{\mathbf{MB}}$, the calibration matrix is employed to identify the forces in dynamic conditions as follows

$$\mathbf{f}^{\mathbf{e}}_{\mathbf{MB}}(\omega t) = \mathbf{C}^{\mathbf{e}}_{\mathbf{MB}}(0)\,\hat{\mathbf{v}}(\omega t) \tag{6.3}$$

Thus, Equation (6.2) describes the dynamic output of the force measurement system, which can be evaluated according to Equation (6.3).

To test the dynamic rotor/TDB contact response to dynamic AMB input forces, the following input is applied

$$\begin{aligned} \hat{F}_{MBX}(\omega t) &= \hat{F}_{MB} \cos(\omega t) \\ \hat{F}_{MBY}(\omega t) &= \hat{F}_{MB} \sin(\omega t) \end{aligned} \tag{6.4}$$

where ω is the whirl frequency generated by the AMB. In this case, no rotor rotation by the motor takes place and the dynamic forces are generated by the AMB whirl induced rotor motion. Therefore, the force measurement system output becomes

$$\begin{aligned} F^{e}_{MBX}(\omega t) &= A_X \cos(\omega t + \phi_X) \\ F^{e}_{MBY}(\omega t) &= A_Y \sin(\omega t + \phi_Y) \end{aligned} \tag{6.5}$$

Figure 6.2 shows the X and Y components of the estimated AMB 2 forces, where an AMB force input of 700 N amplitude was applied at whirl frequencies of 1 Hz and 5 Hz. Dynamic input forces were applied through AMB 2, while full PID control action at both AMBs was functional.

Figure 6.2 demonstrates the ability to evaluate the estimated AMB forces at the measurement system location due to dynamic AMB force inputs. While the *X* and *Y* force components are measured, it is useful to arrive at the amplitude of the estimated dynamic AMB force. This can be achieved by calculating the resultant force amplitude

$$F_{MBR}^{e} = \left\| \mathbf{f}_{\mathbf{MB}}^{\mathbf{e}}(\omega t) \right\|_2 = \sqrt{F_{MBX}^{e}(\omega t)^2 + F_{MBY}^{e}(\omega t)^2} \tag{6.6}$$

In what follows, this is termed the estimated AMB force.

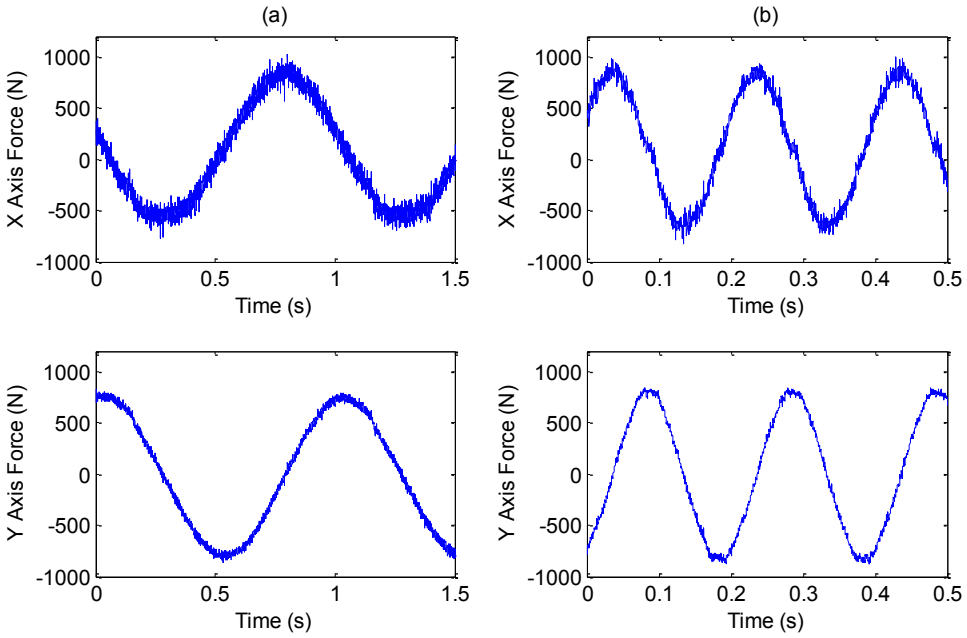

Figure 6.2: Estimated AMB 2 force *X* and *Y* components for an AMB 2 applied force input of 700 N at (a) 1 Hz (b) 5 Hz

Since the estimated AMB force due to rotor/TDB contact measurements is directly relative to the AMB applied force, the dynamic relationship between an input AMB force and the corresponding estimated AMB force can be represented by

$$F_{MBR}^{e} = \alpha(\omega)\hat{F}_{MB} \tag{6.7}$$

where α is the force amplitude ratio, which is frequency dependent. To investigate this, the relationship between the input and estimated AMB forces for whirl frequencies of 1 and 10 Hz were examined as shown in Figure 6.3. An AMB 2 input force range of 100 to 1200 N was applied. A linear force relationship in each case can be derived. The linearized slope of each graph represents the force amplitude ratio α for that specific frequency. At 1 Hz the slope was found to be 1.33, while at 10 Hz the slope was found to be 1.27. Frequency dependence is noticed, and thus the behaviour may change at other frequencies. Further tests are needed to establish the system's dynamic behaviour with changing frequencies.

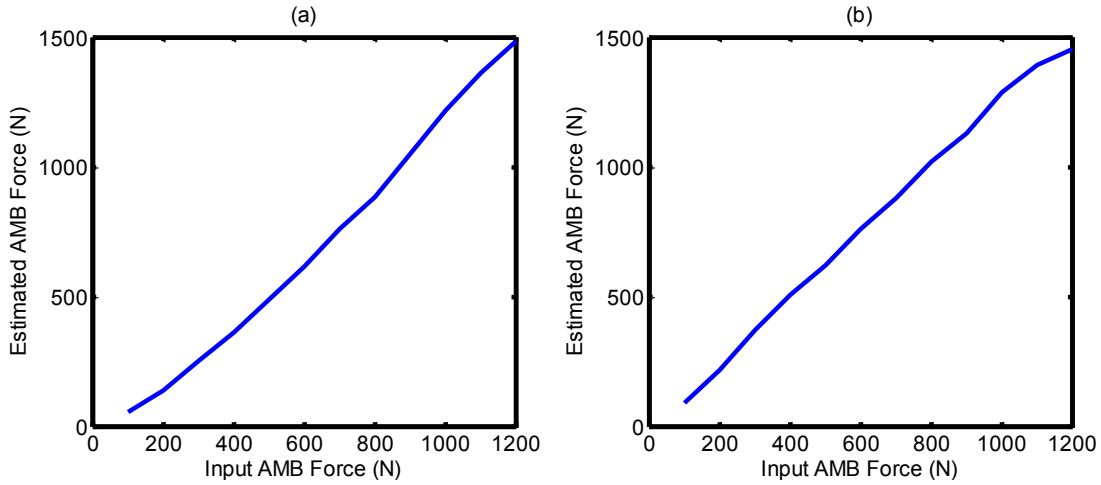

Figure 6.3: Relationship between estimated AMB 2 forces and input AMB 2 forces covering an input force range of 100-1200 N at (a) 1 Hz and (b) 10 Hz

Further tests were performed to identify the relationship between input AMB forces and estimated AMB forces for a frequency range of 1 to 30 Hz, covering different rotor critical frequencies. Figure 6.4 shows the dynamic behaviour of the system at an AMB 2 applied input force of 700 N over the whirl frequency range of 1-30 Hz. Each estimated AMB force value in the figure represents the mean value of the resultant force, F^{e}_{MBR}, for the corresponding input force level $\hat{F}_{MB}$ of 700 N at each whirl frequency.

In the tests performed, the inertia of the force measurement system's steel housing and mounting frame incorporating the TDB was not taken into account, since the purpose of these tests is to relate the estimated AMB forces, due to rotor/TDB contact, to input AMB forces in the system, in order to arrive at an AMB based control system capable of contact force reduction or elimination. However, the inertia and dynamics of the force measurement system should be taken into account if real contact force data are to be evaluated, or if different bearing types are to be employed in the system.

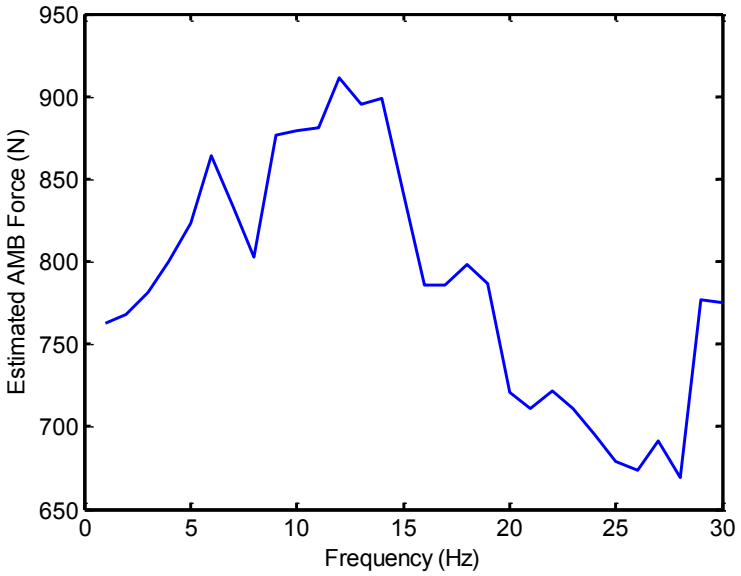

Figure 6.4: Estimated AMB 2 forces over a frequency range of 1-30 Hz for an applied AMB 2 force input of 700 N

Frequency dependence is noticed in Figure 6.4. The mean value of the resultant estimated AMB force at 1 Hz is evaluated to be 763 N giving an amplitude ratio of 1.09, while at 12 Hz the amplitude ratio α reaches a maximum of 1.3 at an estimated AMB force of 911 N. The estimated AMB force is seen to vary over the frequency range considered, which demonstrates the frequency dependent nature of the amplitude ratio α. The frequency dependence is due to the rotor system dynamics, as rotor/TDB contact, which leads to AMB force estimation, occurs at the force

measurement system location, while input forces are applied by AMB 2 of the test rig, which is 0.45 m inboard the force measurement system.

Peaks at 12, 18 and 29 Hz are seen in the plot, corresponding to the natural frequencies of the levitated rotor. These represent the modes with rigid body dominance, in addition to the mode of significant rotor flexure.

A peak at a frequency of approximately 7 Hz is also seen in the plot. This frequency is significantly lower than the first natural frequency of the flexible rotor. Since the experimental rotor/AMB/TDB system is mounted on a base plate with isolators between it and the ground, the base itself can be subject to motion. Rotor/TDB contact motion can induce base motion, which would affect the frequency response of the system. Wang (2016) studied and analysed the base motion, involving isolators, of the same AMB experimental test facility employed in this research. It was demonstrated that a frequency of approximately 7 Hz is a natural frequency that corresponds to base motion of the AMB test rig. This explains the first peak that can be seen in Figure 6.4.

Figure 6.5 shows the dynamic behaviour of the system at an applied input AMB 2 force of 1100 N over a whirl frequency range of 1-30 Hz. The frequency dependence on the flexible rotor is noticed. The amplitude ratio at 1 Hz is evaluated as 1.24 at an estimated AMB 2 force of 1362 N. It reaches a maximum at 12 Hz of 1.31 at an estimated AMB 2 force of 1443 N, and varies at different whirl frequencies.

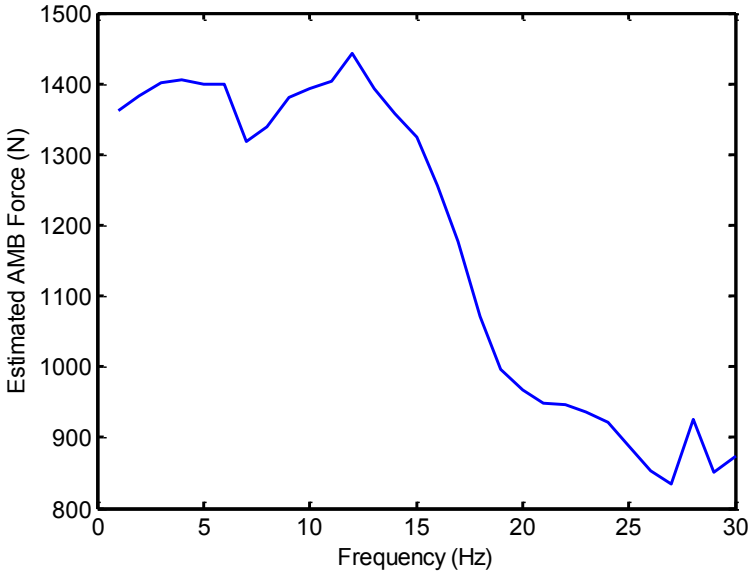

Figure 6.5: Estimated AMB 2 forces over a frequency range of 1-30 Hz for an applied AMB2 force input of 1100 N

The results demonstrate that the estimated AMB force at different force levels and frequencies can be assessed by the force measurement system due to rotor/TDB contact. It is also noticed from the results that the force amplitude ratio, α, as determined by the force measurement system output, is frequency dependent and force dependent, as it varies with both AMB applied force levels and whirl frequency values.

The displacements at the four sensor locations of the rotor/AMB system were measured at different frequencies and force levels during the dynamic tests performed. Figure 6.6 shows the rotor orbits at all sensor locations for a 700 N AMB 2 force input, and Figure 6.7 shows the orbits for a 1100 N AMB 2 force input. The rotor/TDB radial clearance at the driven end is 900 μm, while it is 750 μm at both AMB locations, and 350 μm at the non-driven end where the force measurement system is.

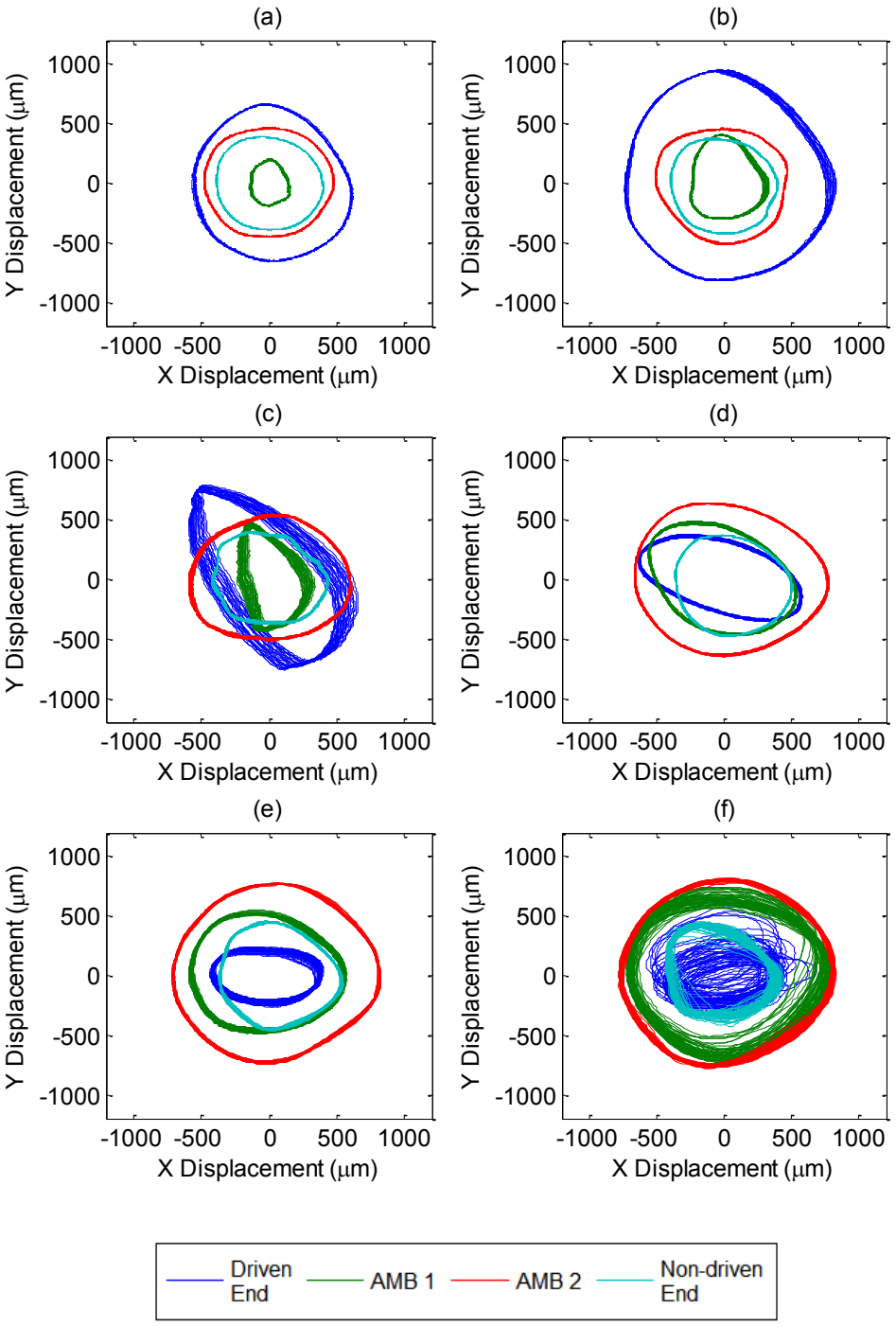

Figure 6.6: Rotor orbits at the four sensor plane locations for an applied AMB 2 input force of 700 N at (a) 5 Hz (b) 10 Hz (c) 15 Hz (d) 20 Hz (e) 25 Hz (f) 30 Hz

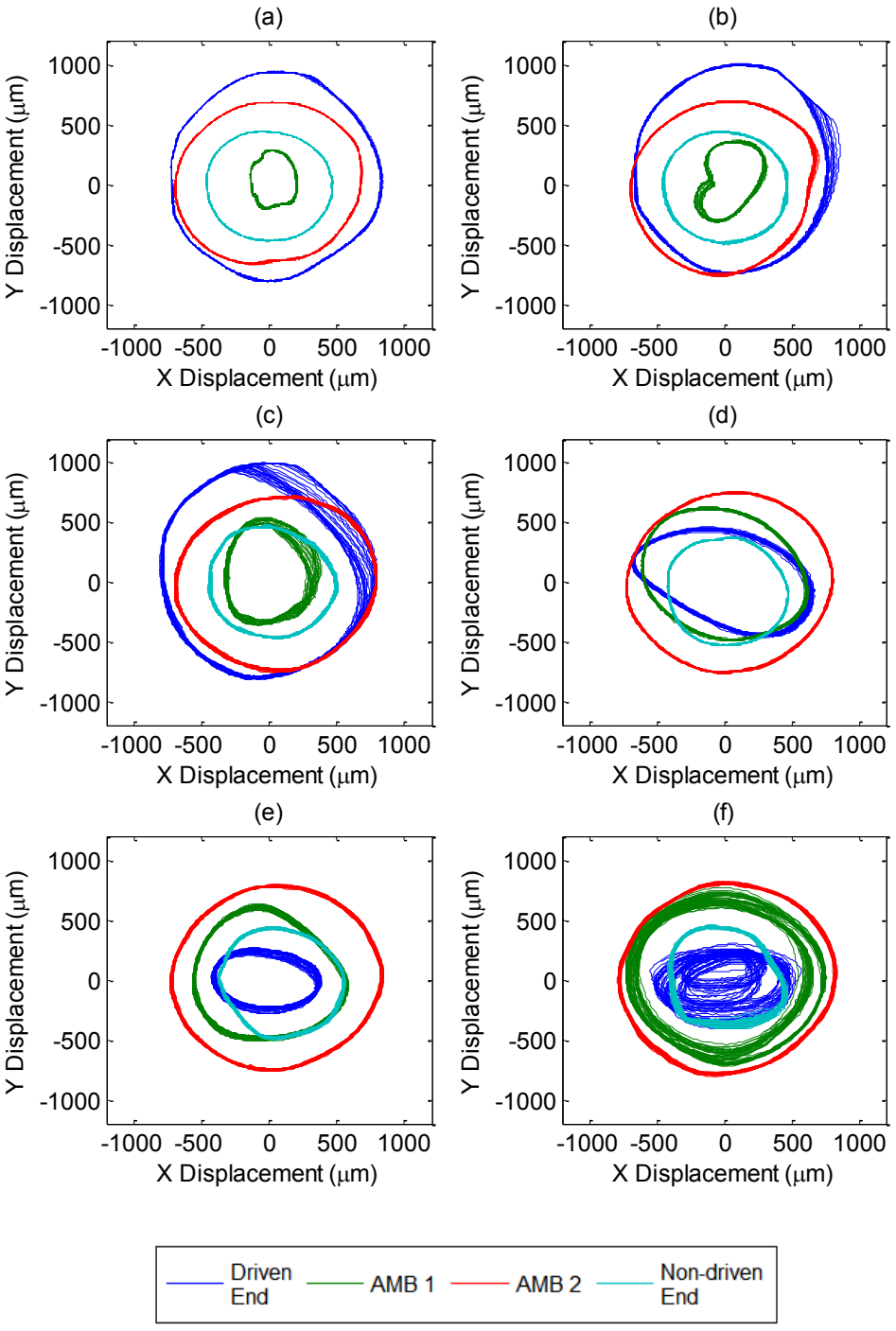

Figure 6.7: Rotor orbits at the four sensor plane locations for an applied AMB 2 input force of 1100 N at (a) 5 Hz (b) 10 Hz (c) 15 Hz (d) 20 Hz (e) 25 Hz (f) 30 Hz

By analysing the radial displacement values of the two figures, it is noted that the rotor is in contact with the TDB at the force measurement system location in all cases at the frequencies and input forces considered. No rotor/TDB contact occurs at AMB 1 due to the PID integral control action, nor does rotor/TDB contact occur at the driven end TDB due to the larger rotor/TDB clearance value. The rotor can be seen to pass through the conical and cylindrical modes by observing the orbits, specifically the driven end orbits, as the whirl frequency is increased.

At 700 N, the rotor is noticed to make contact at the TDB of AMB 2, where the input force is applied, at frequencies of 25 and 30 Hz. This is due to the combination of a 700 N force amplitude and high whirl frequencies. Similarly, at 1100 N, the rotor makes contact at the TDB of AMB 2 at frequencies of 20, 25 and 30 Hz. It is noticed that with high force amplitudes and whirl frequencies, the rotor makes contact with the AMB TDB where these forces and frequencies are applied, in addition to contact at the force measurement system TDB.

6.3 Phase Assessment

In order to understand rotor/TDB dynamics and enable control design capable of dealing with rotor/TDB interaction, the phase values related to the estimated AMB forces, arising from rotor/TDB contact, need to be determined. Both AMB input forces and force measurement system output forces have been applied and measured in their X and Y components, as described by Equations (6.4) and (6.5). The phase difference between input AMB control forces and estimated AMB forces can hence be explored. Figure 6.8 shows both estimated AMB force components and applied input force components at a 700 N AMB 2 applied force amplitude at whirl frequencies of 1 Hz and 5 Hz.

The force components are plotted against time. The input force amplitude and the resultant estimated AMB forces are also shown for both frequencies. The mean value of the resultant estimated AMB force at 1 Hz was calculated to be 763 N, and it was

calculated to be 823 N at 5 Hz. This gives amplitude ratios of 1.09 and 1.18, respectively.

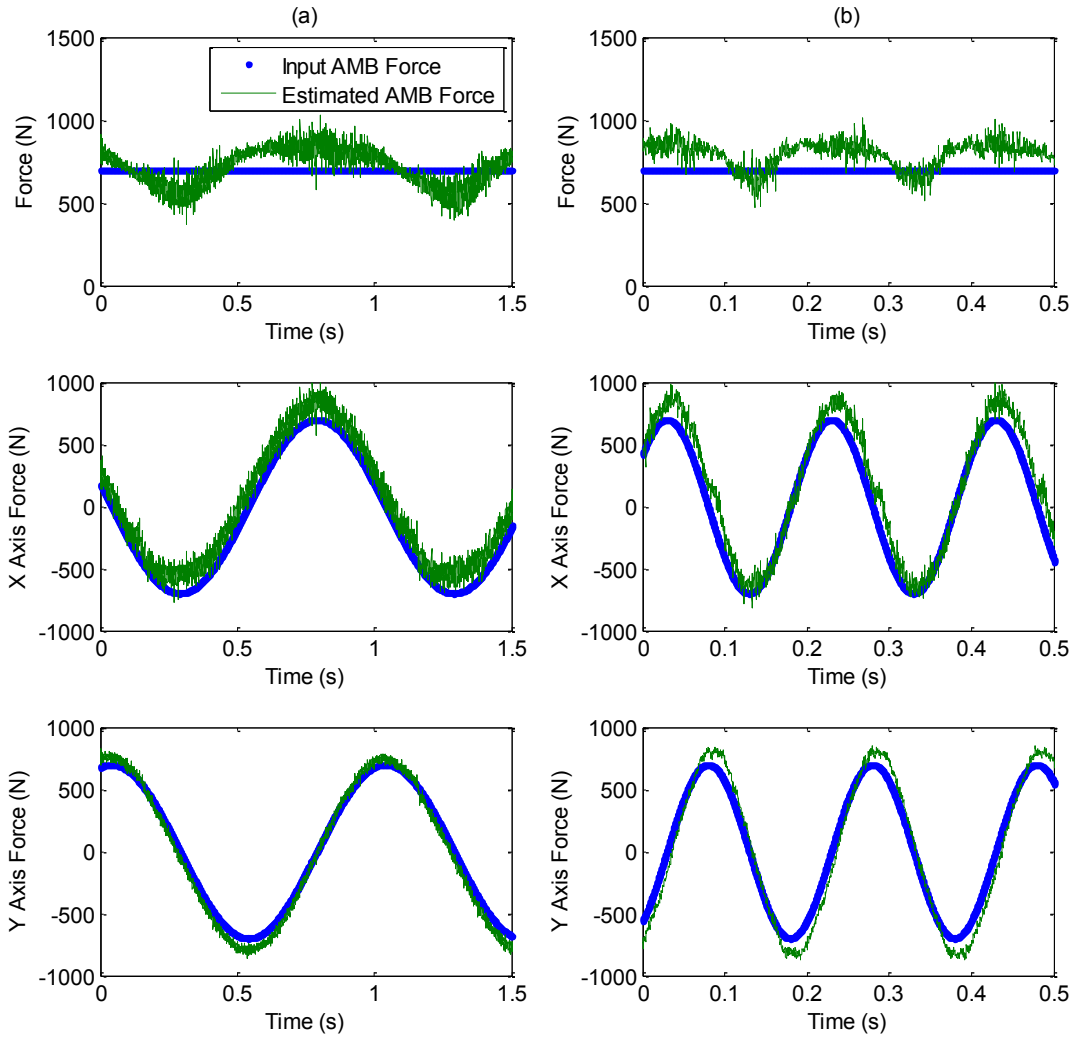

Figure 6.8: Estimated AMB 2 forces for an applied force input of 700 N at (a) 1 Hz (b) 5 Hz

A difference in the time domain between applied forces and estimated AMB forces in the *X* and *Y* directions for each frequency can be identified. This relative timing between the two force signals at a given frequency yields experimental phase data. The sinusoidal component of each of the input and evaluated measured signals at the

specific frequency considered can be used to extract the phase. Since each cycle in the time domain represents 360 degrees, the phase difference can be evaluated and expressed in Deg. In Figure 6.8, for the 1 Hz frequency, examining the *X* and *Y* force signals, a phase difference of 1 Deg exists between applied and estimated AMB forces. At 5 Hz, a phase difference of 11 Deg is evaluated.

While the force amplitude ratio and phase values obtained from the force measurement system output at 1 Hz represent a close resemblance to static conditions, due to the very low whirl frequency applied, a significant difference is noticed at 5 Hz, with a bigger phase difference and an increased force amplitude ratio. These measured force and phase data characterise the dynamic behaviour of the system upon the occurrence of rotor/TDB contact.

At the whirl frequencies considered, the phase difference between input and estimated AMB forces may be due to the contact friction between the rotor and the touchdown bearing because of rubbing contact motion. The friction force in this case increases with the increase of the contact force experienced by the bearing. However, if phase difference specifically due to friction is of interest, it requires to be assessed and established, for any whirl frequency, by tests using different bearing/bushing types with different materials, lubricants, or a different surface finish. The phase difference between input and output measured forces is also influenced by the rotor/AMB system dynamic behaviour, in addition to the force measurement system dynamics. This includes the influence of system critical frequencies and the different rotor mode shapes.

The relative phase at different frequencies was explored. Figure 6.9 shows the phase difference between the estimated AMB forces and applied forces, in both the *X* and *Y* force components, for a whirl frequency range of 1-30 Hz. An applied AMB 2 force amplitude of 700 N was used.

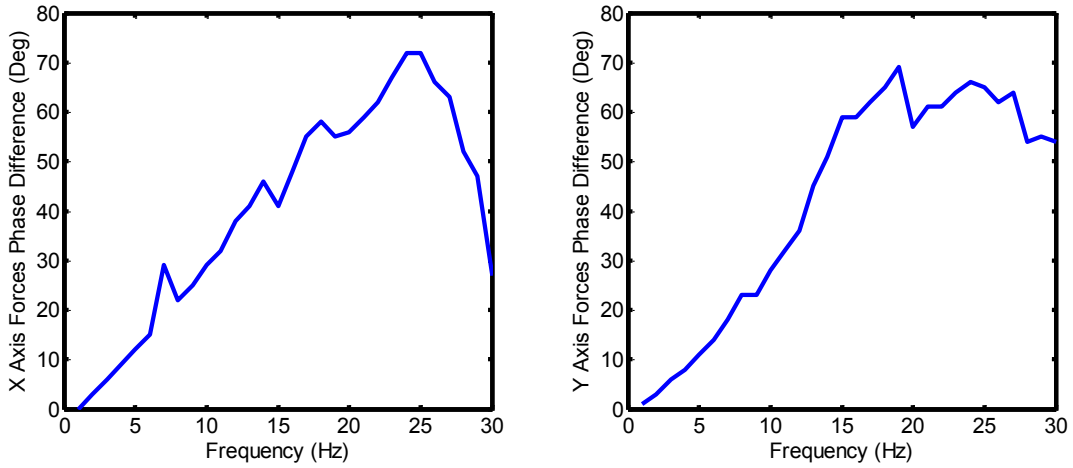

Figure 6.9: Phase difference between input and estimated AMB 2 forces in X and Y components over a frequency range of 1-30 Hz for an applied force input of 700 N

The dynamic phase behaviour is identified over the frequency range. It is noticed that there is a small difference between the phase values in the X and Y force components at some frequencies. It is useful to arrive at an overall resultant phase shift value for the input force level considered. In this case, the different X and Y components of the estimated AMB force amplitude and phase shift of Equation (6.5) can be considered. This takes into account the possible different output force amplitudes and phases in the X and Y directions that can be obtained from the measurements. Therefore, the resultant overall phase difference can be calculated as follows, considering the rotor forward whirl motion

$$\phi_R = \tan^{-1}\left(\frac{A_X \sin\phi_X + A_Y \sin\phi_Y}{A_X \cos\phi_X + A_Y \cos\phi_Y}\right) \tag{6.8}$$

Hence, a more accurate approach to the resultant estimated AMB force calculation, in comparison to Equation (6.6), can be expressed as

$$F^e_{MBR} = \frac{1}{2}\sqrt{{A_X}^2 + {A_Y}^2 + 2A_X A_Y \cos(\phi_X - \phi_Y)} \tag{6.9}$$

which yields

$$F_{MBR}^{e} = \frac{A_X + A_Y}{2} \tag{6.10}$$

if $\phi_X = \phi_Y$. Using Equation (6.8), the results of Figure 6.9 are combined with the resultant phase and shown in Figure 6.10.

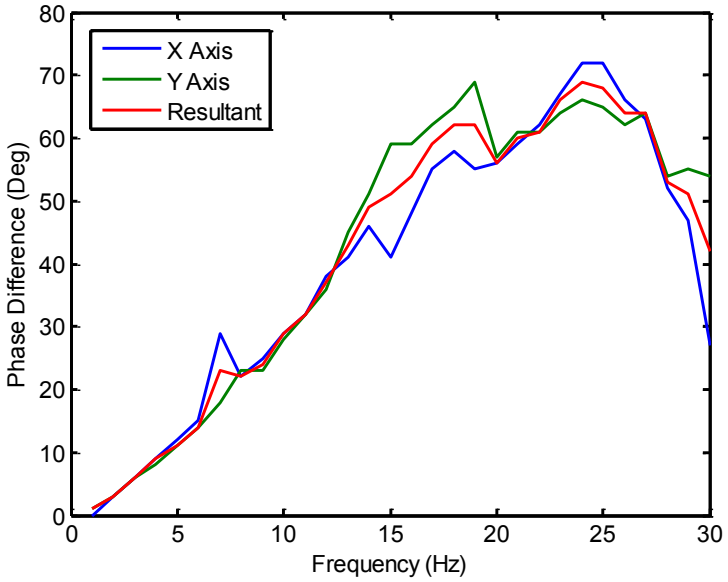

Figure 6.10: Phase difference between applied and estimated AMB 2 forces over a frequency range of 1-30 Hz for an applied AMB force input of 700 N

Phase difference dynamic changes were also evaluated for different force levels and are shown in Figure 6.11. AMB 2 input force amplitudes of 600 N, 800 N, 1000 N, and 1200 N are considered.

The frequency dependent nature of the phase difference can be highlighted, identifying the system dynamic behaviour. Since phase data are demonstrated using the force measurement system outputs, appropriately phased AMB input control forces can be

derived and identified, to form valuable data for potential contact control. This includes contact at different force levels and rotor frequencies.

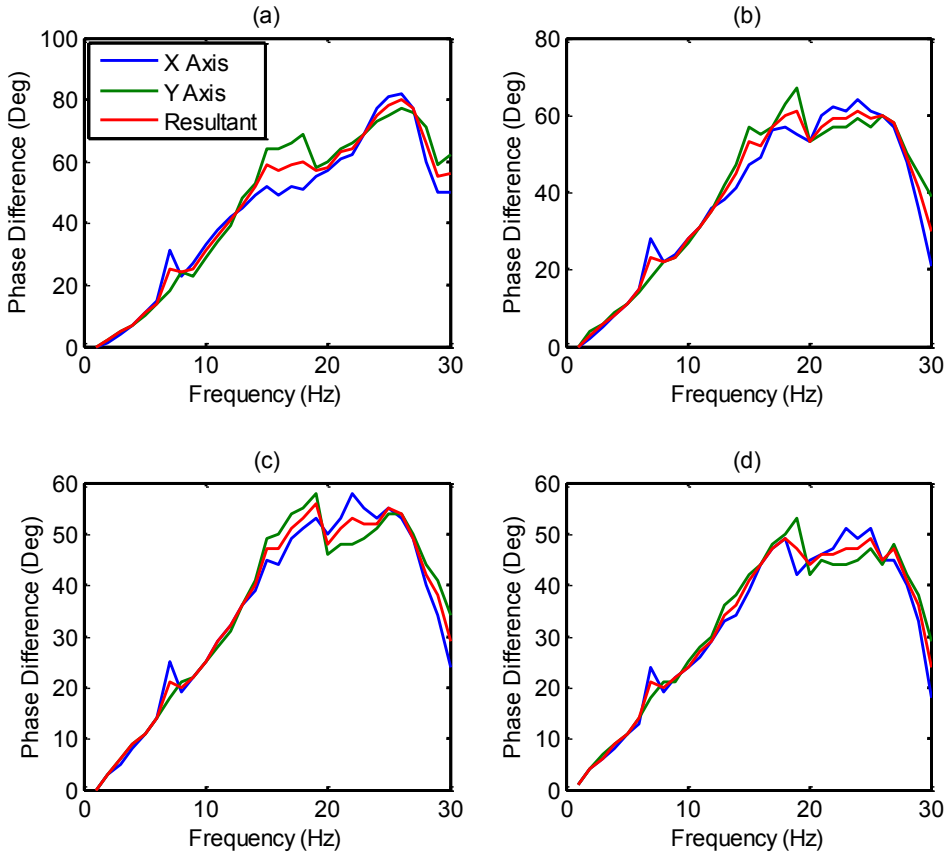

Figure 6.11: Phase difference between applied and estimated AMB 2 forces over a frequency range of 1-30 Hz for an applied AMB force input of (a) 600 N (b) 800 N (c) 1000 N (d) 1200 N

The initial tests performed can be extended to cover a variety of force levels and frequencies, yielding more force and phase data in relation to AMB input forces.

6.4 Contact Behaviour at Varying Forces and Frequencies

For a more comprehensive understanding of the rotor/AMB/TDB system, and to provide more data that can potentially be used in contact control and system model validation and understanding, a wide range of AMB 2 input forces were applied to the force measurement system. The results can form a dynamic map of the system behaviour, and be considered as the dynamic calibration of the force measurement system.

An AMB 2 force input range of 100-1200 N was considered, with 100 N increments. This gives 12 input force levels. An input whirl frequency range of 1-30 Hz was also considered, covering rigid body and first flexural critical frequencies. Thus, 360 individual experimental tests were performed to arrive at the full set of data.

Lubrication was used between the rotor and the TDB at the force measurement system location, giving a relatively low coefficient of friction and reducing damage to the system due to the contact motion. The response of the force measurement system was used to arrive at the force amplitude ratio and phase difference for each test. This provides data in relation to different rotor/TDB contact conditions at different frequencies and force levels. Figure 6.12 shows the force amplitude ratio, α, obtained from the estimated AMB force levels, and Figure 6.13 shows the measured phase results.

In addition to the force measurement system data, displacement sensor data were recorded to show the displacement amplitudes at different locations along the 2 m flexible rotor. Figure 6.14 shows the measured radial displacement amplitudes at the non-driven end, close to the force measurement system location. Figure 6.15 shows the displacements close to the AMB 2 location, where the input forces were applied. Figure 6.16 shows the displacements close to the AMB 1 location, which remained under PID control with no extra AMB forces applied. Figure 6.17 shows the displacements at the driven end of the rotor system.

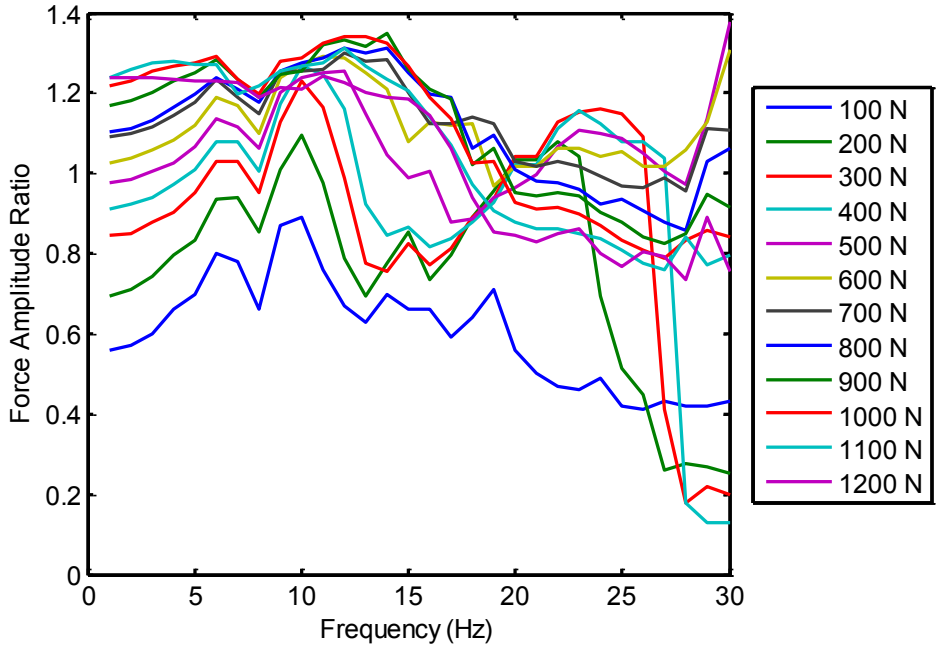

Figure 6.12: Force amplitude ratios between AMB 2 applied forces and estimated AMB 2 forces for a frequency range of 1-30 Hz and input force amplitudes of 100-1200 N

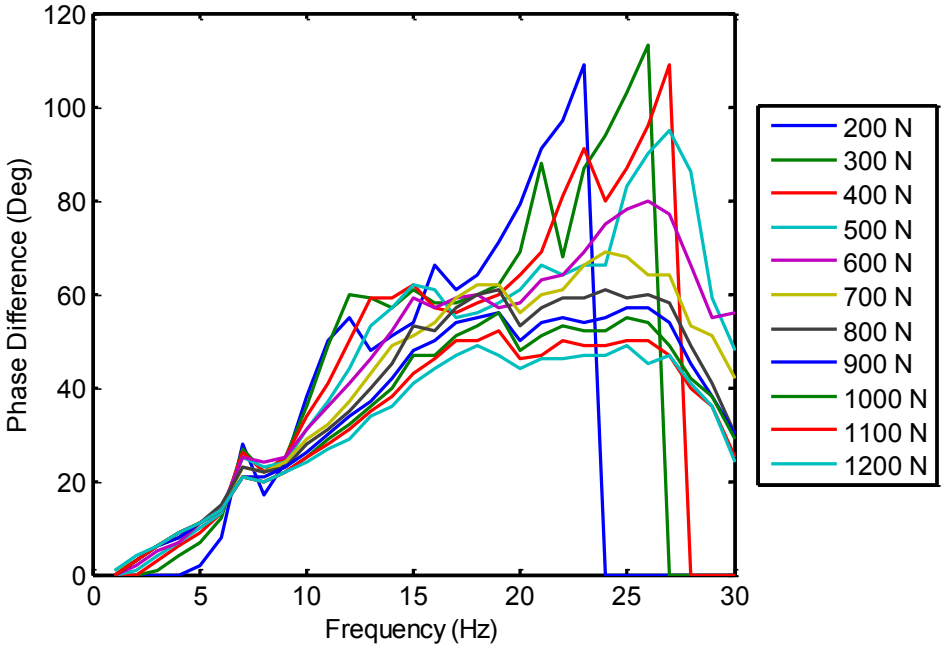

Figure 6.13: Phase difference between AMB 2 applied forces and estimated AMB 2 forces for a frequency range of 1-30 Hz and input force amplitudes of 200-1200 N

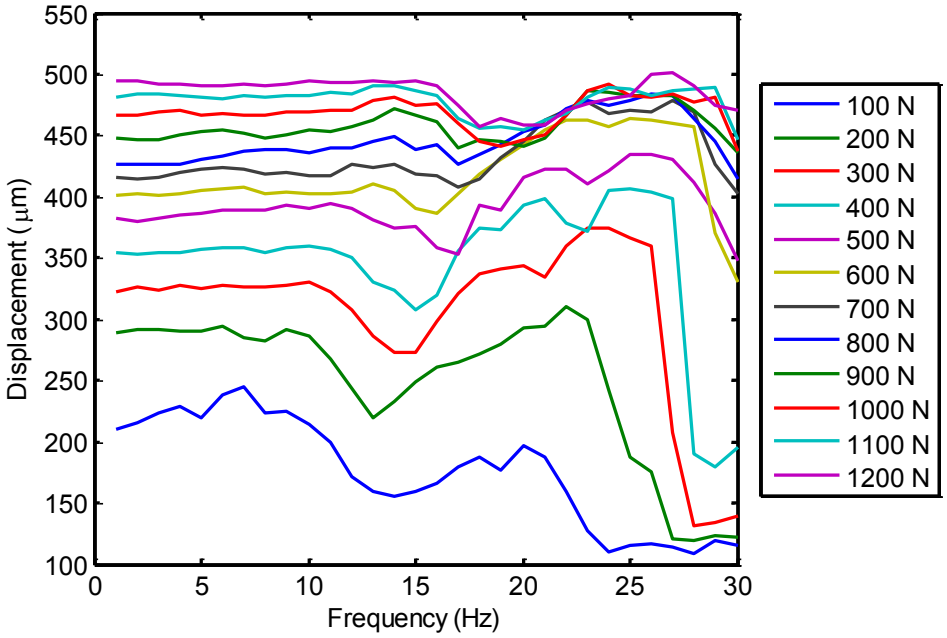

Figure 6.14: Measured displacement amplitudes at the non-driven end for a frequency range of 1-30 Hz covering AMB 2 input force amplitude levels of 100-1200 N

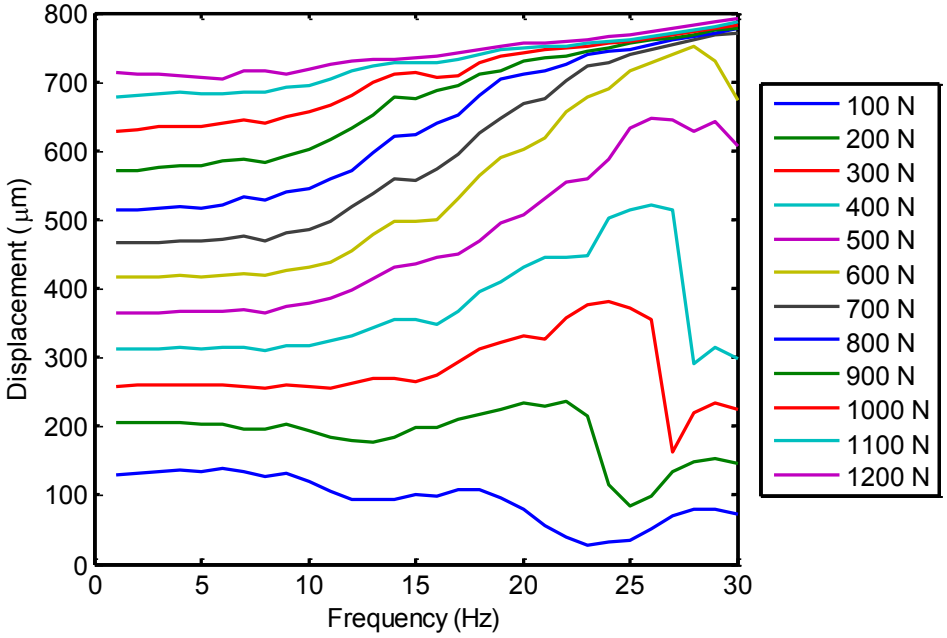

Figure 6.15: Measured displacement amplitudes at AMB 2 for a frequency range of 1-30 Hz covering AMB 2 input force amplitude levels of 100-1200 N

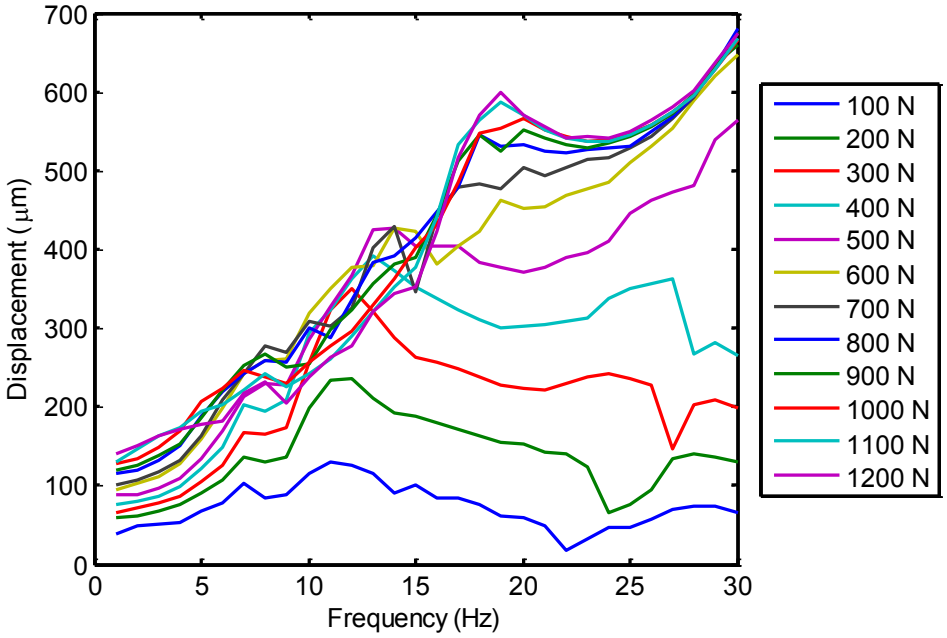

Figure 6.16: Measured displacement amplitudes at AMB 1 for a frequency range of 1-30 Hz covering AMB 2 input force amplitude levels of 100-1200 N

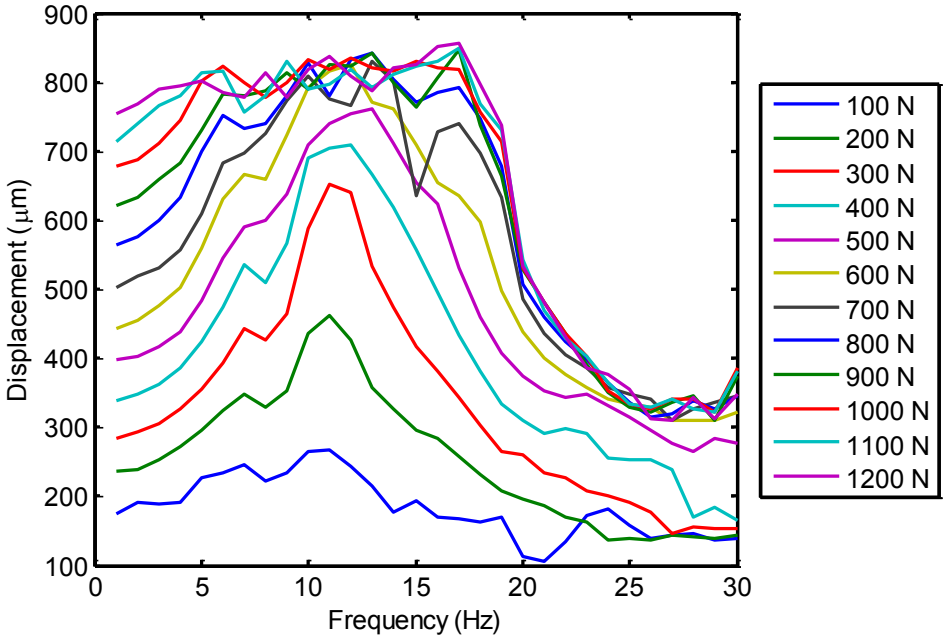

Figure 6.17: Measured displacement amplitudes at the driven end for a frequency range of 1-30 Hz covering AMB 2 input force amplitude levels of 100-1200 N

It is noticed from the figures that no contact occurs at AMB 1 and at the driven end over the force and whirl frequency range considered. However, contact does occur at the AMB 2 touchdown bearing at high force input amplitudes and frequencies generating big orbits, where the rotor/TDB clearance is 750 μm. This generates multiple rotor/TDB contact locations along the rotor, as contact also happens at the non-driven end.

Full rotor/TDB contact occurs at most force levels and frequencies at the non-driven end as the results demonstrate. However, for input forces of 400 N and below, full rubbing contact does not occur at all frequencies, and this behaviour varies for each force level in this range.

Although the rotor/TDB clearance at the force measurement system location is 350 μm, measured displacement amplitudes reach a value of about 500 μm near that location. This is because the displacement sensors are not at the same position as force measurement system along the rotor, and both the rotor and the force measurement system have degrees of flexibility.

It is noticed from the force, phase and displacement data that the rotor passes through the different modes and critical frequencies, while it is levitated with the PID controlled AMBs. Changes at frequencies around 12, 18 and 29 Hz can be observed. The results presented provide experimental data on the system behaviour upon rotor/TDB contact for a wide range of cases.

6.5 Experimental and Simulation Model Results Comparison

6.5.1 Contact Force and Phase Simulation Results

Simulations were undertaken and results were obtained for the same range of contact cases described in the last section to investigate the rotor/AMB/TDB system dynamics theoretically. A total of 360 simulation tests were performed using the 17 node system model, which has nodes corresponding to the displacement sensor locations of the test rig, in addition to the non-driven end TDB location. The parameters of the AMBs and their PID controllers used in the simulations were the same as those of the experimental tests. The input forces in the simulations were in the form of unbalance applied at AMB 2 to simulate AMB control forces. The unbalance forces are expressed as

$$\begin{aligned} F_{uX} &= F_u \cos \Omega t \\ F_{uY} &= F_u \sin \Omega t \end{aligned} \tag{6.11}$$

The gyroscopic matrix of the model was not used in the simulations, in order to simulate the effect of whirl frequencies, as opposed to rotor spinning by the motor. The output forces were obtained from the rotor/TDB contact model, and the relationship between the input and contact forces is defined as

$$F_{cR} = \alpha_c F_{uR} \tag{6.12}$$

where α_c is the calculated contact force amplitude ratio. Figures 6.18 and 6.19 show the calculated contact force amplitude ratio for input unbalance force amplitudes of 100-500 N and 600-1200 N, respectively. The phase difference between the input unbalance force and the resulting contact force was evaluated, and is shown in Figures 6.20 and 6.21 for input unbalance force amplitudes of 200-500 N and 600-1200 N, respectively.

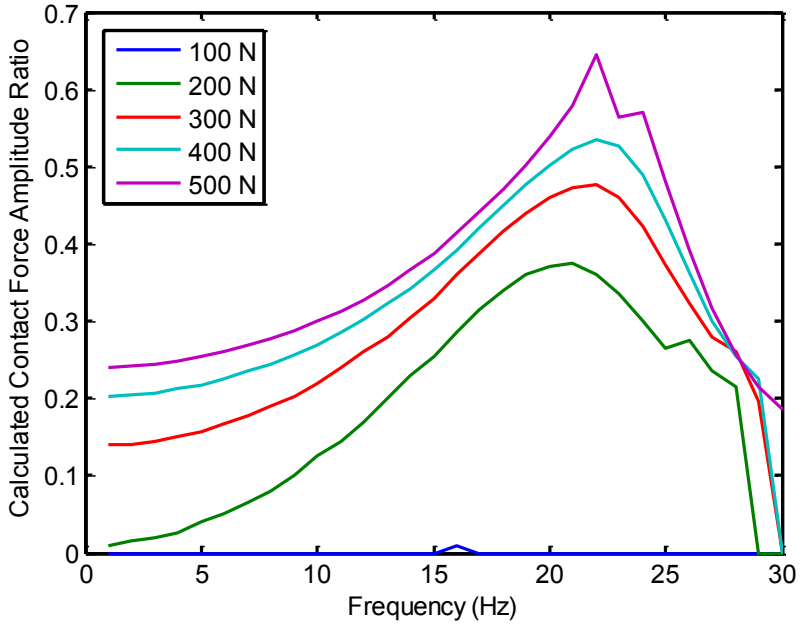

Figure 6.18: Calculated contact force amplitude ratio over a frequency range of 1-30 Hz for input unbalance force amplitudes of 100-500 N

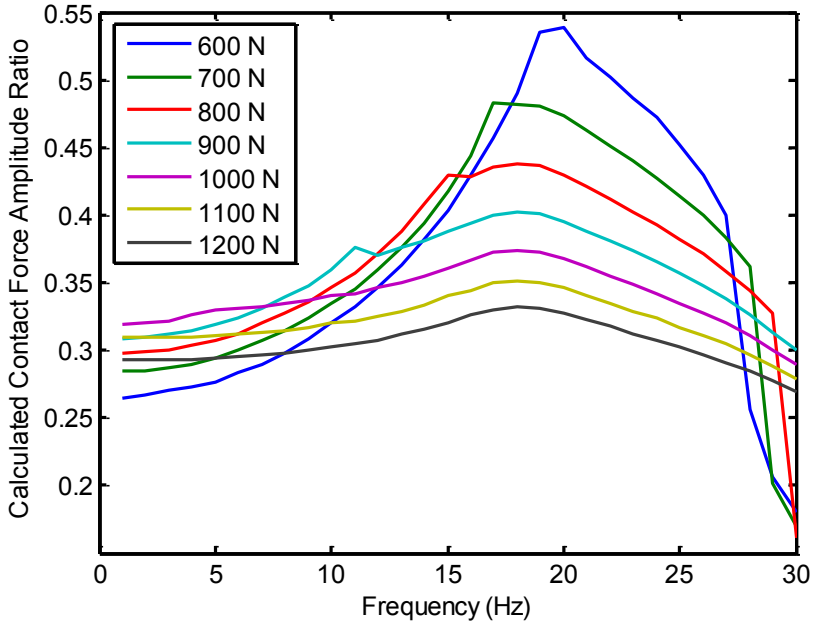

Figure 6.19: Calculated contact force amplitude ratio over a frequency range of 1-30 Hz for input unbalance force amplitudes of 600-1200 N

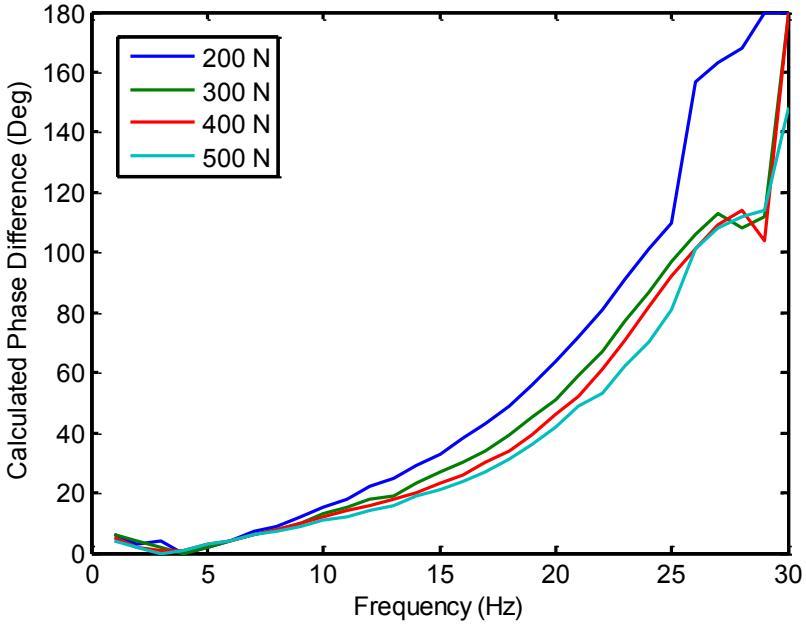

Figure 6.20: Phase difference between input unbalance forces and calculated contact forces at the non-driven end over a frequency range of 1-30 Hz for input unbalance force amplitudes of 200-500 N

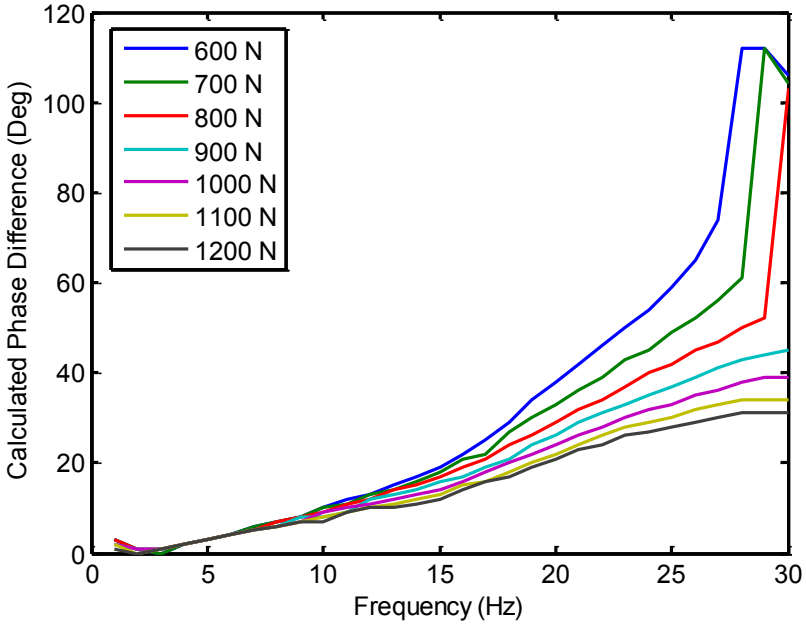

Figure 6.21: Phase difference between input unbalance forces and calculated contact forces at the non-driven end over a frequency range of 1-30 Hz for input unbalance force amplitudes of 600-1200 N

Frequency dependence is evident in all cases. Changes in the force amplitude ratio and phase difference are observed with the increasing input force levels and frequencies.

There are differences in the variation of contact force and phase with frequency between simulation and experimental results. These differences are expected due to the different output forces considered. Although input force levels at the AMB 2 location are similar in the simulations and experiments, the simulation model yields direct rotor/TDB contact forces at the non-driven end, while the experimental results demonstrate estimated AMB 2 forces due to rotor/TDB contact measurements at the non-driven end. Estimated AMB forces are defined by the force measurement system calibration in Chapter 5. However, the main aim of the experiments undertaken was to measure and estimate AMB related forces to enable deriving control data, in contrast to measuring real contact forces. The relationships between the measured estimated AMB forces and the calculated simulation contact forces are explored in the next section.

Differences between simulation and experimental results are also due to other factors. Since the experimental rotor/AMB system is mounted on a base plate with isolators between it and the ground, the base itself can be subject to motion with rotor motion and rotor/TDB contact. The base motion was not modelled in the simulations, which would have an effect on the frequency characteristics of the system. In addition, the characteristics and dynamics of the force measurement system used in the experiments may have an influence on the system dynamics in a different way to the TDB model employed in the simulations.

6.5.2 Measured and Calculated Force Relationships

Estimated AMB forces by the force measurement system outputs are directly related to input AMB forces, while simulation contact forces are modelled to relate to the direct contact forces experienced by the rotor/TDB. In this section, the relationships between the two forces are investigated. The relationships are derived and discussed

based on the tests undertaken over the different rotor frequencies. A relationship between the estimated AMB force and the calculated contact force in a specific contact condition can be expressed as

$$F_{MBR}^{e} = \beta F_{cR} \tag{6.13}$$

where β is the force-force amplitude ratio. To consider this ratio, Figure 6.22 shows the force relationships for a frequency range of 1-12 Hz based on the results presented in the last section.

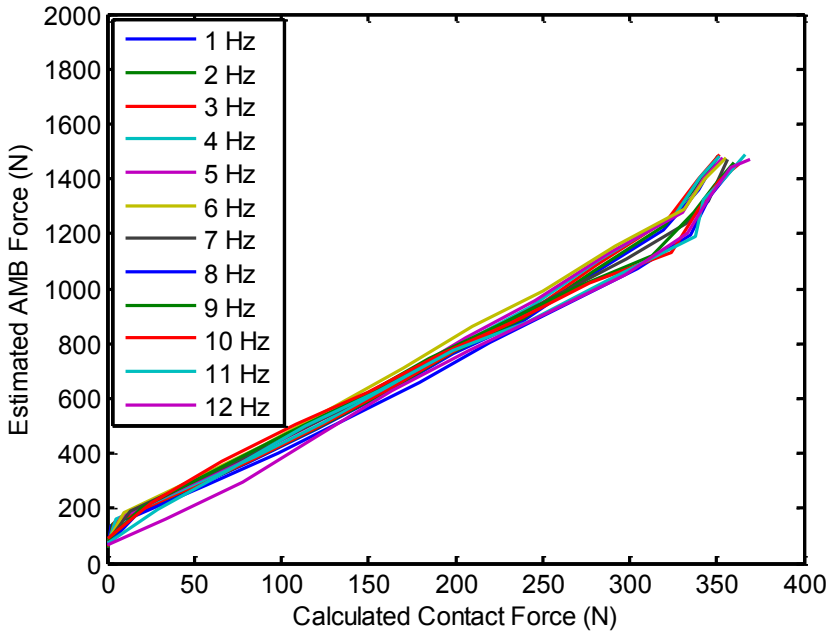

Figure 6.22: Estimated AMB forces vs calculated contact forces at the non-driven end for a frequency range of 1-12 Hz

A first order polynomial fit to the plot presented yields an average value of β of 3.7 for the force and frequency range considered. This value of β covers a frequency range up to the first rotor critical frequency of the conical mode, and resembles the relationship between the estimated AMB force and the direct contact force of

rotor/TDB interaction in these cases. Figure 6.23 shows the force relationships for a frequency range of 13-18 Hz.

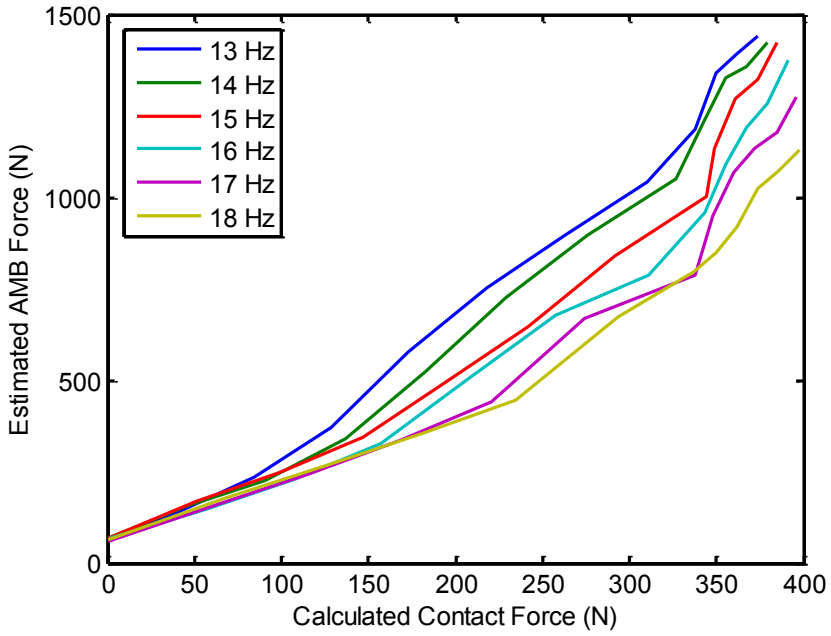

Figure 6.23: Estimated AMB forces vs calculated contact forces at the non-driven end for a frequency range of 13-18 Hz

A first order polynomial fit for the data presented in Figure 6.23 yields an average value of β of 3.2. The values of β in this case are seen to vary and range from 3.7 to 2.7 as the frequencies increase. This shows the dynamic behaviour as the rotor system moves between the conical and cylindrical rotor critical frequencies. A frequency dependent force ratio β is demonstrated.

Figure 6.24 shows the forces for a frequency range of 19-27 Hz. This represents the frequency range between the cylindrical and bending flexural rotor critical frequencies. A first order polynomial fit for the data presented yields an average value of β of 2.5 in this case, lower than the values of the previous frequency ranges.

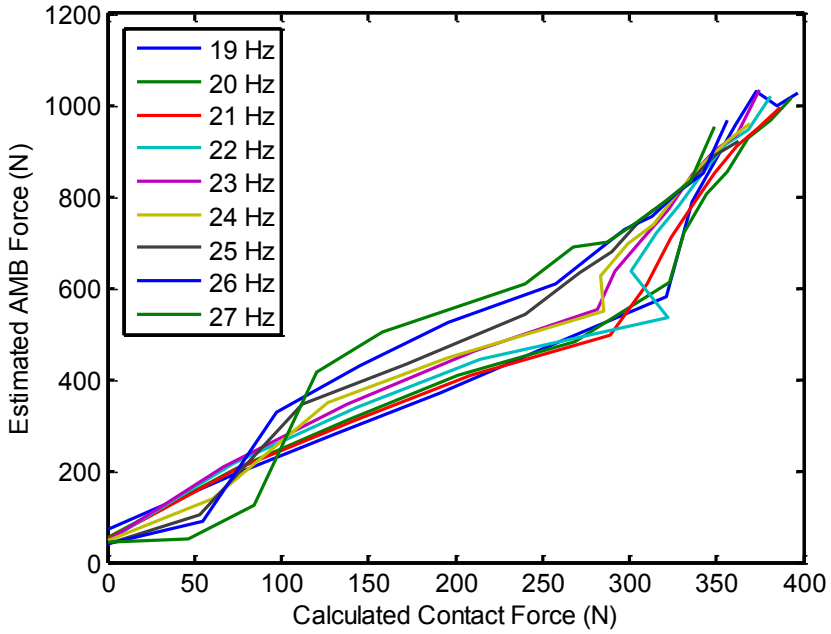

Figure 6.24: Estimated AMB forces vs calculated contact forces at the non-driven end for a frequency range of 19-27 Hz

Figure 6.25 shows the force relationships for the frequency range of 28-30 Hz. A force dependent ratio β is noticed in this case, where the system exceeds the first bending critical frequency. The average value of β is evaluated to be 5.5 up to a 140 N calculated contact force level, after which it decreases to 0.7.

It is demonstrated from the data presented in this section that linear relationships between the estimated AMB forces of the experimental tests and the simulation calculated contact forces can be derived. These relationships vary over different system frequencies. It is noticed that the value of β decreases as the rotor frequency is increased going through the different critical frequencies in the range. The variation of β over different frequencies reflects the rotor system dynamics, including the force measurement system dynamics. If the force measurement system was calibrated to yield direct contact force data, a value of β close to 1 would be expected.

A comparison between the simulation and experimental rotor displacement results for the contact cases considered is presented in the next section.

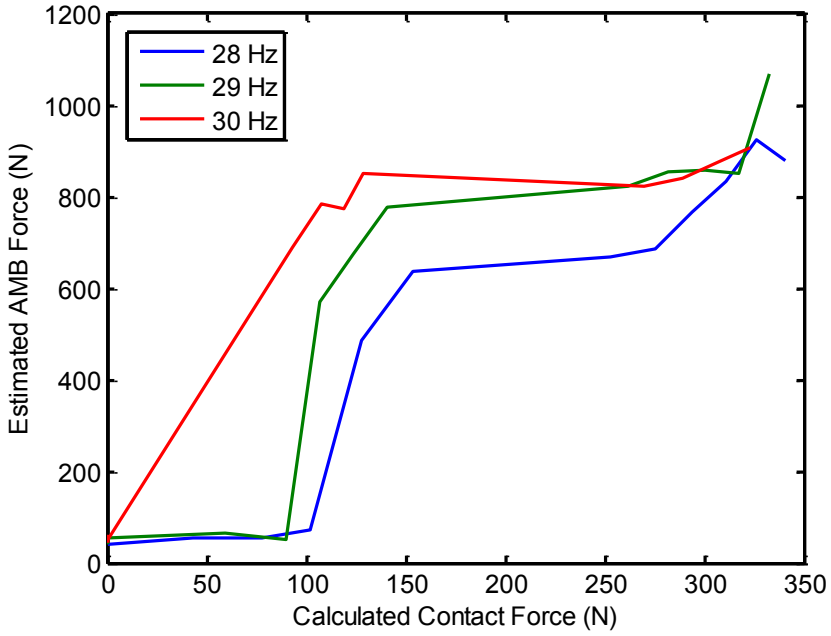

Figure 6.25: Estimated AMB forces vs calculated contact forces at the non-driven end for a frequency range of 28-30 Hz

6.5.3 Measured and Calculated Rotor Displacement

In this section, the measured rotor displacements are compared to the calculated displacements from the simulation model for the contact cases discussed. The displacements at the non-driven end, corresponding to the location of sensors 7 and 8, are shown in Figure 6.26. An AMB 2 input force of 700 N was used in this case. Different frequencies were considered covering the full range. It is demonstrated from the orbits that measured and calculated displacements show good agreement.

To investigate the measured and calculated displacements further, the displacement amplitudes at all the force levels and frequencies considered in the dynamic tests were evaluated. Figure 6.27 shows the measured and calculated displacement amplitudes at the non-driven end, representing the location of sensors 7 and 8 close to the force measurement system TDB, where rotor/TDB contact occurs. Figure 6.28 shows the

displacement amplitudes close to the AMB 2 location, which applies the input forces. This represents the location of sensors 5 and 6. Rotor/TBD contact occurs at high AMB 2 force amplitudes and frequencies at this location. It can be seen that measured and calculated results of both figures show good agreement.

Although the displacement results show good agreement in general, discrepancy between calculated and measured results is present. Differences are evident through slightly different rotor displacement amplitudes. Additionally, different rotor/TDB contact behaviours can be noticed in rotor orbits, including what appears as rotor bouncing motion in certain experimental measurements, as opposed to full rubbing motion in calculated orbits. These differences are due to a number of factors, primarily model inaccuracies, measurement errors, and rotor/TDB misalignment issues in the experimental setup.

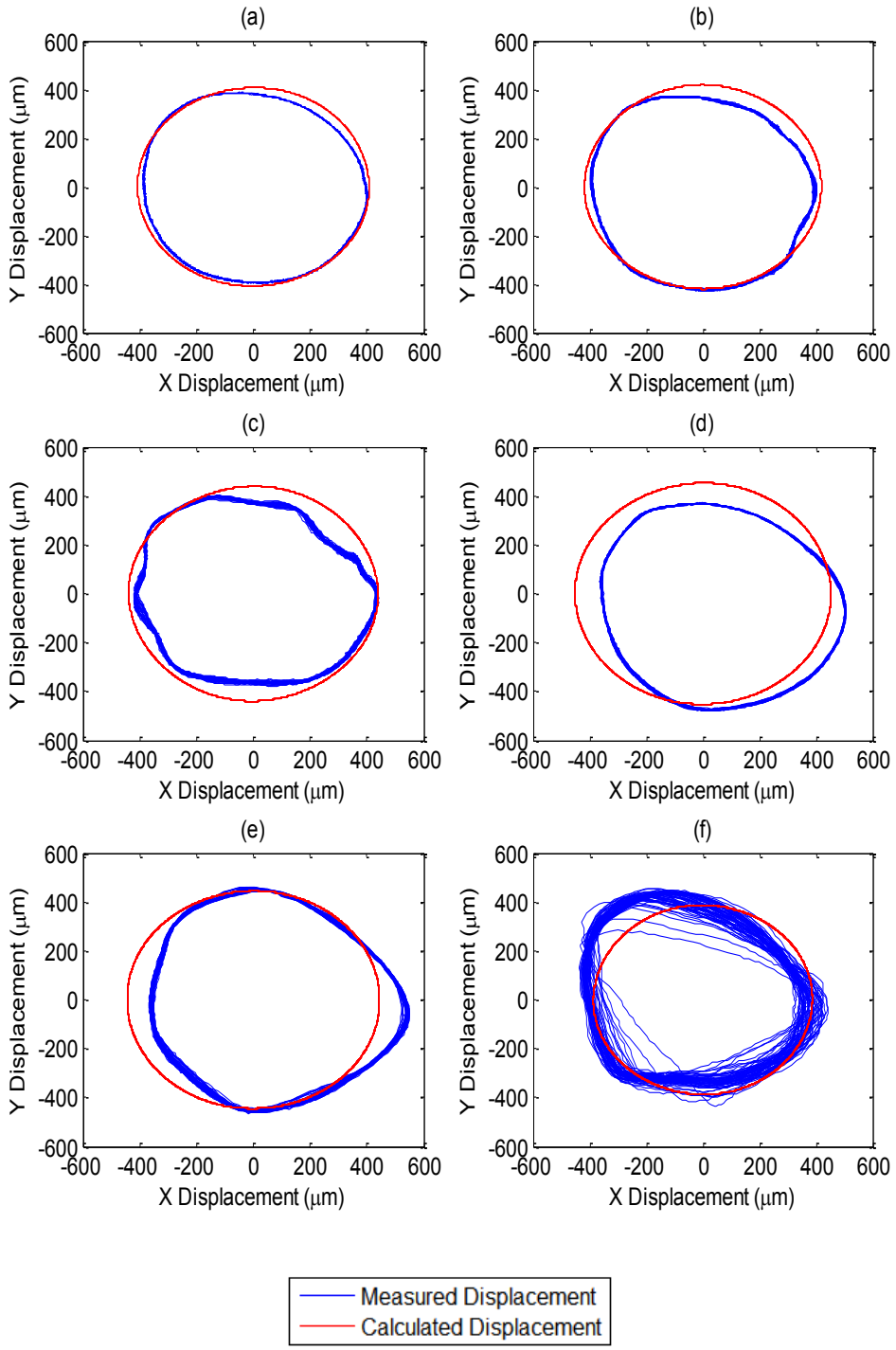

Figure 6.26: Measured and calculated orbits for rotor contact at the non-driven end TDB for an AMB 2 input force of 700 N at (a) 5 Hz (b) 10 Hz (c) 15 Hz (d) 20 Hz (e) 25 Hz (f) 30 Hz

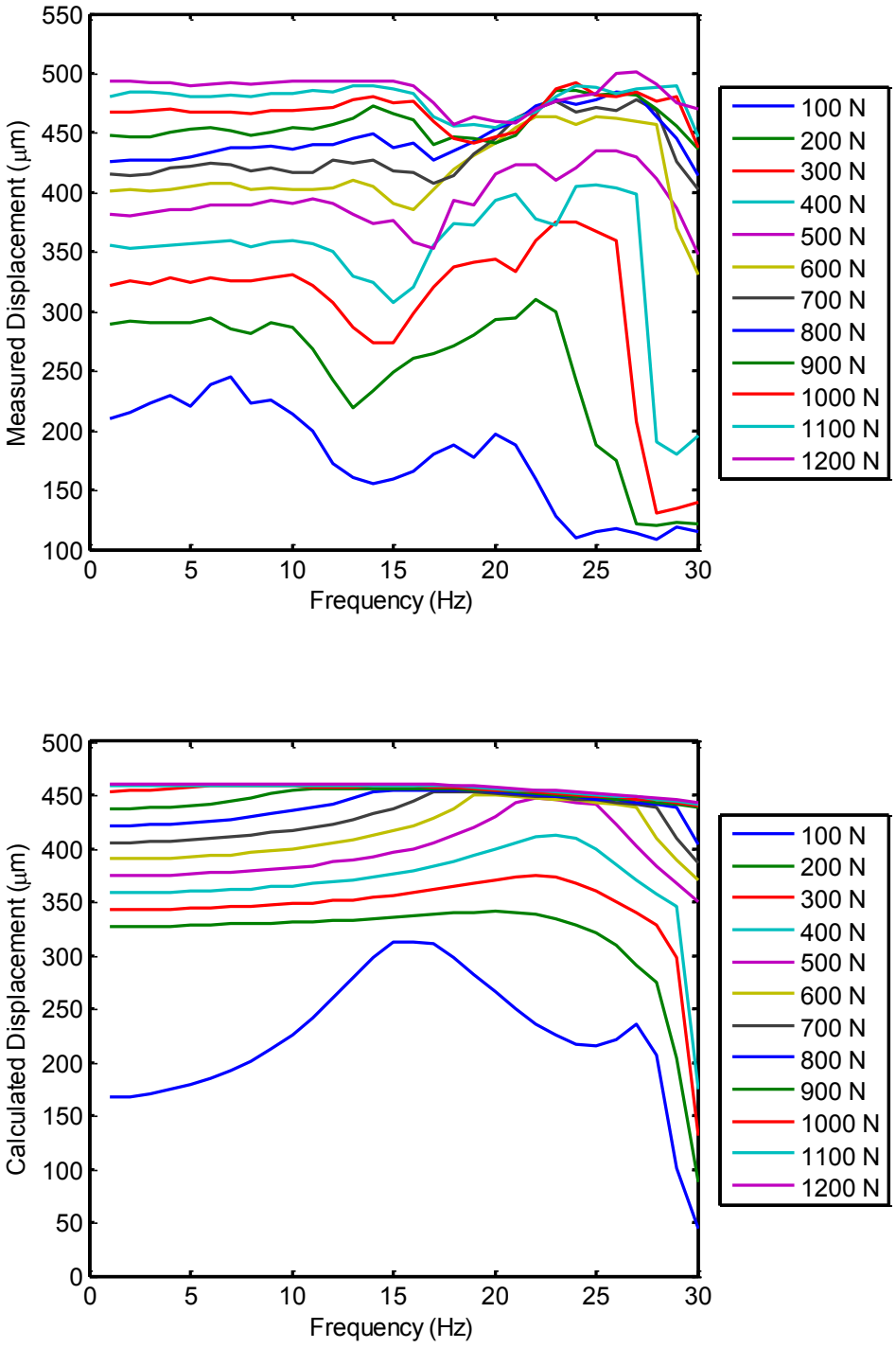

Figure 6.27: Measured and calculated displacement amplitudes at the non-driven end for a frequency range of 1-30 Hz covering AMB 2 input force levels of 100-1200 N

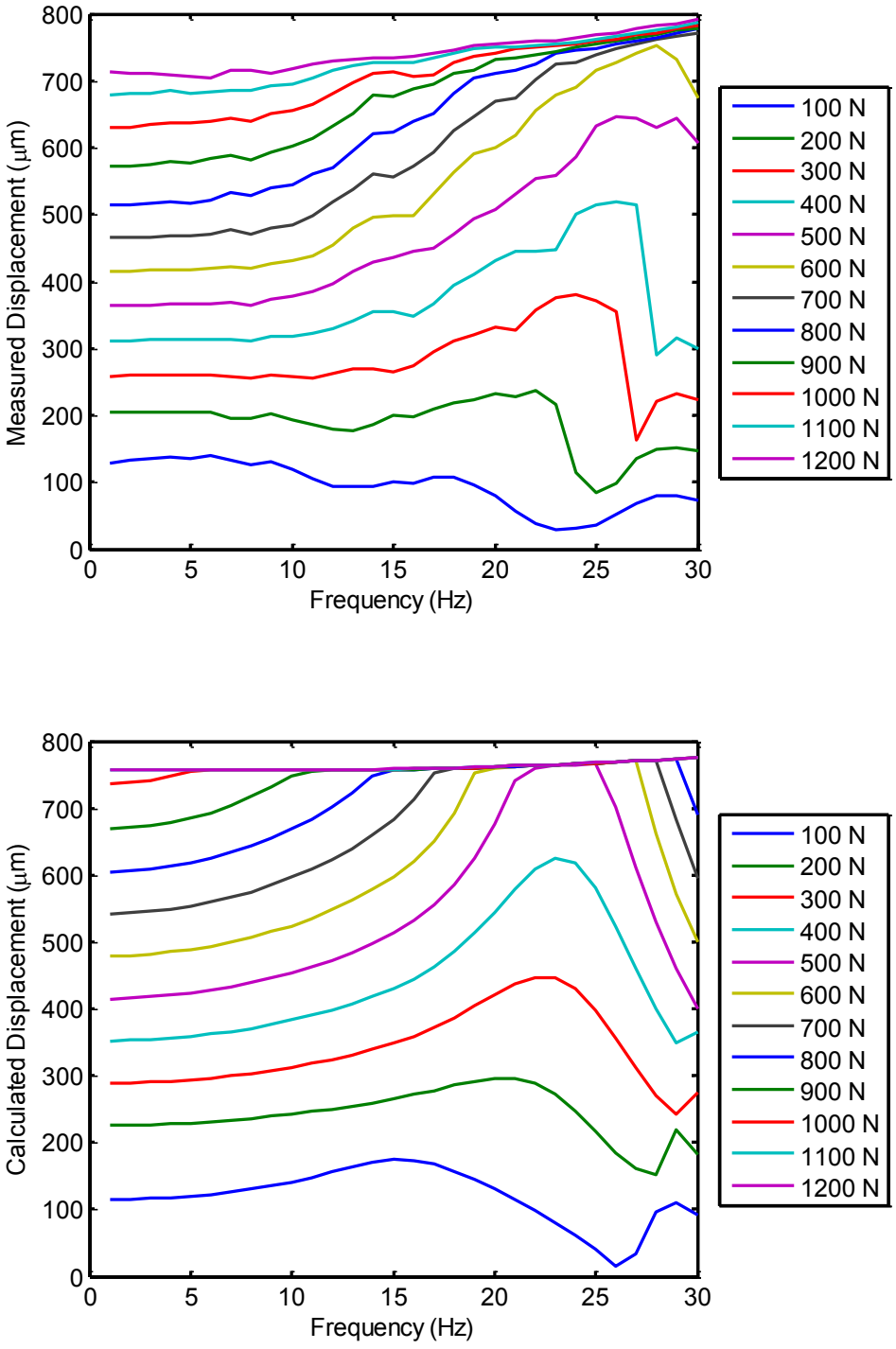

Figure 6.28: Measured and calculated displacement amplitudes at AMB 2 for a frequency range of 1-30 Hz covering AMB 2 input force levels of 100-1200 N

6.6 Closure

The dynamic behaviour of the experimental rotor/AMB/TDB system was investigated through a series of dynamic tests using the force measurement system. Dynamic forces and phases were assessed and demonstrated from the force measurement system outputs. Additionally, displacement sensor measurements were presented showing the contact dynamics of the system. The frequency dependent behaviour of the system was demonstrated and discussed for all results. Simulation results were presented, and the relationship between the calculated contact force and the estimated AMB force, which was based on experimental results, was explored. Moreover, measured and calculated rotor displacements were compared.

Chapter 7

CONTROL STRATEGY FOR CONTACT RECOVERY BASED ON FORCE MEASUREMENT

7.1 Overview

The control of rotor/TDB contact and vibration through force measurement data is explained in this chapter. Static and dynamic calibration tests of the strain gauge based force measurement system are analysed and employed to provide the control data. Vibration attenuation of an unbalanced rotor in persistent rotor/TDB contact at various running frequencies is explored with respect to recovery from contact. The control is performed in open-loop through applied AMB forces. Experimental results are demonstrated and discussed.

7.2 Control System Description

In order to experimentally validate rotor recovery from contact using force measurement data, an open-loop control strategy is used employing the magnetic bearings for applying control forces. During a rotor/TDB contact condition, the force signals obtained from the force measurement system are used to specify the appropriate control force and phase to recover the rotor, based on dynamic contact tests that were implemented at various rotor whirl frequencies and AMB force levels. This is done while the PID controllers of both magnetic bearings are fully functional.

Figure 7.1 shows the control structure, where the estimated AMB force amplitude at the measurement system location F^{e}_{MBR} is used to specify the appropriately phased control force, $\mathbf{f_i}$, needed for the contact-free recovery of the rotor. The rotor/TDB contact behaviour is observed using both the displacement and force measurements.

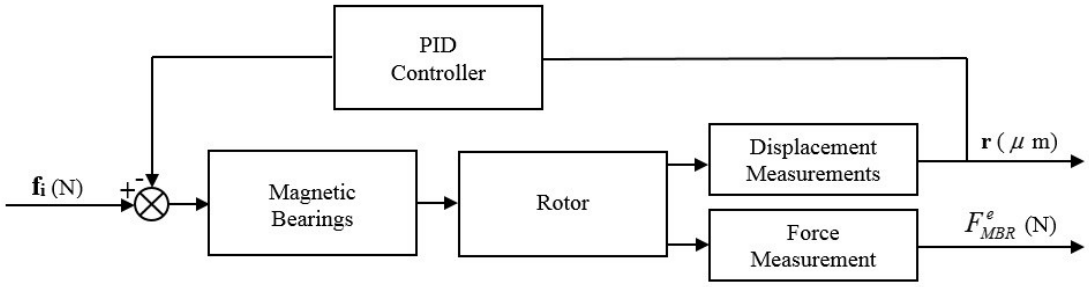

Figure 7.1: Block diagram showing the structure of open-loop force based control and PID feedback control for the flexible rotor/bearing system

The input control force, $\mathbf{f_i}$, is obtained from the dynamic tests relating an input AMB force amplitude, $\hat{F}_{MB}$, to the estimated AMB force amplitude, F^{e}_{MBR}, at a whirl frequency, ω, and has an amplitude equal to that of $\hat{F}_{MB}$. For a given force measurement of F^{e}_{MBR}, the control force $\mathbf{f_i}$ consists of the X and Y components as follows

$$\begin{aligned} F_{iX} &= \hat{F}_{MB}\cos(\Omega t + \phi_i) \\ F_{iY} &= \hat{F}_{MB}\sin(\Omega t + \phi_i) \end{aligned} \tag{7.1}$$

where $\Omega = \omega$, and:

$$\phi_i = \pm(\phi_R - 180) \tag{7.2}$$

The control phase, ϕ_i, is obtained using the dynamic tests that yield the phase difference, ϕ_R, between the input AMB force and the estimated AMB force, for an

input $\hat{F}_{MB}$. The control phase is applied with a 180 degrees phase shift in order to generate an equal and opposite force to recover the rotor from contact.

7.3 Experimental Procedure

7.3.1 Rotating Rotor/TDB Contact

To arrive at rotor/TDB contact conditions, rotor unbalance near the measurement system location is introduced, while the rotor is spun by the motor at rotational frequencies that result in full rotor/TDB contact at the measurement system location. Tests are done with a 52 g unbalance mass, which is used on the disk at the non-driven end. The radius of the disk is 0.12 m, and the mass was positioned at a distance of 0.02 m from the edge of the disk, therefore giving an eccentricity of 0.1 m. This gives an unbalance value of *me* of 5.2 gm.

Run-up tests were undertaken with the unbalanced rotor over a rotational frequency range of 0-28 Hz to observe the rotor's behaviour. The motor of the test rig was used with a speed that was increased steadily by 1 Hz increments. The steady-state average displacement amplitude at each rotating frequency was obtained at the non-driven end. Tests were performed without a TDB at the measurement system location, and were performed again with the TDB in place to show the contact behaviour, where the radial clearance between the rotor and the TDB is 350 μm. Figure 7.2 shows the results of both tests.

At this unbalance level, the rotor is seen to make full contact with the force measurement system's touchdown bearing starting at a rotational frequency of 13 Hz, where the displacement amplitude is seen to exceed 300 μm at the non-driven end sensors' location. When the bearing is removed, an amplitude peak of 750 microns is seen at 19 Hz.

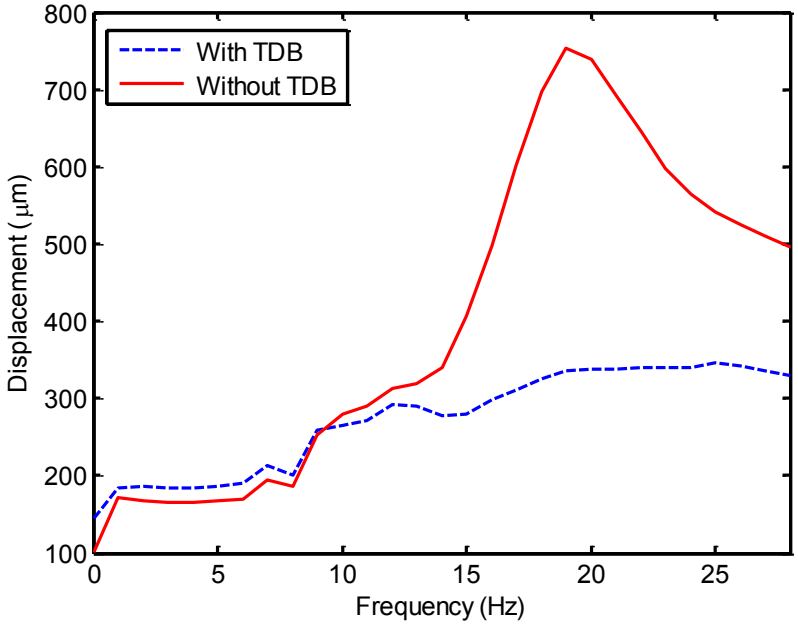

Figure 7.2: Run-up tests showing the measured displacement amplitude at the non-driven end for a rotating frequency range of 0-28 Hz at an unbalance of 5.2 gm

The orbits at the frequency of 19 Hz are shown in Figure 7.3, when the TDB is used at the measurement system location. It is noted that while the orbit at the non-driven end demonstrates full rub contact, the orbits at the other three locations demonstrate no rotor/TDB contact, as they are within the clearance ranges of the TDBs at those locations. This shows that single location contact occurs at this frequency and unbalance level, while at higher unbalance forces or frequencies contact may occur at more than one location. The natural frequency of 19 Hz corresponds to the cylindrical mode of the rotor system, where contact only occurs at the unbalance location at the non-driven end. Multiple location contact may occur at different frequencies, including those related to the conical mode of the rotor system, in addition to those of the flexural modes at higher rotating frequencies. Based on these tests, a rotating frequency range of 17-21 Hz was selected to analyse the force levels at the measurement system and test the control strategy with the unbalanced rotor.

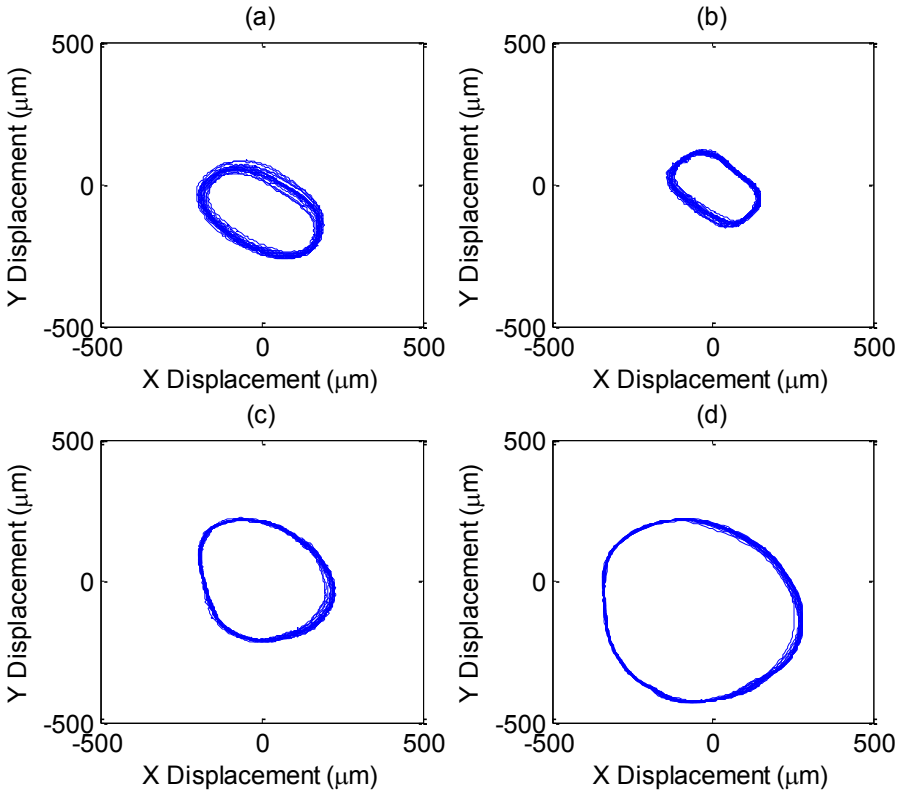

Figure 7.3: Orbits at a rotating frequency of 19 Hz with an unbalance of 5.2 gm, at (a) driven end (b) AMB 1 (c) AMB 2 (d) non-driven end with the TDB

7.3.2 Static Calibration and Dynamic Tests

Since the force measurement system was removed from the test rig and then re-installed before testing the control system, the measurement system was re-calibrated using static and dynamic tests based on AMB forces, for the purpose of testing the control strategy over the selected frequency range. The calibration methodology explained in Chapter 5 and tested dynamically in Chapter 6 was used.

The estimated AMB force X and Y components at the measurement system location were calibrated against X and Y forces applied by AMB 2 of the test rig. Static calibration was performed with the whirl frequency ω set to zero, and without

rotational (motor) frequency. A series of static radial forces ranging up to 1100 N were applied over a range of angles covering 360 degrees through AMB 2. The measured voltages from the strain gauge system were related directly to the *X* and *Y* radial forces at the measurement system with a calibration matrix. A calibration matrix was estimated by recording 80 sets of experiments with different input force amplitudes and phase angles.

Figures 7.4 and 7.5 show the relationships between the applied input forces and the estimated AMB forces in the *X* and *Y* components. Figure 7.6 shows the relationship between the applied and estimated angles.

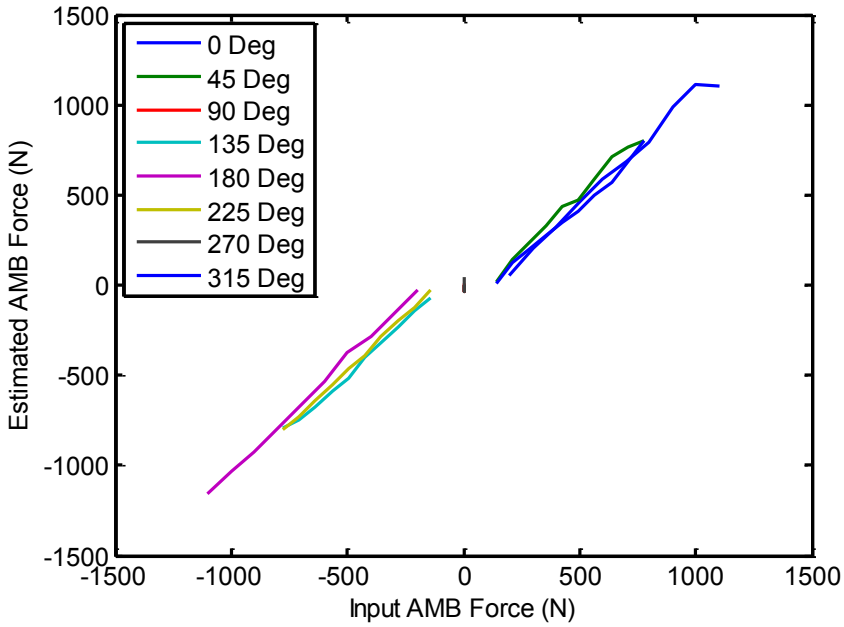

Figure 7.4: X-axis static AMB 2 forces at phase angles: 0, 45, 90, 135, 180, 225, 270 and 315 Deg

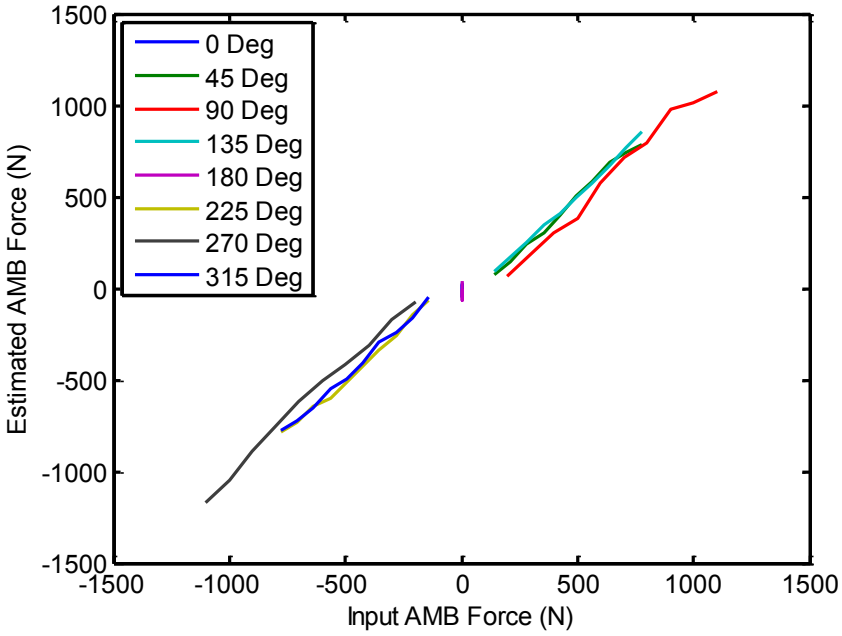

Figure 7.5: Y-axis static AMB 2 forces at phase angles: 0, 45, 90, 135, 180, 225, 270 and 315 Deg

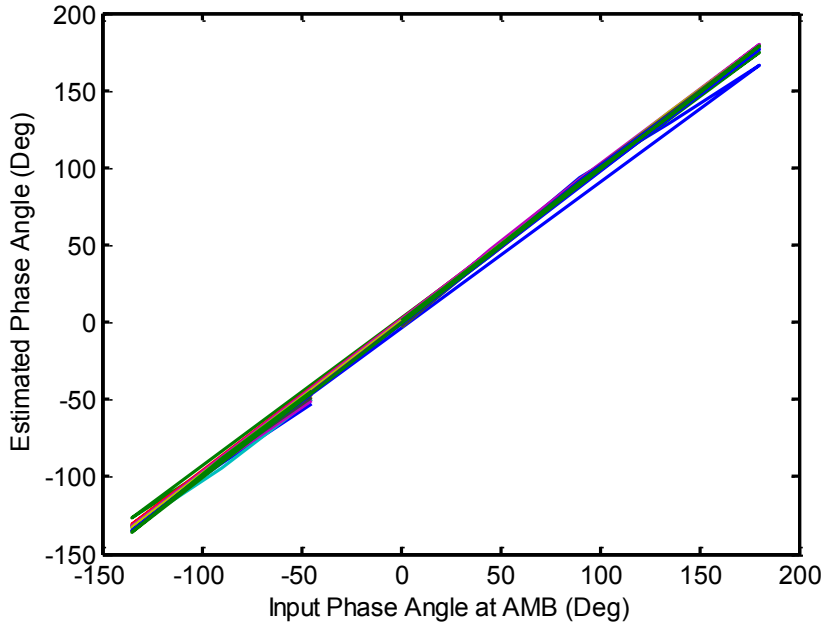

Figure 7.6: Phase angle variation with static AMB 2 forces over an input force amplitude range of 300-1100 N

Based on the calibration matrix estimated from the static calibration tests, which is demonstrated through the relationship between the static input and estimated forces, dynamic tests were performed over the whirl frequency range of 17-21 Hz. Different AMB input force amplitudes were applied. This is to identify the relationship between input AMB forces and estimated AMB forces for that frequency range.

The dynamic input forces were applied through AMB 2, and the resultant estimated AMB forces were evaluated using the calibration matrix. No rotation was applied to the rotor. Full PID control action at both AMBs was operational.

Figure 7.7 shows the dynamic behaviour of the system at applied AMB force inputs of 300-600 N over a whirl frequency range of 17-21 Hz. Each estimated AMB force value in the figure represents the mean value of the resultant estimated AMB force amplitude corresponding to the AMB input force level and frequency. The frequency dependence on the rotor is noted, with peaks showing at the 20 Hz whirl frequency. Figure 7.8 shows the overall phase difference values between the applied AMB forces and the estimated AMB forces for the same input force levels and whirl frequency range.

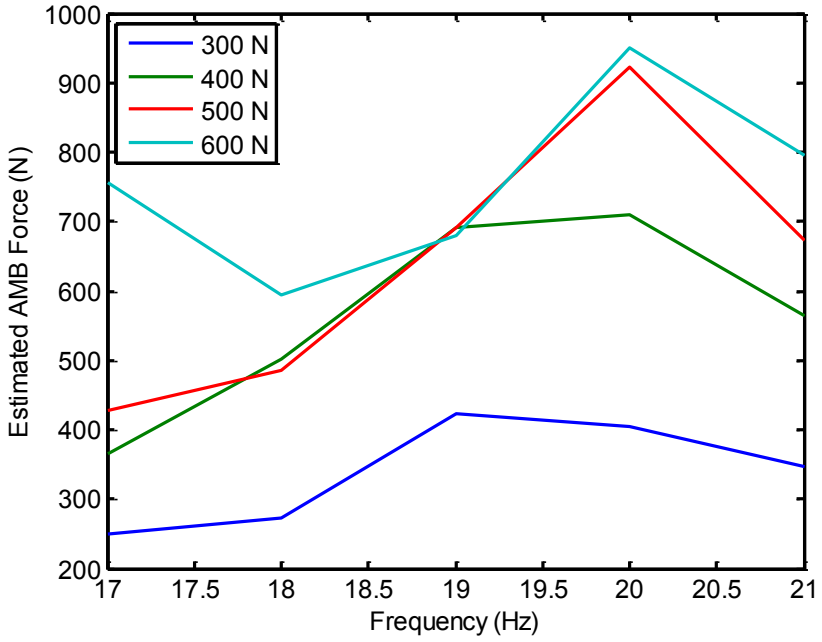

Figure 7.7: Estimated AMB 2 forces over a frequency range of 17-21 Hz for an applied AMB 2 force input range of 300-600 N

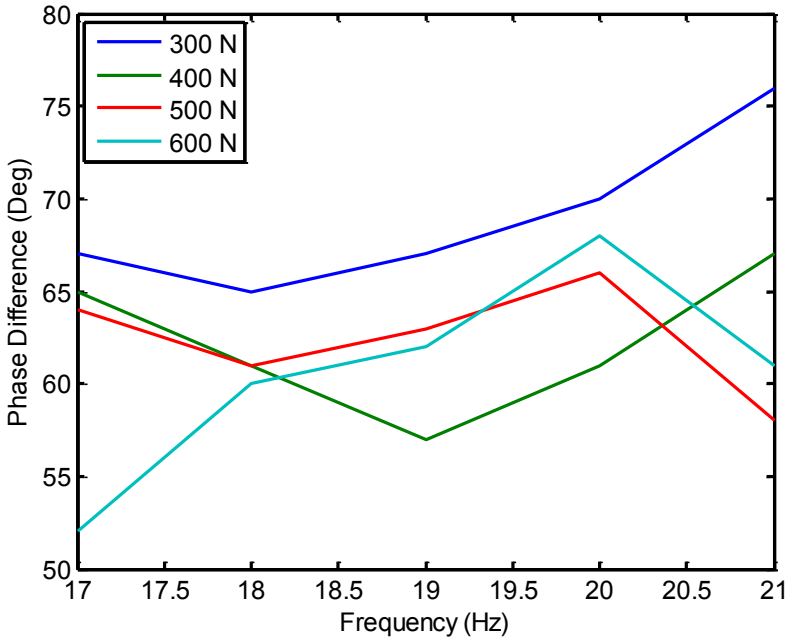

Figure 7.8: Phase difference between input AMB 2 forces and estimated AMB 2 forces for a frequency range of 17-21 Hz covering an applied AMB 2 force input range of 300-600 N

The displacement amplitudes at each frequency and force level were measured during the dynamic tests. Figure 7.9 shows the displacement at all sensor locations. The rotor/TDB radial clearance at the driven end is 900 μm, while it is 750 μm at both AMB locations. The rotor/TDB clearance at the force measurement system position is 350 μm. It is noticed that at the force levels and frequency range applied, rotor/TDB contact only occurs at a single location, which is where the force measurement system is located, close to the non-driven end displacement sensors. Full contact occurs at all the force levels and frequencies applied at that location. These data can hence be employed in controlling single location contact through AMB 2 forces, while at higher AMB force levels and whirl frequencies contact would occur at more than one location.

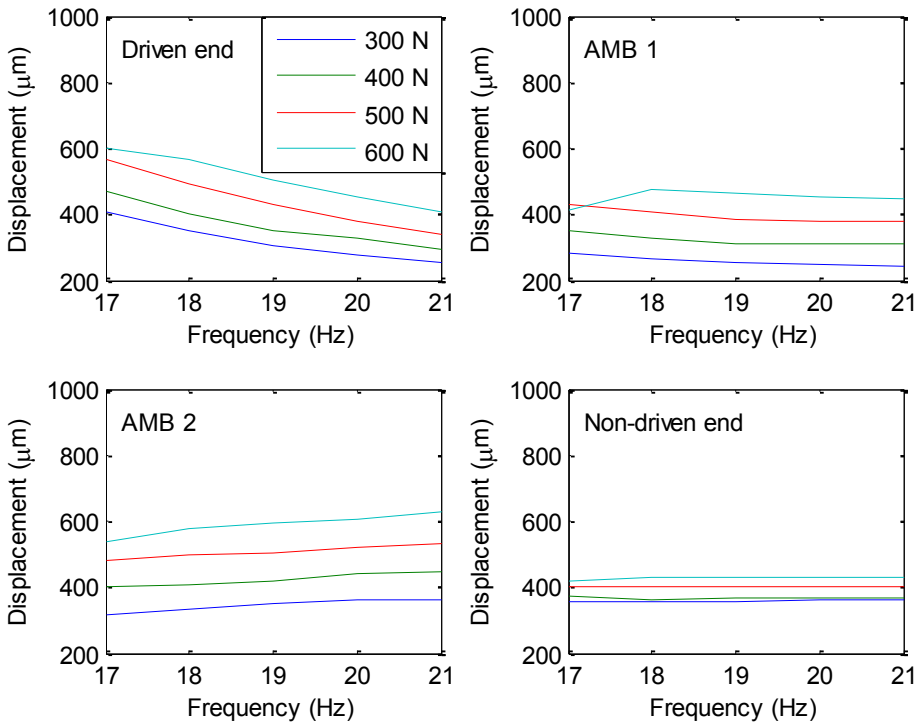

Figure 7.9: Displacement amplitudes at the four sensor locations over a frequency range of 17-21 Hz for an applied AMB 2 force input range of 300-600 N

7.3.3 Control Force Assessment

For a given unbalance causing rotor/TDB contact, the estimated AMB force levels and the required control force amplitudes and phases can be assessed, based on the static and dynamic calibration tests. Unbalance forces causing contact are assessed by using the mean value of the steady-state resultant estimated AMB force. This is achieved by using the estimated calibration matrix and the measured voltages due to contact. Control forces are estimated using the dynamic contact tests, where for any frequency value and estimated AMB force level within the range, the data of Figure 7.7 yields an input AMB force level that would have caused similar contact. This input force level is then to be used in contact control.

The control phase can be obtained from the dynamic calibration tests after determining the input AMB control force amplitude, using the data presented in Figure 7.8. For any input AMB force level and rotor frequency, the phase difference value between input and estimated forces is obtained. This phase difference is used with a 180 degrees phase shift as the control phase, together with the control force amplitude, as presented in Equations (7.1) and (7.2).

Figure 7.10 shows the estimated AMB forces caused by an unbalance of 5.2 gm, over a rotating frequency range of 17-21 Hz. Based on the estimated AMB forces, the control force levels, which are equal in amplitude to input AMB forces, are also evaluated and plotted. Frequency dependent force relationships for the specified unbalance are noticed at both the estimated and control forces.

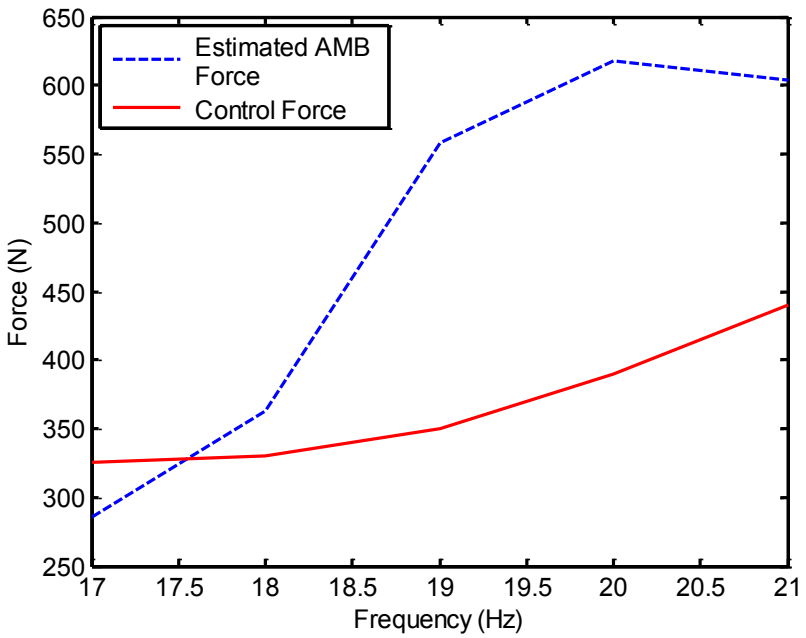

Figure 7.10: Estimated AMB forces and control forces for a frequency range of 17-21 Hz at an unbalance of 5.2 gm

The estimated forces start at a value of 286 N at 17 Hz, and reach a value of 604 N at 21 Hz, while the control forces start at 325 N at 17 Hz, and reach a value of 440 N at 21 Hz. This corresponds to force amplitude ratios α of 0.88 and 1.37, respectively. Figure 7.10 demonstrates a peak at the frequency of 20 Hz, where the estimated force is 618 N, and the control force is 390 N. This gives a peak force amplitude ratio of 1.58. This corresponds to a system natural frequency whilst rotor/TDB contact occurs.

With an unbalance of 5.2 gm over the 17-21 Hz frequency range, contact occurs at the unbalance location, while at higher unbalance levels and higher frequencies multiple location contact may occur. Additionally, at significantly higher contact levels, the required AMB control forces may have high amplitudes causing contact at the AMB location with the unbalanced rotor, creating multiple location contact. However, the tests undertaken were limited to the single location contact case.

Figure 7.11 shows the corresponding control phase values ϕ_i for the same unbalance. The maximum control phase value of 118 Deg is at the frequencies of 19 and 20 Hz. Thus at the frequency of 20 Hz, an increase in the force amplitude ratio is noticed, in addition to an increase in the control phase value. This shows close correlation with the results of Figure 7.2, where a peak is noticed at a rotating frequency of 19 Hz, corresponding to the cylindrical mode of the rotor system.

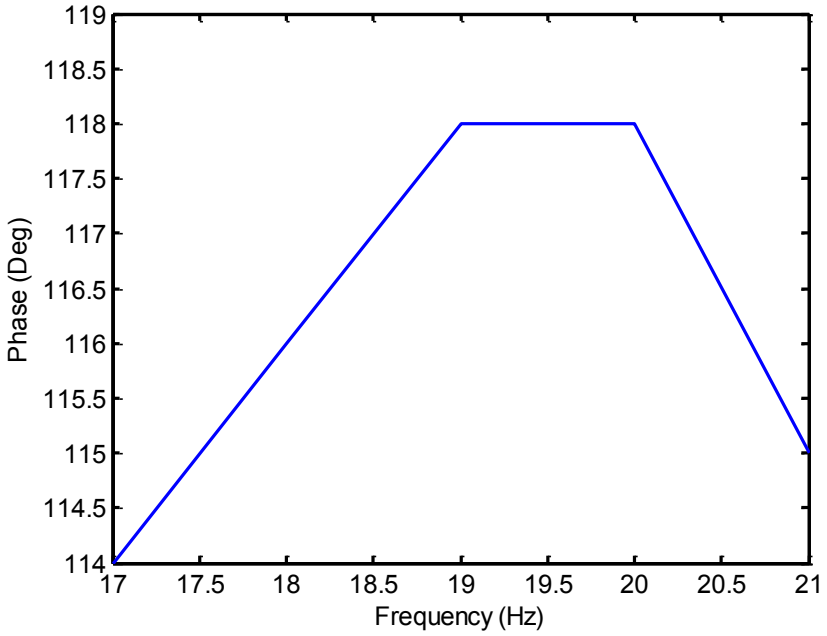

Figure 7.11: Control phase values for a frequency range of 17-21 Hz for an unbalance of 5.2 gm

Based on the data of Figures 7.10 and 7.11, the identified AMB control force amplitudes and phases could be employed to recover the spinning rotor from contact. This is now considered in the next section.

7.4 Unbalance Control Tests

The objective was to use the force measurement system and estimated AMB forces to determine appropriate control forces for AMB 2. The control forces are to be applied as synchronous AMB 2 forces at the rotating frequency Ω, as described by Equation (7.1). The time t is substituted by a cyclic time referred to as the base time, shown in Figure 7.12. The time is set to be zero at the start of each synchronous cycle, triggered by an encoder signal, which gives one pulse per revolution. The running time of the tests is therefore time repeated with synchronous cycles with the periodic time T. This

process enables synchronous AMB forces to be applied, and allows for variations of rotor speed during contact events.

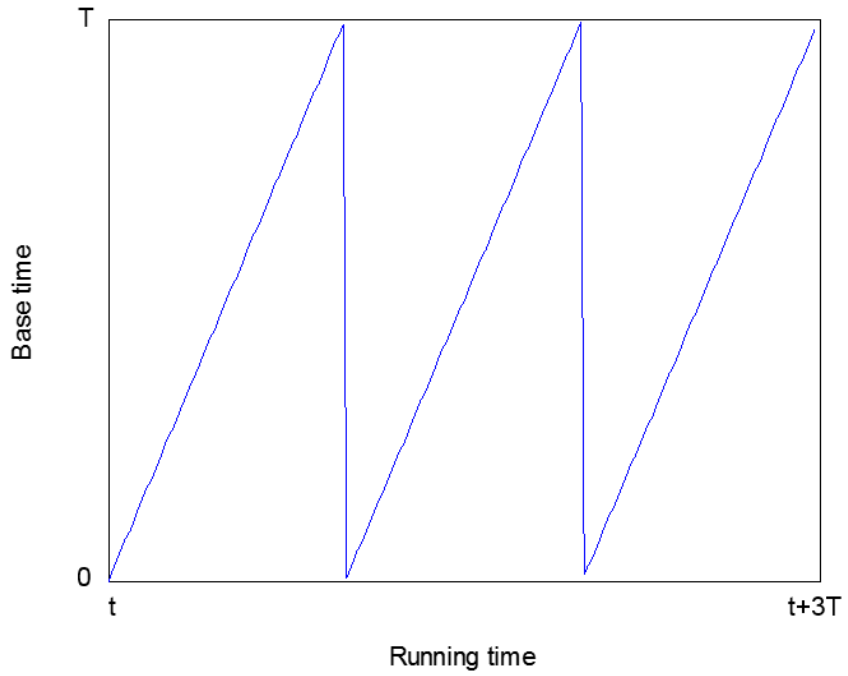

Figure 7.12: Base time used in applying synchronous AMB forces

Control forces are to be applied as open-loop forces, while the PID controllers of both magnetic bearings are still in operation. The values of PID parameters used are identical for both AMBs, and are shown in Table 7.1.

Table 7.1: PID control parameters

PID Control Parameter	**AMB 1**	**AMB 2**
$K_i K_P$ (N/μm)	3	3
$K_i K_I$ (N/s/μm)	0.3	0.3
$K_i K_D$ (Ns/μm)	0.005	0.005

The data of Figures 7.10 and 7.11 were used for controlling an unbalance of 5.2 gm applied at the non-driven end. The control forces were applied through AMB 2, and the output from the displacement sensors of the non-driven end was recorded. Figure 7.13 shows the response before and after control for rotating frequencies of 17 and 21 Hz.

Full rubbing contact is noticed at the start, caused by the unbalanced rotor. After the appropriate control force amplitudes and phases were applied, the displacement decreased at both frequencies. The steady-state dynamic response shows the rotor recovered from contact under the control forces. In this case, a synchronous AMB 2 force amplitude of 325 N was applied with a control phase of 114 Deg at 17 Hz, and a force amplitude of 440 N was applied with a control phase of 115 Deg at 21 Hz.

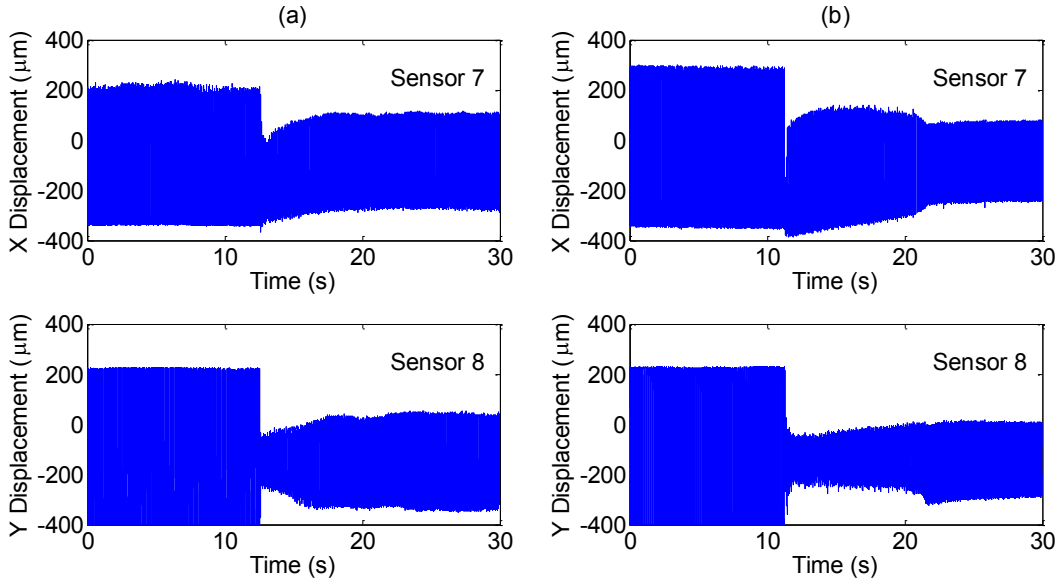

Figure 7.13: Measured displacements at the non-driven end showing the effect of open-loop control based on force measurement at (a) 17 Hz and (b) 21 Hz

Similar tests were undertaken for the whole frequency range of 17-21 Hz, and the resulting orbits are shown in Figure 7.14. Full contact is seen at all frequencies before the open-loop control is applied. Both the transient and steady-state responses of the

rotor orbit are demonstrated after control, and the steady-state response shows the rotor successfully recovered from contact at all frequencies with the synchronous control forces applied.

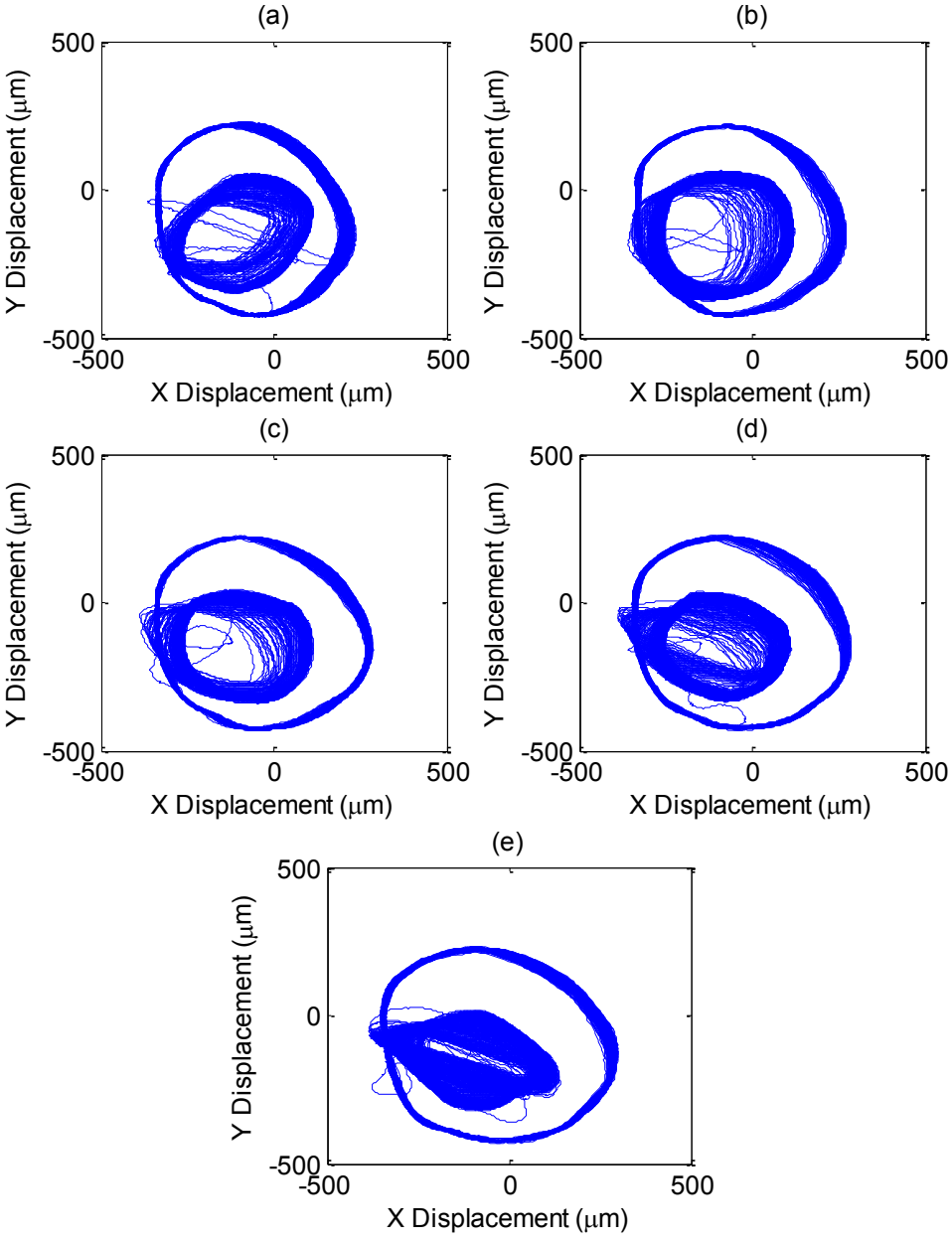

Figure 7.14: Orbits at the non-driven end showing the effect of open-loop control based on force measurement at (a) 17 Hz (b) 18 Hz (c) 19 Hz (d) 20 Hz (e) 21 Hz

Tests were performed at the frequency of 19 Hz to arrive at the maximum AMB 2 control forces that can apply on the unbalanced rotor, causing maximum vibration reduction. While a control force amplitude of 351 N and a control phase of 118 Deg were evaluated to recover the rotor from contact based on force measurement data, it was found that a control force amplitude of 280 N with a phase of 110 Deg causes maximum displacement reduction for the unbalanced rotor. Figure 7.15 shows the results of both cases. Both cases show the rotor completely recovered from full contact after control was applied.

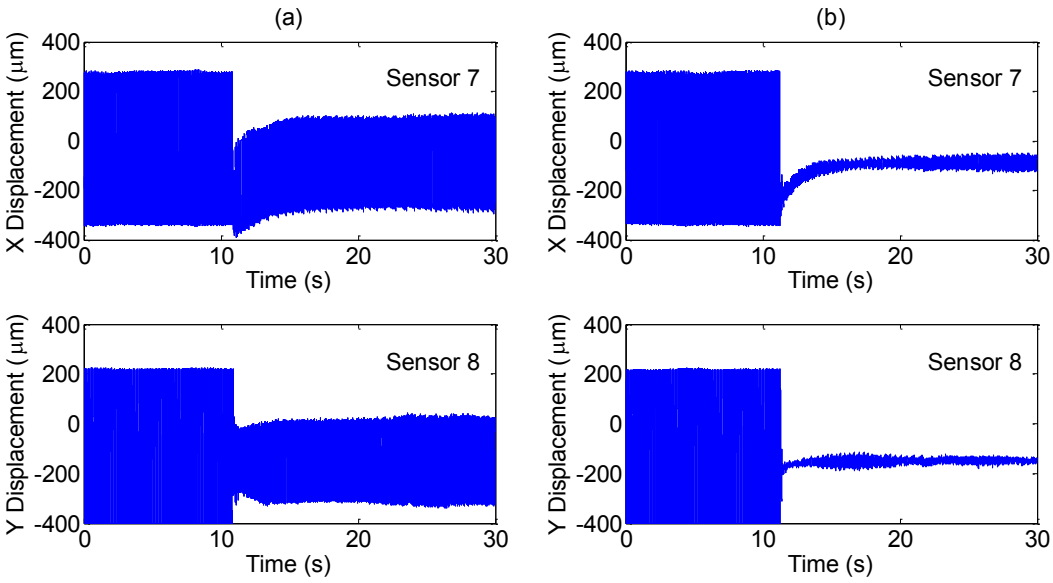

Figure 7.15: Measured displacements at the non-driven end showing the effect of (a) open-loop control based on evaluated force measurement and (b) maximum vibration reduction control, at 19 Hz rotational speed

The corresponding steady-state orbits at all four sensor locations for the same cases at 19 Hz are shown in Figure 7.16. It is evident that rotor/TDB contact occurs only at the non-driven end location before control. The effectiveness of the control is evident.

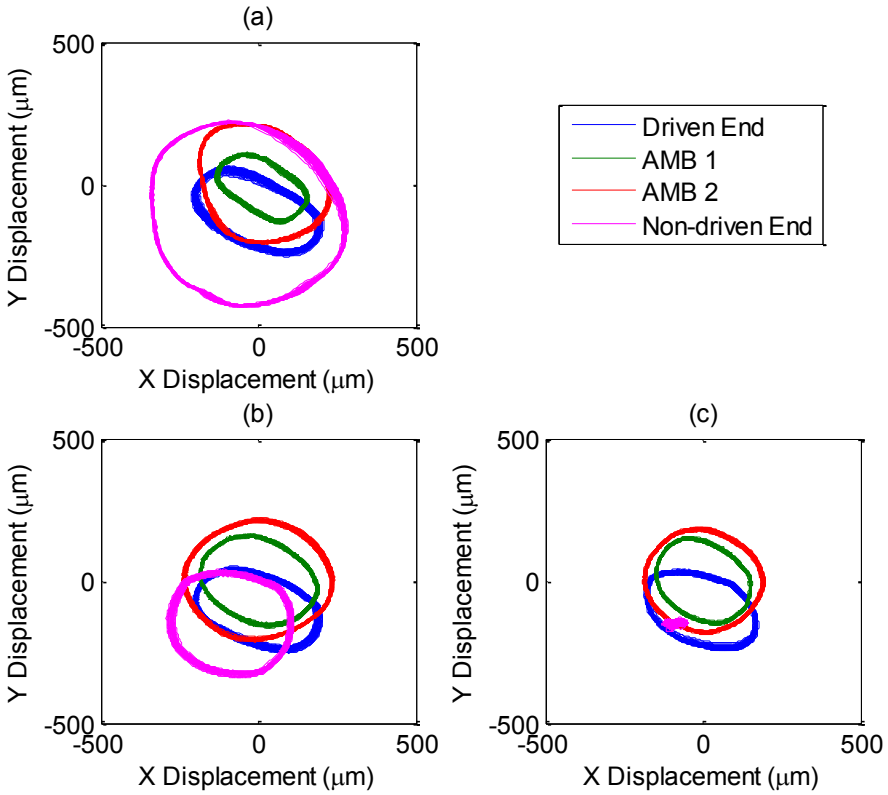

Figure 7.16: Measured orbits at the four sensor plane locations showing the steady-state effect of (a) uncontrolled unbalance with contact (b) open-loop control based on evaluated force measurement and (c) maximum vibration reduction control at 19 Hz

Similar tests were done at frequencies of 17, 19, and 21 Hz, to compare force measurement based control to maximum vibration reduction control. The orbits showing the behaviour before and after control are shown in Figure 7.17. In all cases the rotor is seen to recover from full contact.

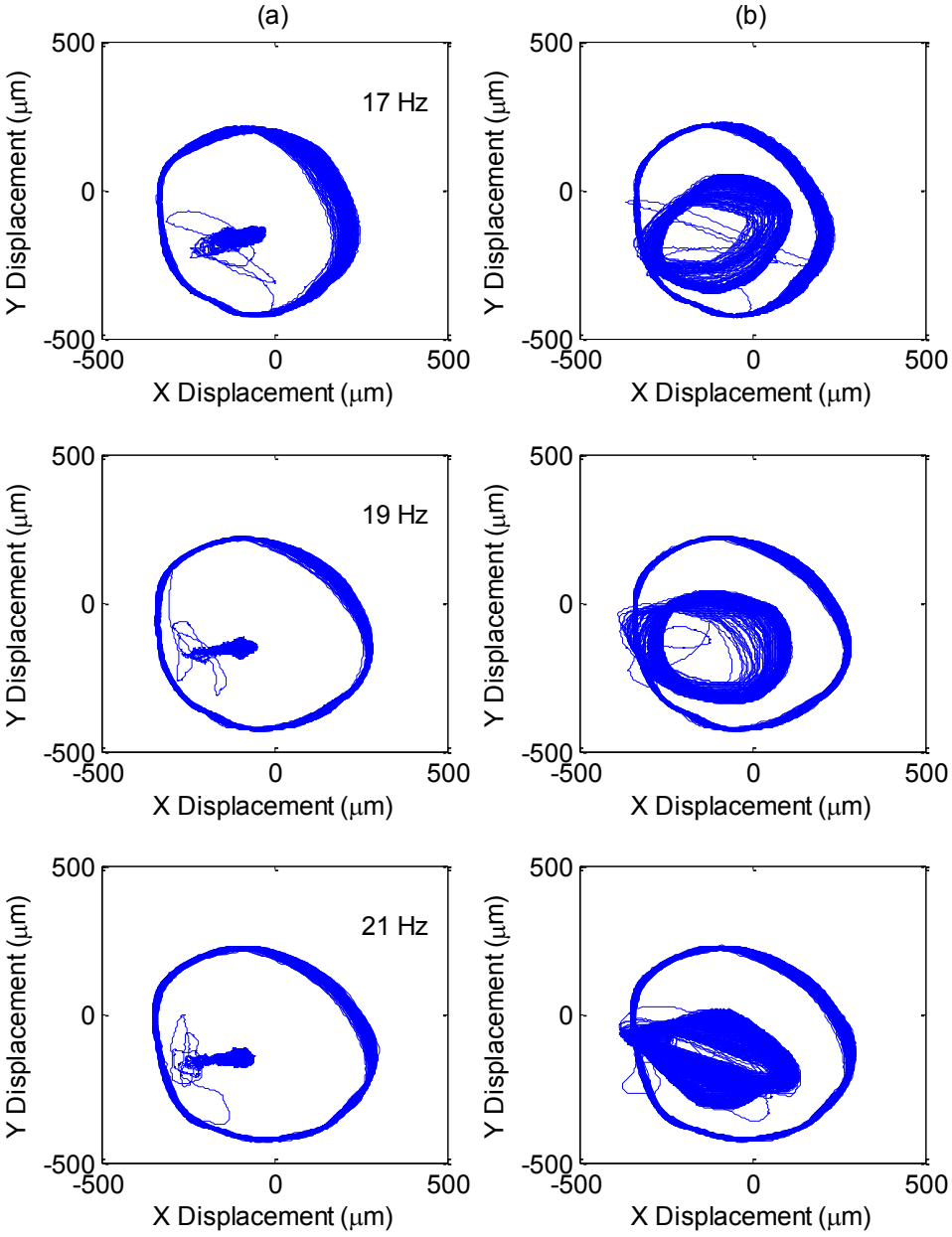

Figure 7.17: Orbits showing the effect of (a) maximum vibration reduction control and (b) evaluated force measurement based control, for frequencies 17, 19 and 21 Hz

Further experimental tests were undertaken to show the required AMB 2 control force amplitude and phase values to recover the rotor from contact with maximum vibration reduction, in comparison to the force amplitude and phase obtained from the evaluated force measurement data. The rotating frequency range of 17-21 Hz was covered in

these tests. Additionally, tests were done to show the force amplitude and phase range within which the unbalanced rotor is fully recoverable from contact using AMB 2 forces for each frequency. Figures 7.18 and 7.19 demonstrate the results. Figure 7.19 shows more points defining the controllable range for the 21 Hz case.

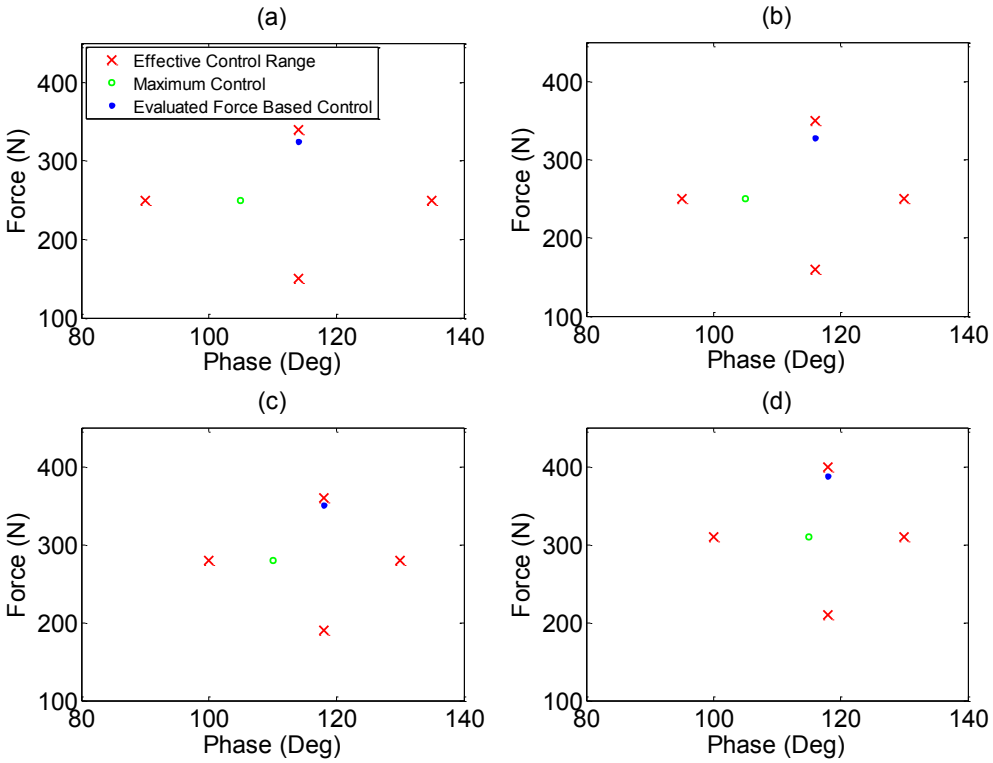

Figure 7.18: Force amplitude and phase values for unbalanced rotor control using AMB 2 forces for rotating frequencies (a) 17 Hz (b) 18 Hz (c) 19 Hz (d) 20 Hz

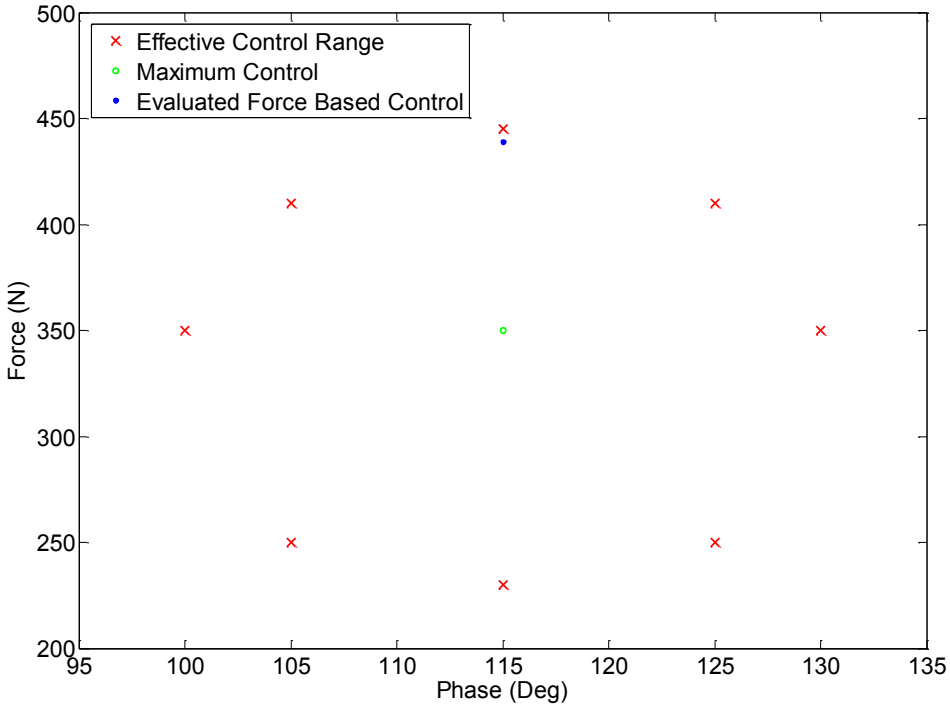

Figure 7.19: Force amplitude and phase values for unbalanced rotor control using AMB 2 forces for a rotating frequency of 21 Hz

A wide range of control force amplitudes and phases that are capable of recovering the rotor from contact are noticed. The point of maximum control refers to control causing maximum vibration reduction as demonstrated experimentally. It is noticed that the evaluated force measurement data give control force amplitude and phase values within the controllable range in all cases, however, the control force amplitude values are consistently higher than those demonstrated with maximum vibration reduction control for the frequency range considered. Figure 7.20 shows the displacement amplitude behaviour of the rotor at the minimum and maximum control force amplitude and phase values shown in Figure 7.19.

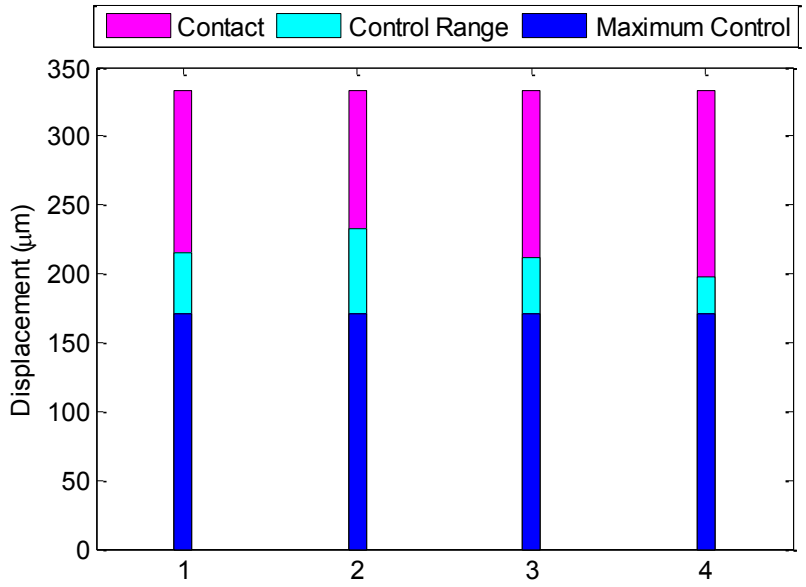

Figure 7.20: Displacement amplitudes with rotor unbalance at 21 Hz rotating frequency showing the maximum contact amplitude, the amplitude with maximum vibration control, and the amplitudes at the maximum and minimum points of the control range: (1) 445 N, 115 Deg; (2) 230 N, 115 Deg; (3) 350 N, 130 Deg; and (4) 350 N, 100 Deg

Contact with full rubbing behaviour occurs at a rotor amplitude of 333 µm at 21 Hz before control is applied. With maximum vibration reduction control, the rotor amplitude reaches 171 µm. The control range defines the range in which the rotor was completely recovered from contact under AMB forces, with a maximum displacement amplitude of 233 µm demonstrated in case (2) of Figure 7.20. Therefore, the recovered rotor displacement amplitude is at least 100 µm less than the 333 µm amplitude at the full contact case. Within this contact range of 100 µm, the contact behaviour develops from occasional bouncing behaviour to full rub at 333 µm.

Thus a displacement reduction of at least a 100 µm is needed for contact-free recovery at 21 Hz. This may be caused by misalignment issues due to the small rotor/TDB clearance used, causing the rotor to enter into bouncing behaviour before reaching full contact. In perfect alignment conditions, the value of 100 µm would be reduced,

increasing the control range and the corresponding force amplitude and phase ranges demonstrated in Figures 7.18 and 7.19, while the control points of force based control and maximum control remain the same.

Figure 7.21 shows a displacement amplitude comparison between the unbalanced rotor contact case, the AMB 2 controlled unbalance based on force measurement data, and the AMB 2 controlled unbalance with maximum vibration reduction. Data for the full frequency range tested are shown at all four sensor locations.

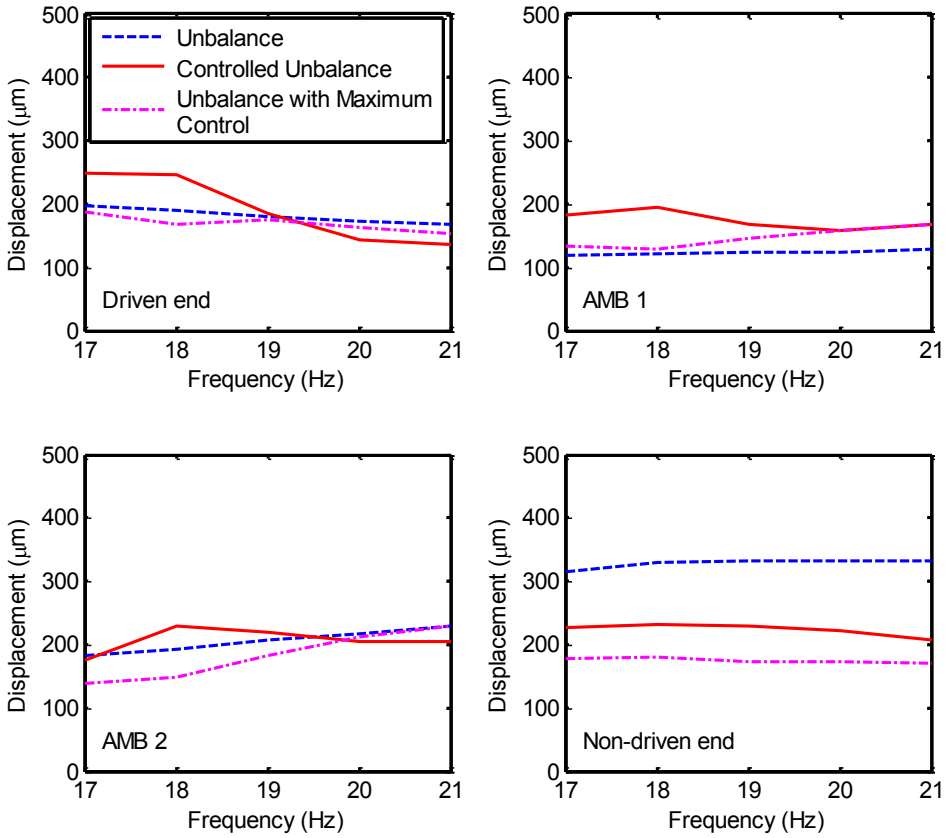

Figure 7.21: Displacement amplitudes at the four sensor plane locations showing controlled and uncontrolled rotor unbalance at the non-driven end for a frequency range of 17-21 Hz

In all cases at all frequencies, single location contact occurs, which is fully controllable by AMB forces. At the non-driven end where contact occurs, the average displacement amplitude for full contact over the frequency range presented is 325 μm. The force measurement based control decreases the amplitude to an average of 220 μm recovering the rotor from contact, while the AMB is capable of decreasing the amplitude to an average of 175 μm in the maximum vibration reduction control case. Therefore, the difference between the evaluated force measurement based control and the maximum achievable vibration reduction control is an average of 45 μm.

Under evaluated force based control, an average reduction in the displacement amplitude of 105 μm is achieved from the contact amplitude level of 325 μm, fully recovering the rotor from contact in all cases.

It can be concluded from these tests that the force measurement data are capable of providing control force amplitude and phase values able to recover the rotor from full contact, when possible.

7.5 Closure

Experimental validation of an open-loop control system based on evaluated force measurement data was performed on the flexible rotor/active magnetic bearing facility. Unbalanced rotor experiments were undertaken at a frequency range covering one of the rotor's critical speeds to test the control strategy. The control suppressed the vibration causing full rotor recovery from rotor/TDB contact using synchronous AMB forces. The range of AMB control data capable of full contact-free recovery was explored for each running speed. The control data consisting of force amplitude and phase values were presented and discussed. This provides insight into new potential control methods capable of achieving rotor/TDB contact recovery utilizing force data estimated from rotor/TDB contact.

Chapter 8

CONCLUSIONS AND FUTURE WORK

8.1 Conclusions

Issues related to rotor/TDB contact conditions in AMB systems are addressed in this thesis. The problem of rotor/TDB contact control during fault conditions or external disturbances experienced by AMB systems was identified as an area that requires significant consideration. Although PID controllers, which are widely used in AMB systems in various applications, offer simple implementation, they are characterised by poor performance in cases where the system experiences input disturbances. This results in the occurrence of rotor/TDB contact in cases where significant inputs to the system occur, such as rotor unbalance or externally induced motion. The importance of devising contact control strategies based on fully operational AMB systems is highlighted. Such strategies would have the advantage of achieving rotor contact-free recovery, even if persistent rotor/TDB contact has developed. Further knowledge of the interaction dynamics between the rotor and the TDBs in AMB systems has been identified as a necessary step in optimising control action that reduces or eliminates the damaging effect of contact.

A rotor/AMB/TDB system, with a 2 m long flexible rotor incorporating 4 disks, was considered in this thesis to study rotor/TDB interaction dynamics theoretically and experimentally. The behaviour of the rotor, which was levitated with two radial active magnetic bearings, was investigated under various contact conditions. A finite element model of the system was presented and employed. The system model incorporated a nonlinear rotor/TDB contact model based on localised Hertzian contact mechanics. Rotor mass changes were introduced to initiate synchronous external unbalance forces

resulting in a range of contact cases. A speed range covering three of the rotor's critical frequencies was employed, and possible types of transient and steady-state contact modes were demonstrated for the AMB system. A map of possible rotor/TDB contact modes at different rotor speeds of up to 32 Hz was produced for the AMB system as a result of running different simulations. The contact modes demonstrated included non-persistent and persistent trapped contact modes of varying contact force levels and time durations. The contact behaviour was shown to be dependent on the unbalance forces, in addition to the rotor speeds. Information about contact caused by unbalance was shown to be obtained from displacement rotating frame coordinates and contact force levels. That provided a background to enable investigation of the restoration of the rotor's position following developed contact cases. It also provided an understanding on the contact dependence on the removal of residual unbalance. It was identified that effective contact force reduction or elimination is important, particularly in persistent contact cases.

In practice, although rotor displacement data are usually sufficient for control and monitoring purposes during normal AMB operation, the experimental assessment of rotor forces is critical to fully evaluating the system characteristics should contact conditions occur. Force assessment gives additional data in relation to the level of accelerations and stresses affecting the TDBs, providing an advantage in identifying and understanding system dynamics pertaining to rotor/TDB interaction. Assessment of contact-induced forces can also identify sufficient control currents needed to maintain AMB operation within its specified limits. In order to undertake experimental investigations of contact-induced forces, design methodology was presented for a rotor/TDB contact force measurement system for the AMB system, which was based on strain gauges. The force measurement system was commissioned and installed on the AMB test rig.

Strain measurements of the TDB support structure of the force measurement system were related to rotor/TDB contact force components. A static calibration method was demonstrated for the system through a series of experimental tests. The calibration established the measurement and estimation of applied AMB control forces, by considering rotor/TDB contact in the AMB system. The dynamic behaviour of the rotor/AMB/TDB system was investigated experimentally through a series of tests

employing the strain measurement system. Various single and multiple contact cases were identified as a result of applying synchronous unbalance AMB forces over a range of whirl frequencies. It was shown that the force measurement system was capable of providing an estimate of dynamic AMB forces, through rotor/TDB contact, as a result of applied AMB forces. Additionally, corresponding phase values were assessed and demonstrated from the measurement system data. The frequency dependent behaviour of the system was demonstrated.

A series of simulations were undertaken corresponding to the experimental dynamic tests employing the force measurement system. Simulation results were compared to measured results, where the relationship between the calculated contact force and the estimated AMB force due to contact measurements was identified and discussed. Experimental and calculated rotor displacement orbits and amplitudes were also demonstrated and compared, showing good agreement. The dynamic force measurement results obtained can significantly facilitate the application of appropriate control methods employing operational AMB forces during contact conditions.

The force and phase data obtained from the force measurement system were validated experimentally using a control strategy based on the evaluated measurements. An open-loop control system was presented, performed, and validated on the flexible rotor/AMB/TDB facility. The open-loop control system employed the application of appropriate synchronous unbalance compensation forces through the magnetic bearings. Rotor/TDB contact was initiated by synchronous rotor unbalance forces through adding unbalance masses to one of the rotor disks. The unbalanced rotor experiments were undertaken at a frequency range covering one of the rotor's critical speeds. The controller was demonstrated to successfully attenuate the vibration, causing full rotor recovery from contact. Rotor recovery from a persistent rub contact mode at a single location was shown during the full operation of AMBs. The range of AMB control data consisting of force and phase values, which is capable of full contact-free recovery of the rotor, was identified experimentally for each running speed considered.

The new force based contact control method presented and demonstrated provides insight into potential control methods capable of achieving rotor/TDB contact

recovery, utilizing data related to contact forces. This will contribute towards improving safety and reliability aspects of existing and potential AMB systems due to rotor/TDB contact reduction or elimination.

8.2 Future Work

A number of different potential areas of future work can be identified. This includes the measurement of direct rotor/TDB contact forces that are independent of AMB forces. Direct contact force measurement would require a different calibration approach, and would provide real force data that would enable better understanding and validation of contact force models.

Dynamic contact tests with rolling element bearings or different bushing materials or lubricants can be undertaken to establish the corresponding effects on force measurements, including friction forces and phase data. Tests can also be performed with different rotor/TDB clearance values.

Single location rotor/TDB contact was demonstrated and controlled in the work of this thesis using force measurement at the contact location. Multiple location contact control is an area of potential research, especially at high frequencies where rotor bending modes can occur. This may require using a number of force measurement devices to fully assess the dynamics of the system.

Control of contact cases at a wider range of running speeds and unbalance levels can be investigated. This can include varying unbalance forces acting on the rotor, where transient and steady-state contact cases occur under different contact modes and for different durations. Other external disturbances causing contact can also be considered, such as base motion, where the applied forces can be varied, and multi-frequency excitations can be considered.

An open-loop control method was proposed in this thesis based on force measurements. Design of closed loop control methods can be investigated. They have the potential for higher performance and reliability in comparison to open-loop strategies.

REFERENCES

Abulrub, A.G., Sahinkaya M.N., Keogh P.S. and Burrows, C.R., 2006a. A constrained Lagrangian approach for modelling multiple contacts of flexible rotors. *IFToMM 7th International Conference on Rotor Dynamics*, Vienna, Austria.

Abulrub A.G., Sahinkaya M.N., Keogh P.S. and Burrows C.R., 2006b. Adaptive Control of Active Magnetic Bearings to Prevent Rotor-Bearing Contact. *ASME International Mechanical Engineering Congress and Exposition (IMECE2006)*, Chicago, Illinois, USA.

Althaus, J., and Ulbrich, H., 1992. A Fast Hydraulic Actuator for Active Vibration Control. *IMechE*, C432/045, pp. 141-148.

Bartha, A. R., 1998. Dry friction induced backward whirl: theory and experiment. *Proceedings of 5th IFToMM Conference on Rotor Dynamics*, Darmstadt, Germany, pp. 756–767.

Bartha, A., 2000. Dry Friction Backward Whirl of Rotors. *Doctoral Dissertation, Swiss Institute of Technology Zurich*.

Bedoor, B. O., 2000. Transient torsional and lateral vibrations of unbalanced rotors with rotor-to-stator rubbing. *Journal of Sound and Vibration*, 229 (3), pp. 627–645.

Black, H. F., 1968. Interaction of a whirling rotor with a vibrating stator across a clearance annulus., *J. Mech. Engng Sci.*, 10 (1), pp. 1–12.

Burrows, C. R. and Sahinkaya, M. N., 1983. Vibration control of multi-mode rotor bearing systems. *Proceedings of the Royal Society of London*, 386, pp. 77–94.

Cade, I.S., Sahinkaya, M.N., Burrows, C.R. and Keogh, P.S., 2008. On the Design of an Active Auxiliary Bearing for Rotor/Magnetic Bearing Systems. *Proc. ISMB 11*, Nara, Japan.

Cade, I., Sahinkaya, M. N., Burrows, C. and Keogh, P., 2009. An active auxiliary bearing control strategy to reduce the onset of asynchronous periodic contact modes in rotor/magnetic bearing systems. *Proceedings of the ASME Turbo Expo 2009*, 6, pp. 855-865.

Cole M.O.T.; Keogh P.S., 2003a. Rotor vibration with auxiliary bearing contact in magnetic bearing systems, Part 2: robust synchronous control for rotor position recovery. *Proceedings of the IMECHE Part C Journal of Mechanical Engineering Science*, 217, 4, pp. 393-409.

Cole, M.O.T. and Keogh, P.S., 2003b. Asynchronous Periodic Contact Modes for Rotor Vibration Within an Annular Clearance. *Proc. IMechE, Part C*, 217, pp. 1101-1115.

Cole, M. O. T., Keogh, P. S., Sahinkaya, M. N. and Burrows, C. R., 2004. Towards fault-tolerant active control of rotor-magnetic bearing systems. *Control Engineering Practice*, 12, pp. 491–501.

Cuesta, E.N., Rastelli, V.R., Medina, L.U., Montbrun, N.I. and Diaz, S.E., 2002. Non-Linear Behaviors in the Motion of a Magnetically Supported Rotor on the Catcher Bearing During Levitation Loss, an Experimental Description. *ASME Turbo Expo*, Amsterdam, Paper GT-2002-30293.

Dell, H., Engel, J., Faber, R. and Glass, D., 1988. Developments and Tests on Retainer Bearings for a Large Active Magnetic Bearing. *Magnetic Bearings, Proc. First Internat. Symp. on Magnetic Bearings*, Zurich, Springer-Verlag.

Dussaux, M., 1990. The industrial applications of active magnetic bearings technology. *Proceedings of the 2nd International Symposium on Magnetic bearings*, pp. 33–38.

Ehrich, F. F., 1965. Bistable vibrations of rotors in a bearing clearance. *ASME paper 65-WA/MD-1*.

Feeny, B. F., 1994. Stability of cylindrical and conical motions of a rigid rotor in retainer bearings. *Proceedings of 4th International Symposium on Magnetic Bearings*, pp. 219–224.

Foiles, W.C. and Allaire, P.E., 1997. Nonlinear Transient Modelling of Active Magnetic Bearing Rotors During Rotor Drop on Auxiliary Bearings. *Proc. MAG'97*, Alexandria, VA, pp. 154-163.

Fumagalli, M., Varadi, P. and Schweitzer, G., 1994. Impact dynamics of high speed rotors in retainer bearings and measurement concepts. *Proceedings of 4th International Symposium on Magnetic Bearings*, ETH, Zurich, Switzerland, pp. 239–244.

Fumagalli, M. and Schweitzer, G., 1996. Measurements on a rotor contacting its housing. *Proceedings of 6th International Conference on Vibrations in Rotating Machinery*, University of Oxford, paper C500/085/96, pp. 779–788.

Fumagalli M., 1997. Modelling and Measurement Analysis of the Contact Interaction between a High Speed Rotor and its Stator. *Doctoral Dissertation, Swiss Institute of Technology Zurich*.

Ginzinger, L. and Ulbrich, H., 2006. Control of a Rubbing Rotor – Experiments and Theory. *Proceedings of the Eleventh Int. Symposium on Transport Phenomena and Dynamics of Rotating Machinery*, Honolulu, Hawaii.

Hawkins, L., Filatov, A., Imani, S. and Prosser, D., 2007. Test Results and Analytical Predictions for Rotor Drop Testing of an Active Magnetic Bearing Expander/Generator. *ASME J. Engineering for Gas Turbines and Power*, 129, pp. 522-529.

Ishii, T. and Kirk, R. G., 1991. Transient response technique applied to active magnetic bearing machinery during rotor drop. *ASME Conference Proceedings*, 35, pp. 191–200.

Ishii, T. and Kirk, R. G., 1996. Transient response technique applied to active magnetic bearing machinery during rotor drop. *Trans. ASME, J. Vibr. Acoust.,* 118, pp. 154–163.

Kasarda, M. E. F., 2000. An overview of active magnetic bearing technology and applications. *The Shock and Vibration Digest*, 32 (2), pp. 91–99.

Keogh, P. S. and Cole, M. O. T, 2003. Rotor vibration with auxiliary bearing contact in magnetic bearing systems, Part 1: Synchronous Dynamics. *Proc. Instn Mech. Engrs, Part C: J. Mechanical Engineering Science*, 217, pp. 377-392.

Keogh P.S., Cole M.O.T., Sahinkaya M.N. and Burrows C.R., 2004. On the control of synchronous vibration in rotor/magnetic bearing systems involving auxiliary bearing contact. *Trans. ASME, Journal of Engineering for Gas Turbines and Power*, 126 (2), pp. 366-372.

Keogh, P. S., 2012. Contact dynamic phenomena in rotating machines: active/passive considerations. *Mechanical Systems and Signal Processing*, 29, pp. 19-33.

Kim, Y. B. and Noah, S. T., 1990. Bifurcation analysis for a modified Jeffcott rotor with bearing clearances. *Nonlinear Dynamics*, 1, pp. 221–241.

Kirk, R. G. and Ishii, T., 1993. Transient response drop analysis of rotors following magnetic bearing power outage. *Proceedings of MAG'93*, pp. 53–61.

Kirk, R. G., Swanson, E. E., Kavarana, F. H. and Wang, X., 1994. Rotor drop test stand for AMB rotating machinery, Part 1: description of test stand and initial results. *Proceedings of 4th International Symposium on Magnetic Bearings*, ETH, Zurich, Switzerland, pp. 207–212.

Kirk, R. G., Raju, K. V., and Ramesh, K., 1996. Evaluation of AMB rotor drop stability. *Virginia Polytechnic Inst. and State Univ, Rotordynamic Instability Problems in High-Performance Turbomachinery*, pp. 197–208.

Kirk, R. G., Raju, K. V. S. and Ramesh, K., 1997. Modelling of AMB turbo-machinery for transient analysis. *Proceedings of MAG'97*, Alexandria, Louisiana.

Kirk, R. G., 1999. Evaluation of AMB turbomachinery auxiliary bearings. *Journal of Vibration and Acoustics, Transactions of ASME*, 121, pp. 156–161.

Kirk, R.G. Gunter, E.J.; Chen, W.J., 2005. Rotor drop transient analysis of AMB machinery. *Proceedings of the ASME International Design Engineering Technical Conferences and Computers and Information in Engineering Conference*, *20th Biennial Conf. on Mechanical Vibration and Noise*, pp. 1003-1012.

Knospe, C. R., Hope, R.W., Fedigan, S. T., and Williams, R. D., 1995. Experiments in the control of unbalance response using magnetic bearings, *Mechatronics*, 5 (4), pp. 385–400.

Kwapisz, D., Stephant J., and Meizel D., 2008. Instrumented bearing for force and moment measurements. *IEEE SENSORS*, Lecce, Italy, pp. 1480–1483, art. no. 4716725.

Lee, J., Allaire, P. E., Tao, G., Decker, J. A., and Zhang, X., 2003. Experimental study of sliding mode control for a benchmark magnetic bearing system and artificial heart pump suspension. *IEEE Transaction on Control Systems Technology*, 11 (1), pp. 128–138.

Li, P., Sahinkaya, M. N. and Keogh, P. S., 2012. Active recovery of contact-free levitation in magnetic bearing systems. *ASME 2012 International Design Engineering Technical Conferences and Computers and Information in Engineering Conference, IDETC/CIE 2012*, Chicago, IL.

Lingener, A., 1990. Experimental Investigation of Reverse Whirl of a Flexible Rotor. *Third Internat. Conf. on Rotordynamics*, Lyon, pp. 13-18.

May, C.P., 2001. Dynamic Simulation of Conventional Bearings Employed As Load-Sharing Auxiliary Support to Active Magnetic Bearings. *University of Bath Thesis*.

Muszynska, A., 1984. Partial lateral rotor to stator rubs. *Proceedings of 3rd International Conference on Vibrations in Rotating Machinery*, University of York, paper C281/84, pp. 327–335.

Muszynska, A., 1989. Rotor to stationary element rub related vibration phenomena in rotating machinery, Literature Survey. *The Shock and Vibration Digest*, pp. 3-11.

Muszynska, A., 2002. Rotor-to-stationary part full annular contact modelling. *Proceedings of 9th International Symposium on Transport Phenomena and Dynamics of Rotating Machinery*, Honolulu, Hawaii.

Nakashima, K., Tsujino, T. and Fujii, T., 1996. Multivariable control of a magnetic levitation system using closed loop identification and H∞ control theory. *Proceedings of the 35th Conference on Decision and Control*, Kobe, Japan.

Nelson H.D. and McVaugh, J.M, 1976. The Dynamics of Rotor-Bearing Systems Using Finite Elements. *ASME Journal of Engineering for Industry*, 98, pp. 593-600.

Nelson, H.D., 1980. A Finite Rotating Shaft Element Using Timoshenko Beam Theory. *ASME Journal of Mechanical Design*, 102, pp. 793-803.

Palazzolo, A.B., Lin, R.R., Alexander, R.M., Kascak, A.F., and Montague, J., 1991. Test and Theory for Piezoelectric Actuator - Active Vibration Control of Rotating Machinery. *Trans. ASME Journal of Vibrations and Acoustics*, 113, pp. 167-175.

Ramesh, K., and Kirk, R. G., 1994. Rotor drop test stand for AMB rotating machinery, Part II: Steady state analysis and comparison to experimental results. *Fourth International Symposium on Magnetic Bearings*, pp. 213–218.

Roark, R.J. and Young, W.C., 1975. Formulas for Stress and Strain. *McGraw-Hill.*

Rutland, N. and Keogh, P. S., 1994a. Design procedure for an active magnetic bearing. *University of Bath*, Technical Report 029/1994.

Rutland, N. and Keogh, P. S., 1994b. Design of an experimental rotor and active magnetic bearing rig. *University of Bath*, Technical Report 030/1994.

Rutland, N. and Keogh, P. S., 1995. Experimental validation of active magnetic bearing force characteristics. *University of Bath*, Technical Report 032/1995.

Sahinkaya M.N., Abulrub A.G., Keogh P.S. and Burrows C.R., 2007. Multiple sliding and rolling contact dynamics for a flexible rotor/magnetic bearing system. *IEEE/ASME Transactions of Mechatronics*, 12 (2), pp. 179-189.

Santos, I. F., 1993. Aktive Kippsegmentlagerung-theorie und experiment. *Fortschritt-Berichte VDI reihe 11*, 189.

Schmied, M., Pradetto, B., 1992. Drop of Rigid Rotor Retainer Bearings. *Third Internat. Symp. on Magnetic Bearings*, Washington, pp. 145-156.

Schoeb, R., and Dasse, K., 2001. Magnetic suspension systems for biomedical applications. *Sixth International Symposium on Magnetic Suspension Technology*, Turin, Italy.

Schoenhoff, U., Luo. J., Li, G., Hilton, E., Nordmann, R. and Allaire, P., 2000. Implementation results of μ–synthesis control for an energy storage flywheel test rig. *Proc. 7th Internat. Sympos. on Magnetic Bearings,* ETH Zurich, pp. 317-322.

Schweitzer, G. and Lange, R., 1976. Characteristics of a magnetic rotor bearing for active vibration control. *IMechE Conference on Vibration in Rotating Machinery*, Cambridge, Paper no. C239/76.

Schweitzer, G., Bleuler, H. and Traxler, A., 1994. Active Magnetic Bearings: Basics, Properties and Applications. *Verlag der Fachvereine*, ISBN 3 7281 21320.

Schweitzer, G., 2002. Active magnetic bearings -chances and limitations. *Proceedings of the Sixth International Conference on Rotor Dynamics*, 1, pp. 1–14.

Schweitzer, G., 2005. Safety and Reliability Aspects for Active Magnetic Bearing Applications - A Survey. *Proceedings of the I MechE Part I Journal of Systems & Control Engineering*, 219 (6), pp. 383-392.

Siemens, 2015. Facts & Figures: Oil-Free Steam Turbine [Online]. *Available from*: http://www.energy.siemens.com/hq/pool/hq/power-generation/steam-turbines/downloads/siemens-oil-free-steam-turbine-fact-sheet-en.pdf

Sinha, A., Meese, K., and Wang, K. W., 1991. Sliding mode control of a rigid rotor via magnetic bearings. *ASME Biennial Conference on Mechanical vibration and noise*, Miami, Florida.

Sivrioglu, S. and Nonami, K., 1995. LMI approach to gain scheduled H∞ control beyond PID control for gyroscopic rotor-magnetic bearing systems. *Proceedings of the 35th conference on decision and control*, pp. 3694–3699.

Swanson, E. E., Kirk, R. G. and Wang, J., 1995. AMB Rotor Drop Initial Transient on Ball and Solid Bearings. *Proceedings of MAG '95: Magnetic Bearings, Magnetic Drives and Dry Gas Seals*, Washington, pp. 207-216.

Ulbrich, H., 1994. Comparison of Different Actuator Concepts for Applications in Rotating Machinery. *International Journal of Rotating Machinery*, 1 (1), pp. 61-71.

Ulbrich, H., Chavez, A. and Dhima, R., 2004. Minimization of Contact Forces in Case of Rotor Rubbing Using an Actively Controlled Auxiliary Bearing. *The 10th International Symposium on Transport Phenomena and Dynamics of Rotating Machinery*, Honolulu, Hawaii.

Von Groll, G. and Ewins, D. J., 2001. The harmonic balance method with arc-length continuation in rotor/contact problems. *J. Sound Vibr*., 241, pp. 223–233.

Wang, X. and Noah, S. T., 1998. Nonlinear dynamics of a magnetically supported rotor on safety auxiliary bearings. *Trans. ASME, J. Vibr. Acoust*., 120, pp. 596–606.

Wang, M., 2016. H_∞ optimal control for linear time invariant and parameter dependent conditions in active magnetic bearing systems. *PhD Thesis, University of Bath.*

Wu, F. and Flowers, G. T., 1993. An experimental study of the influence of disk flexibility and rubbing on rotordynamics. *Proceedings of ASME Conference on Vibrations of Rotating Systems,* 60, pp. 19–26.

Xie, H., Flowers G.T., Feng, L. and Lawrence C., 1999. Steady-State Dynamic Behaviour of a Flexible Rotor with Auxiliary Support from a Clearance Bearing. *Journal of Vibration and Acoustics, Transactions of ASME*, 121, pp. 78-83.

Yang, L. F., Mikulas, M. M., Park, K. C., and Su, R., 1991. Slewing maneuvers and vibration control of space structures by feedforward-feedback moment-gyro controls. *Trans. ASME, J. Dynamic Systems, Measmt, and Control*, 117, pp. 343–355.

Youcef-Toumi, K. and Reddy, S., 1993. Dynamic analysis and control of high speed and high precision active magnetic bearings. *Trans. ASME, J. Dynamic Systems, Measmt, and Control*, 114, pp. 623–632.

ZapomeĬ l, J., Fox, C. H. J. and Malenovsky, E., 2001. Numerical investigation of a rotor system with disc-housing impact. *J. Sound Vibr.,* 243, pp. 215–240.

Zeng, S., 2003. Modelling and experimental study of the transient response of an active magnetic bearing rotor during rotor drop on back-up bearings. *Proceedings of the IMechE Part I Journal of Systems & Control Engineering*, 217 (6), pp. 505-517.

Zhou, K. and Doyle, J.C., 1997. Essentials of robust control. *Prentice Hall*, 411p.